Departament de Física
Facultat de Ciències
Universitat Autònoma de Barcelona

DEFORMATION BEHAVIOUR AND STRENGTHENING OF BULK METALLIC GLASSES AND NANOCOMPOSITES

Thesis presented by
Amadeu Concustell i Fargas
Bellaterra, January 2007

Els Doctors **Maria Dolors Baró i Mariné** i **Jordi Sort i Viñas**, directors de la tesi doctoral realitzada per **Amadeu Concustell i Fargas**, i que porta per títol "Deformation Behaviour and Strenghtening of Bulk Metallic Glasses and Nanocomposites"

FAN CONSTAR: Que l'aportació del doctorand al treball que es presenta ha estat fonamental tant pel que fa al disseny experimental com a l'obtenció de les mostres, la realització dels experiments, l'anàlisi de les dades i la discussió i elaboració dels resultats presentats.

I perquè així consti, a petició de l'interessat i als efectes oportuns, ho signem a Bellaterra, el 25 de gener de 2007.

Dra. M. D. Baró Dr. J. Sort

AGRAÏMENTS:

En primer lloc vull fer constar que aquesta tesis doctoral no s'hagués dut a terme sense la col·laboració de moltes persones. A totes elles vull expressar la meva sincera gratitud.

Als meus directors de tesis, la Prof. Maria Dolors Baró i el Dr. Jordi Sort, vull agrair-los la confiança dipositada en mi. També els he d'agrair el seu estímul en la meva tasca investigadora, els mitjans que han posat a la meva disposició, els ànims i l'ajut per tal de poder fer estades en altres centres de recerca a l'estranger, i la dedicació amb què han dirigit i coordinat aquesta tesis doctoral.

Igualment vull agrair al Prof. Santi Suriñach l'especial dedicació amb la qual m'ha atès. També li he d'agrair la seva inestimable ajuda i els valuosos consells que m'ha donat.

Aquests anys al grup he tingut l'oportunitat de conèixer molta gent i compartir amb ells molts bons moments. Vull doncs donar les gràcies a aquests companys per l'estímul que han suposat i els coneixements que hem compartit: Pau Solsona, Enric Menéndez, Nele Van Steenberge, Germán Salazar, Josep Nogués, Veronique Langlais, i també als companys que ens han deixat: Ádam Révész, Azat Gimazov, Daciana Ile, Martí Gich, Alex Zhilyaev, Stefania Doppiu, Margaret Zielinska, Sebastian Brück, Vladimir Gavrilov i Tony Spassov.

Bona part d'aquesta tesis no s'hagués pogut dur a terme sense les estades que he realitzat a l'estranger. Primer de tot, al Prof. Jürgen Eckert li agraeixo especialment la seva invitació per poder treballar a l'IFW-Dresden durant gairebé un any. Els mitjans que va posar a la meva disposició i les discussions mantingudes em van ajudar enormement.

Durant les estades a l'IFW-Dresden he conegut a molta gent que m'ha ajudat en la preparació de mostres, i en la utilització de diferents tècniques experimentals. M'agradaria però, fer especial èmfasis en el Dr. Germán Alcalá i la Dra. Sònia Mato per la seva amistat i ajuda en tot moment. Igualment el Dr. Norbert Mattern per la seva ajuda en les experiències de sincrotró.

Al Prof. Lindsay Greer li dono les gràcies per la seva invitació al seu departament a la Universitat de Cambridge. També agrair-li els coneixements adquirits en les múltiples discussions que varem mantenir.

A tots els tècnics, Jordi López, Manel Garcia i Rafael Moraira, els he d'agrair la rapidesa i eficàcia amb què han resolt qualsevol tipus de problema tècnic que ha aparegut.

També vull agrair al Ministeri de Ciència i Educació Espanyol per haver-me concedit una beca FPI (FP-2001-0517) sense la qual hagués estat molt més difícil la realització d'aquesta tesis.

Als meus amics els agraeixo els bons moments que hem passat junts durant la realització d'aquesta tesis, i els ànims que m'han donat en tot moment.

Finalment, vull donar les gràcies a la meva família i especialment a la Cristina Cano per l'estima i l'ajuda que m'han donat.

Index

Preface

Metallic glasses have been the subject of widespread research over the past four decades with significant advancement in their understanding. As the name suggests, they are metallic alloys with no long-range order. The lack of long-range atomic order makes their properties and behaviour considerably different from those of crystalline alloys. For example, they typically behave as very soft magnetic materials (low coercitivity and high permeability) and have led to commercial applications such as transformer cores, magnetic read-heads and magnetic shielding [1]. By some specific treatments or techniques, it is possible to control the total or partial crystallization of metallic glasses. In some cases very fine, uniform microstructures have been exploited for their hard magnetism [2]. Furthermore, early work already pointed out that their mechanical behaviour showed unique properties, i.e. high strength, large elastic limit, homogeneous and inhomogeneous modes of deformation, and the novel "molten" appearance of fracture surfaces [3,4].

Due to their poor glass-forming ability, the early glass systems were typically cast by rapid quenching techniques, with critical cooling rates of 10^5 to 10^6 K s^{-1}, resulting in limited section thickness. The development of bulk metallic glasses (BMG) started with Pd-based compositions [5], and after extensive work, an enlarged range of multicomponent alloys exists with significant lower critical cooling rates [6,7].

The combination of their high yield strength together with the possibility of casting metallic glasses in bulk form has triggered the interest in using them as structural materials [8]. However, metallic glasses show a distinctive localization of the plastic deformation into shear bands when loaded under ambient conditions [9,10]. Instead of work-hardening, metallic glasses soften due to the shear band formation which prevents stable plastic elongation in tension. Therefore, enhancement of the ductility of this type of materials has been the aim of much research work.

Recent works have studied the instrinsic toughening of metallic glasses [11,12]. The significance of the ratio of the elastic shear modulus, μ, to the bulk modulus, B, for the magnitude of toughness has been examined for a variety of different metallic glassy alloys. This approach to the brittle/plastic behaviour was first used in crystalline alloys [13,14]. The competition between flow and fracture relates the resistance to plastic deformation, proportional to μ, to the resistance to dilatation that occurs in the region of a crack tip, which is proportional to B. The results of these works on metallic glasses indicate that exceeding a critical value of μ/B (i.e. in the range of 0.41-0.43) produces an amorphous/annealed glass that approaches the ideal brittle behaviour associated with oxide glasses. Therefore, the correlation between fracture energy and elastic moduli indicates that the intrinsic toughness in metallic glasses may be enhanced by selection of elements with low μ/B (or, equivalently, high Poisson ratio, ν) as constituents.

The tremendous toughness increase that accompanies multiple shear banding indicates that proliferation of shear bands, regardless of how it is accomplished, should provide a powerful toughening mechanism in amorphous metals [15]. This clearly provides the opportunity for microstructural design of extrinsically toughened BMGs via a variety of techniques. The presence of a secondary phase (amorphous or crystalline) has been shown to promote multiple shear band nucleation sites via mismatch in various mechanical properties, while also providing barriers to shear band propagation. The result of the promotion of shear bands and hindering their propagation finally results in macroscopic compressive ductility [16,17].

Therefore, the research on the fundamentals of plastic deformation of metallic glasses and the effects of secondary phases on the ductility of new glass forming systems open a broad range of new investigations.

The main objectives of this thesis are:

- To shed light on the shear band formation and propagation in metallic glasses, and its dependence with the strain rate by means of nanoindentation.

- To study the effects of intrinsic anelasticity of the metallic glasses on nanoindentation tests.

- To investigate the crystallization behaviour, the thermal stability and the mechanical properties of $Cu_{60}Zr_xTi_{40-x}$ amorphous alloys (x = 15, 20, 22, 25, 30) prepared by melt-spinning and copper mould casting.

- To correlate the mechanical properties with the microstructure on the degree of devitrification of a $Cu_{60}Zr_{22}Ti_{18}$ alloy.

- To investigate the mechanical properties, by means of nanoindentation, of a two-phase amorphous Ni-Nb-Y alloy.

- To study the differences in the microstructure, mechanical properties and deformation behaviour of a Ti-based multicomponent alloy composed of micrometer-sized dendrites embedded in a nanostructured eutectic matrix before and after subjecting it to high pressure torsion (HPT).

This thesis has been organized in different chapters as follows:

- Chapter 1 introduces some general aspects on the theory of metallic glasses and nanocrystalline alloys. A brief discussion on the basics of the mechanical properties of amorphous materials and nanocrystalline alloys is also presented since the main part of the results are on these properties.

- Chapter 2 deals with the experimental techniques used for casting the studied alloys and to characterize their thermal, structural and mechanical properties. Furthermore, the experimental procedure for each technique is explained.

- Chapter 3 presents the results obtained and the discussion.

- Chapter 4 includes the main conclusions of the work, and the possible future research to be developed.

Finally, I would like to note that this thesis has been carried out in the framework of two Spanish research projects (MAT-2001-2555 and MAT-2004-01679) and two European research projects (HPRN-CT-2000-00033 and MRTN-CT-2003-504692).

References

[1] Masumoto T, Egami T: Mater Sci Eng 1981; 48:147.

[2] Croat JJ, Herbst JF, Lee RW, Pinkerton FE: J Appl Phys1984; 55:2078.

[3] Pampillo CA, Polk DE: Acta Metall 1974; 22:741.

[4] Masumoto T, Maddin R: Mater Sci Eng 1975; 19:1.

[5] Kui HW, Greer AL, Turnbull D: Appl Phys Lett 1984; 45:615.

[6] Peker A, Johnson WL: Appl Phys Lett 1993; 63:2342.

[7] Inoue A: Acta Mater 2000; 48:279.

[8] Hufnagel TC: On Mechanical Behavior of Metallic Glasses, Scripta Mater 2006; viewpoint nº37.

[9] Spaepen F: Acta Metall 1977; 25:407.

[10] Argon AS: Acta Metall 1979; 27:47.

[11] Lewandowski JJ, Greer AL, Wang WH: Philos Mag Lett 2005; 85:77.

[12] Xi XK, Zhao DQ, Pan MX, Wang WH, Wu Y, Lewandowski JJ: Phys Rev Lett 2005; 94:1255510.

[13] Hecker SS, Rohr DL, Stein DF: Metall Trans A 1978; 9A:481.

[14] Cottrel AH: Advances in physical metallurgy, (Institute of Metals, London, 1990, Edited by: Charles JA, Smith GC).

[15] Schroers J, Johnson WL: Phys Rev Lett 2004; 93:255506.

[16] Hays CC, Kim CP, Johnson WL: Phys Rev Lett 2000; 84:2901.

[17] Ott RT, Sansoz F, Molinari JF, Almer J, Ramesh KT, Hufnagel TC: Acta Mater 2005; 53:1883.

1. Introduction to Metallic Glasses and Nanocrystalline Materials

This chapter deals with certain general aspects of metallic glasses and nanocrystalline materials. Initially the classical theory of nucleation and growth of crystals in an undercooled liquid is described since glass formation may be understood as the absence of crystallinity in a material. The phenomenology of the liquid to glass transition, an introduction to the free volume model and the crystallization of metallic glasses are included. It is also noted that the structure of metallic glasses differs from the crystalline alloys, giving them unique properties. The main mechanical properties of metallic glasses together with their mechanisms of elastic and plastic deformation are also described. Metallic-glass-matrix composites which represent innovative systems to further improve the mechanical properties of metallic glasses are also presented. The last part of the chapter deals with nanocrystalline materials and their mechanical properties. The reduction to the nanometer scale of the grain size results in outstanding properties, but the mechanisms of plastic deformation strongly depend on the grain size of the material, as it is shown below.

1.1. Metallic Glasses

Amorphous metallic alloys or metallic glasses are metals and metal alloys with no long range atomic order. That is, translation characteristic order of the crystalline alloys or orientational characteristic order of quasicrystals is not shown at a longer scale of the constituent elements. Furthermore, metallic glasses exhibit glass transition, i.e. they show an abrupt change in the second order thermodynamic properties (i.e. heat capacity or thermal expansion) at a given temperature from values similar to a crystal until values similar to a liquid.

1.1.1 Nucleation and Growth of Crystals

It is now appropriate to ask why a liquid metal can be extensively undercooled for extended observable times without crystallization. The explanation for this observation lies in the resistance of the undercooled liquids to the formation of crystalline nuclei of critical size [1]. The classical theory of nucleation and growth of crystals is described below and gives us an initial clue. From this theory, it is shown that the time scale for nucleation of crystals depends strongly on undercooling of the liquid allowing glass formation.

1.1.1.1 Nucleation of crystals

The essential driving force for a phase transformation is the difference in the free energies of the initial and final configurations of the assembly, but when small particles of the new phase are formed, the free energy rises at first. The increase is due to the considerable proportion of atoms in these particles which are situated in transition regions between the phases, where they do not have the environment characteristic of the new phase in bulk. Hence, the free energy change (Δg) on the nucleation of a spherical crystal of radius r in the liquid may be described by

$$\Delta g = -(4\pi/3)r^3\Delta g_v + 4\pi r^2\gamma_{SL} \qquad \text{eq. 1.1}$$

where Δg_v is the difference in free energy between unit volumes of the crystal and the liquid and γ_{SL} is the interfacial energy between the crystal and the liquid. The curve of Δg against r will increase to a maximum and decrease again. The position of the maximum is given by $\partial\Delta g/\partial r=0$, which leads to the critical radius of the droplet r_c as

$$r_c = 2\,\gamma_{SL} / \Delta g_v \qquad \text{eq. 1.2}$$

A nucleus of radius r_c is in unstable equilibrium with the liquid. Droplets of radius $r < r_c$ will tend to disappear, while droplets of radius $r > r_c$ will tend to grow.

In the above reasoning, the formation of a nucleus has been regarded as a homogeneous process occurring with equal probability in all parts of the assembly. In practice, this is unlikely to happen unless the assembly is extremely pure. More usually, the presence of impurity particles enables nuclei to be formed with a much smaller free energy of activation than that of the homogeneous nuclei. For a nucleus in the form of a spherical cap growing on a flat substrate, the barrier to heterogeneous nucleation (W_h*) is given by

$$W_h^* = W^* f(\theta) \text{ and } f(\theta) = (2 + \cos\theta)(1-\cos\theta)^2/4 \qquad \text{eqs. 1.3 and 1.4}$$

where θ is the contact angle between the crystal and the nucleating heterogeneity and W* is the free energy of a heterogeneous nuclei of radius r_c. The function, $f(\theta)$, substantially reduces the barrier to nucleation when the contact angle is small.

At temperatures below the liquidus temperature, embryos (nucleis of $r < r_c$) are formed due to fluctuations in the melt. The growth of an individual embryo may be assumed to involve a large number of small fluctuations, and only rarely will there be a sufficiently long chain of forward fluctuations for an embryo to reach the critical size. Following Christian [2], the rate of formation of critical nuclei (I_v) is given by

$$I_v = \frac{n_v kT}{3\pi\lambda^3\eta}\exp\left(-\frac{W^*}{kT}\right) \qquad \text{eq. 1.5}$$

where n_v is the number of molecules or formula units of nucleating phase per unit volume, λ is a jump distance, of the order of atomic dimensions and η is the viscosity of the liquid.

1.1.1.2 Crystals Growth

The formation of stable nucleus is followed by their subsequent growth. Two main types of thermally activated growth are recognized: interface controlled and diffusion controlled.

Interface growth is controlled by processes in the immediate vicinity of the boundary. This means that there is a continuous growth at all points of the boundary or the interface is stepped on an atomic scale, and atoms are transferred from one phase to the other only at these steps. When crystals grow by interface control, the growth rate (u) can be written [2]

$$u = \left(\frac{fD_c}{\lambda}\right)\left[1 - \exp\left(-\frac{\Delta g_v}{kT}\right)\right] \qquad \text{eq. 1.6}$$

where D_c is the kinetic coefficient governing the rate of transport at the crystal/liquid interface, f is the interface site factor (i.e. the fraction of sites on the interface to which an atom can attach), and the quantity in brackets is the thermodynamic factor determining the probability that an atom on the crystal surface will remain there, rather than jumping back into the liquid.

Diffusion controls the growth when the nucleus are richer in solute atoms than the liquid, then there may be a region depleted in solute formed around the crystals as growth proceeds. The continual growth of the particles requires chemical diffusion, and as the particle increases in size, the effective distances over which diffusion takes place may also increase. When the particle is first formed, it is probable that processes near the interface will control the net rate of growth, but the volume diffusion will eventually become the dominant factor. The particle will then grow just as fast as the diffusion rate allows. In contrast to the linear growth law obtained when interface processes dominates the growth of a crystalline particle, the position of the interface and the growth rate may be proportional to the square root of the time when diffusion is decisive [2].

1.1.2 Glass Forming Systems

The absence of any nucleation during the cooling from the melt until the glass transition temperature ensures forming a glass material without any crystalline precipitate. Therefore, the following equation must be satisfied [3]

$$V\int_0^t I_v dt < 1, \qquad \text{eq. 1.7}$$

where V is the volume of the sample. This is a rigorous definition, as it ensures that a material that is called a glass is truly free of any crystallinity. However, calculations from Vreeswijk et al. [4] predicted that SiO_2 would have to be cooled 10^{10} times faster than GeO_2 to form a glass, and that As_2O_3 would have to be quenched at 10^7 K/s. These results are clearly inconsistent with

experimental evidence. The reason for the failure of this approach is indicated in Fig. 1.1. For many systems, the temperature ranges where the nucleation and growth rates are significant do not overlap. It may be virtually impossible to avoid forming a nucleus, but those nuclei that do form may not be able to grow to any meaningful size.

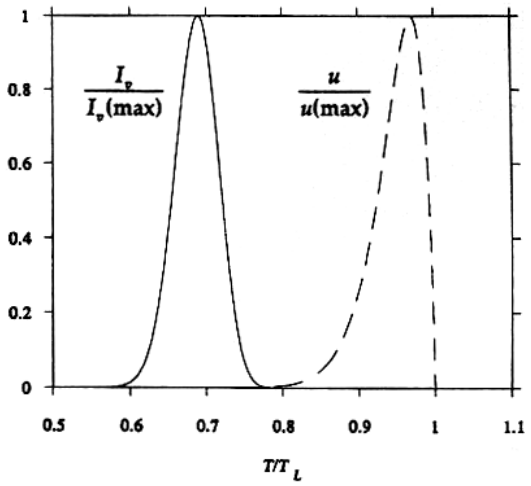

Figure 1.1. Rates of nucleation and crystal growth in SiO_2, calculated from standard theory [5].

The glass forming ability (GFA) of different metallic systems have been explained by a variety of schemes. Although they seem to work for certain groups of materials, they fail for others. At the time being, there is not a satisfactory theory which may predict the GFA of a metallic alloy [5]. However, Egami and Waseda [6] could predict the composition limit for glass formation for a binary system using atomistic theory of hard-sphere dense-random-packing (HS-DRP) and some semiempirical rules have been formulated by Inoue [7] in order to relate the GFA of a system with some fundamental magnitudes.

1.1.3 The Glass Transition

A liquid can be cooled below the liquidus temperature, T_l, if the rates of nucleation and growth of crystals are small enough. At temperatures lower than T_l, the liquid is in metastable equilibrium. If there are small changes in state caused, for example, by sudden heating or cooling, the properties of the liquid gradually approach their equilibrium values. The time-dependent variation in physical properties as the liquid approaches equilibrium is called structural relaxation or physical aging. The glass transition is a region of temperature in which the rate of relaxation (corresponding to a viscosity of $\eta \approx 10^{11}$-10^{13} Pa·s) becomes comparable to the time scale of the measurement.

The temperature dependence of properties such as specific volume (V) and enthalpy (H) suffer a change at the glass transition. As illustrated in Fig. 1.2, the volumetric thermal expansion coefficient ($\alpha_v = \mathrm{d} \ln V/\mathrm{d}T$) decreases near the glass transition temperature (T_g) from a high value characteristic of the equilibrium liquid to a smaller value characteristic of solid glass.

The stronger temperature dependence of the liquid may be explained because the atoms are free to diffuse, so changes in temperature can produce different atomic configurations in addition to changes in vibrational amplitude. In the glass, the atoms are frozen into fixed position and the properties change only because the temperature affects the amplitude of vibration of the atoms around those positions.

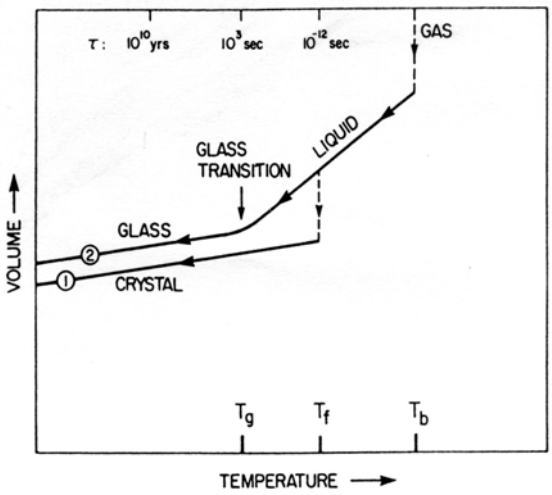

Figure 1.2. Volume change during cooling of a liquid to a crystalline solid (1) or glass (2), [8].

1.1.3.1 Cooling rate dependence of the glass transition temperature (T_g)

The dependence of the glass transition temperature on the cooling rate, $\beta = dT/dt$ shows the kinetic nature of the glass transition. It is observed that the higher is β, the higher is T_g [5]. This is easy to understand if the process of cooling is regarded as a sequence of temperature jumps of size ΔT followed by isothermal holds of length $\Delta t = \Delta T/\beta$. The liquid remains in equilibrium as long as Δt is much longer than the relaxation time, which is proportional to the viscosity [9]

$$\tau = \eta / \zeta \qquad \text{eq. 1.8}$$

where ζ is a constant material dependent and τ is the relaxation time or the rate of relaxation. At high temperatures, τ is much higher than Δt, but near T_g, $\tau \approx \Delta t$, so relaxation of one temperature step is not complete before the next step is taken, and the structure drifts farther and farther out of the equilibrium as cooling continues. The greater the cooling rate, the less time is available for relaxation of each step; since Δt is smaller, the transition occurs at a higher temperature.

1.1.3.2 Thermodynamic and kinetic aspects

A phase transition is said to be first order if the volume and entropy (which are first-order derivatives, with respect to pressure or temperature, of the thermodynamic Gibbs

function) change discontinuously at a certain temperature and pressure. In the glass transition, the discontinuous magnitudes are the specific heat, $c_p = T(\partial S/\partial T)_p$, and α_v, which are second-order derivatives of the thermodynamic Gibbs function. Therefore, the liquid to glass transition is thought to be a second order thermodynamic transition.

However, these changes are not sharp but instead are diffuse, occurring over a small temperature interval rather than at a single sharply definable temperature. These observations are a manifestation of the kinetic aspects of the glass transition. Furthermore, the influence of β on the observed transition, shown in section 1.1.3.1, is the clearest proof that the event actually observed near T_g differs from a strict second-order transition and manifests the kinetic dimension of the glass transition.

Although kinetic effects are important in all practical observations of the transition between the amorphous solid and the liquid phase, both the Gibbs-DiMarzio and the Turnbull-Cohen theories [8] reflect the following prevalent view of the glass transition: there exists an underlying thermodynamic transition that is intimately related to T_g. While kinetics intervenes to influence the placement of T_g in a particular set of experimental circumstances, T_g never strays very far from the value corresponding to the underlying transition.

In fact, there is a strong empirical support for the idea that the observed glass transition is the kinetically modified reflection of an underlying equilibrium transition. The specific heat of the liquid is substantially larger than that of the crystal, and at a given temperature

$$c_{p_{liq}} > c_{p_{cryst}} \rightarrow \left(\frac{\partial S}{\partial T}\right)_{liq} > \left(\frac{\partial S}{\partial T}\right)_{cryst} \qquad \text{eq. 1.9}$$

moreover, the excess entropy, $S_{ex}(T) = S_{liq}(T) - S_{cryst}(T)$, drops sharply between the melting temperature and the glass transition temperature. Therefore, at a given temperature below T_g, known as the Kauzmann temperature T_k, it may happen that $S_{ex} < 0$. Since the existence, at the same temperature, of a liquid phase with lower entropy than the stable crystalline phase is physically implausible, the existence of a transition (the glass transition) is physically necessary in order to keep $S_{ex} > 0$. Indeed, the specific heat of both crystalline and amorphous solids is nearly equal, it follows immediately that S_{ex} levels off at low temperatures to a nearly constant value close to S_{ex} (T_g).

1.1.4 Atomic Structure of Metallic Glasses

Crystalline and amorphous solids share essential properties of the solid state. However, their atomic-scale structures have fundamental differences, which give them their different properties.

In crystalline solids, the nearest-neighbour separations and bond lengths are exactly equal (with permission of thermal fluctuations) and a periodic and translational net may be

defined with the stable atomic positions. Therefore, long-range order is a main property of the crystalline structure. Figure 1.3 a) shows a clear example of a crystalline structure.

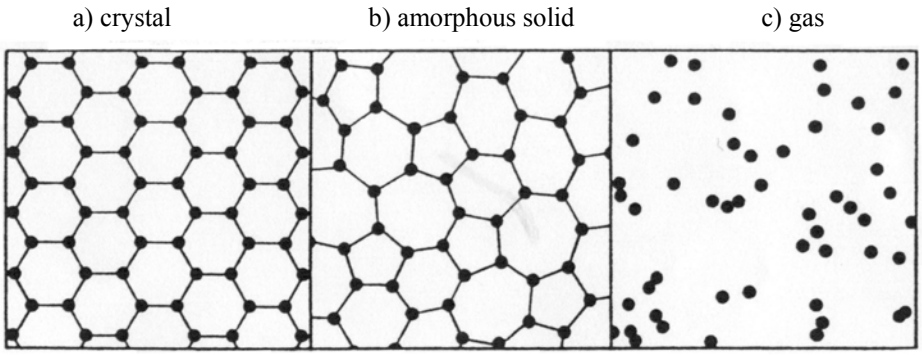

Figure 1.3. Bidimensional structure for different matter states. Solid dots denote the equilibrium positions about which the atoms oscillate a) and b); for the gas c), the dots denote a snapshot of one configuration of instantaneous atomic positions [8].

However, the essential structural difference between crystal and glass consists merely in the latter's loss of long-range order. Thus, while the lack of long-range order in glasses implies randomness at large separations, the atomic-scale structure is highly non-random for a few interatomic distances about any given atom, as shown in Fig. 1.3 b). In order to compare a genuine random array like a gas, Fig. 1.3 c) has been drawn. Therefore, it is recognised that short-range order (SRO) is very much in evidence in the structure of amorphous solids.

Unlike the crystalline structure, the atomic structure of amorphous alloys (i.e. SRO) is highly degenerate and non-unique. As a consequence it has many internal degrees of freedom which can be easily changed by heat treatment or mechanical deformation. The SRO in amorphous materials can be considered as a consequence of the existent chemical short range order (CSRO) and the geometrical short range order (GSRO) in the amorphous structure [10].

All metallic glasses stable at room temperature are alloys. In most cases, a completely random mixture is not attained, so that the chemical composition around the atoms of each alloying component is different from the average. The system then has a CSRO. It is interesting to note that a type of atom in an amorphous structure presents a different number and type of neighbours in the first neighbour-shell than what it does in the crystalline state. Some important changes in the properties due to heat treatment or mechanical deformation are due to changes in CSRO, i.e. changes in the Curie temperature and induced magnetic anisotropy. Such changes in the CSRO do not have to involve diffusional exchange of atoms, but will take place also via more collective atomic rearrangements.

While many properties depend upon CSRO, they also depend upon the details of the geometry of the structure itself, or the degree of randomness of the structure. In network glasses, such as amorphous silicon or germanium, oxides and polymers, the topology of the structure is well defined in terms of connectivity of bonded atoms, and many physical and chemical

properties are determined largely by GSRO. In metallic glasses, the metallic nature of the atomic bonding makes the definition of atomic connectivity almost undefined [10]. However, since the first nearest neighbour is reasonably well defined owing to the presence of a deep valley in the radial distribution function between the first and the second peaks, it is still possible to define topology of the system in terms of the topology of Voronoi polyhedra which is equivalent to Wigner-Sietz cells in crystals [10].

In fact, the atomic structure of metallic glasses is still under discussion [11,12]. Metallic glasses also exhibit order over 1-1.5 nm (for comparison, a typical metallic atom has a diameter of around 0.3 nm). Clusters of atoms (giving their SRO) gather to generate this medium-range order forming a distorted dense packing structure (e.g., face-centred-cubic) [11]. Therefore, the atomic structure of metallic glasses is characterized not only by SRO, also by a medium range order.

1.1.5 Free-volume Model

The free-volume model is noted for its physical plausibility, mathematical simplicity, and its value for qualitatively predicting various experimental observations connected with the liquid to glass transition, diffusion in glasses and its mechanical properties. The concept of free volume is intuitively appealing and extremely useful. It has been known that volume is a good measure of the viscosity of a liquid [13] and the success by Cohen and Turnbull [14-16] to quantify the change of viscosity of a liquid with the temperature made this theory widely applicable.

In the gaseous state atoms are free to move, but a liquid is a condensed matter. An atom is trapped in the cage of neighbouring atoms, but there are small space in-between the atoms. According to the free volume model [14-16], the probability for an atom to have a free volume between v and $v+dv$ is given by

$$p(v)dv = \frac{v_f}{\gamma}\exp\left(-\frac{\gamma v}{v_f}\right) \qquad \text{eq. 1.10}$$

where γ is a constant of the order of unity that takes into account overlap of free volume between neighbouring atoms, and v_f is the average free-volume per atom. The probability, c_f, that a free volume fluctuation greater than v^*, the minimum size that makes a diffusional jump possible, is formed is then:

$$c_f = \int_{v^*}^{\infty} p(v)dv = \exp\left(-\frac{\gamma v^*}{v_f}\right) \qquad \text{eq. 1.11}$$

Now, since an atom is confined in the cage, a moving atom gets "backscattered" by the neighbouring atoms, unless there is a big enough space, v^*, next to it so that the atom can move

into this space. The magnitude of v^* is about 80% of the atomic volume. Thus the diffusivity is given by [17]

$$D = ak\lambda^2 c_f \qquad \text{eq. 1.12}$$

where a is a geometric factor, k the atomic jump frequency and λ the average jump distance. This gives rise to the Vogel-Fulcher law for viscosity in liquids. When a liquid is rapidly cooled the system freezes above T_g, and the value of v_f remains high. If the rapidly cooled glass is annealed below T_g, structural relaxation takes place and v_f decreases and various other related properties consequently change.

However, the free-volume model has some imperfections. For example, it is assumed that the atomic transport in liquids and glasses occurs through atom jumps into a free space next to it, similar to vacancy atomic diffusion in crystals. But it has long been known that large vacancies are highly unstable in a glass [18]. Recent molecular dynamics (MD) simulations of diffusion in glasses clearly show that diffusion in liquids and glasses is a more collective and diffusive process, where chain actions occur at many atoms linearly connected [19]. The reality of "free-volume" is closer to the "distributed free-volume" picture of Argon [20]. Therefore, while the concept of atomic cage is correct, an atom does not come out of a cage by a big jump as in the free-volume model, but by gradually changing the neighbours.

Although some assumptions of the model are not correct, the concept is useful and intuitive. Indeed in glass science the temperature at which the rapidly cooled glass freezes is known as the fictive temperature, T_f. Since changes in specific volume of a liquid during cooling are linearly related to T_f, free-volume is a convenient measure of the fictive temperature, and therefore expresses the degree of relaxation in the glass [21].

1.1.6 Crystallization of a metallic glass

The driving force for any transformation is the difference in free energy (usually Gibbs free energy, G) of the final and initial states, and is thus determined by thermodynamic parameters appropriate to large regions of the phases concerned. At temperatures above the melting temperature, T_m, the liquid is in a thermodynamically stable state since Gibbs free energy is in a minimum for that atomic configuration. However, when the system is cooled, crystallization may occur because the crystalline solid is the atomic configuration with lower Gibbs free energy at $T < T_m$. If the cooling rate is high enough, crystallization can be suppressed (as mentioned above) and the supercooled liquid becomes a glass at T_g. Therefore, a glass is a metastable state resistant to all possible fluctuations, and any transformation path must pass through states of higher free energy to reach the crystalline state. There is a critical configuration which must be attained if the crystalline state has to be reached, and the increase in free energy required to form this critical configuration determines the time taken to make the unit step. There is thus an activation energy, E_a, for the process which must be supplied by a local fluctuation in the thermal energy of the system.

The crystallization process of a metallic glass is a nucleation and growth transformation process. If the activation energy for nucleation is overcome, nucleus of a crystalline phase must be formed and subsequent growth may take place. If a metallic glass is heated at temperatures near T_g, thermal fluctuations may be high enough to overcome the energy barrier for nucleation. Then, the velocity of transformation may be dependent both on the rate at which stable nuclei form and on their subsequent growth rates. The activation energy for nucleation is an important rate limiting factor, but in condensed phases (i.e. metallic glass) the activation energy for atomic migration or diffusion is usually equally important. In fact, the kinetics of growth in the crystallization of a metallic glass may be interface or diffusion controlled, typically similar to the mentioned in section 1.1.1.2.

1.1.6.1 Johnson-Mehl-Avrami-Kolmogorov (JMAK) model

The transformation kinetics from a phase α to a phase β in a metallic alloy at a constant temperature, T, may be described by the Johnson-Mehl-Avrami-Kolmogorov (JMAK) model [22-26]. In this model, the transformed fraction of the new β phase, x_β, is related to the time, t, by the following equation

$$x_\beta(t) = 1 - \exp(-(K(T)\cdot(t - t_0))^n) \qquad \text{eq. 1.13}$$

where $K(T)$ is called the rate constant, t_0 is the induction time period, that is the time needed to form a transformed β region, and n is the Avrami exponent. The value of the Avrami exponent may be related with the characteristics of the transformation. In general, n may be divided in two contributions $n = n_n + n_g$, where n_n depends on the nucleation rate and n_g on the growth rate. Therefore, $n_n = 0$ indicates a null nucleation rate and $n_n = 1$ a constant nucleation rate. On the other side, n_g may be defined as $n_g = b \cdot p$, where p is the dimension of the growth and b indicates interface controlled growth if $b = 1$ or diffusion controlled growth if $b = ½$ [2]. However, it is evident that a kinetic investigation which is limited to the establishment of the value of n most appropriate to the assumed growth law does not, as once assumed, give sufficient information to be deduce the growth habit.

Although the JMAK model is widely used in the crystallization of metallic glasses, some essential limitations must be taken into account [2]. These limitations are:

i) crystallization is considered in an unlimited medium,

ii) the nucleation rate does not depend on the local microstructure,

iii) the existence of a critical radius of nuclei is neglected,

iv) the growth rate of nuclei does not depend on the local chemical composition and its change during crystallization.

1.1.7 Mechanical properties of Metallic Glasses

1.1.7.1 Elastic and Anelastic Behaviour

The usual assertion made in discussing the elastic behaviour of metallic glasses is that these amorphous materials behave isotropically, by virtue of a random disordered structure. However, amorphous materials are not necessarily structurally isotropic, and anisotropic properties can result if directional preparation or treatment conditions imprint a directional character on the structure. Furthermore, the deviation from linearity at stresses lower than the yield strength in the stress-strain curves shows the relative large anelasticity of metallic glasses.

The disordered structure of a metallic glass means that atoms exist in a range of local atomic environments. Consequently, not all atoms experience the same displacement in elastic deformation, even if they belong to the same species [27]. For instance, Weaire et al. [28] showed that allowing atomic relaxation in a model calculation reduced the shear modulus by 33% compared to a model in which no relaxation was permitted. This result suggested that anelastic processes might be occurring during nominally elastic deformation. The atomic relaxations consist of topological rearrangements within the atomic near-neighbour environment in which an atom switches one of its atomic near-neigbours in preference for another atom in the second nearest-neighbour shell [29]. Therefore, if elastic deformation occurred within the first neighbour-shell, the elastic modulus would be comparable to that of crystalline materials of similar composition. However, the entire structure gets the benefit of the added deformation due to the atomic rearrangements and the elastic modulus of metallic glasses is lower than their crystalline counterparts [27]. Furthermore, Hufnagel et al. [27] have observed by in-situ structural studies that with increasing load the average atomic hydrostatic stress $<p>$ increases, but overall p becomes more uniform. This effect may come from the deformation of regions of locally large dilatation, which in the unloaded state are regions of unusually low p. As the load increases, these are the regions in which the atomic rearrangements described above occur. This brings the local p for these regions closer to the overall mean $<p>$, thus reducing $<p^2>$. A reduction in $<p>$, because it corresponds to a more uniform distribution of free volume, also implies a reduction in the entropy of the glass upon loading. This would imply that the stiffness of metallic glasses has entropic component, analogous to the entropic contribution in rubber elasticity.

As with most materials, the mechanism of anelastic deformation of metallic glasses is closely linked to their structure. In fact, it has been recognized that the free-volume which refers to the fraction of matter having a lower atomic coordination than that in a reference material having a dense random packing and the same composition, is of key importance for anelastic deformation. It is in these free-volume regions where mechanical coupling to the surroundings is weak that anelastic relaxations become possible by local atom rearrangements without affecting significantly the surroundings. It is interesting to note that such local relaxation

processes are not mono-energetic but require a distribution of activation energies, hence a distribution of free volume sites with different local atomic coordination [30-32].

1.1.7.2 Yield criterion for metallic glasses

Metallic glasses show strength differential between states of tensile and compressive loading, suggesting a pressure or normal-stress dependent yield criterion. Donovan [33] studied a $Pd_{40}Ni_{40}P_{20}$ glass in tension, compression and pure shear. This study identified a compression/tension strength differential of 23%. Furthermore, it is well-known that the fracture angles between the stress axis and the shear plane of metallic glasses always deviate from 45º and also show a differential fracture angle when tested in tension or compression [34].

The Mohr-Coulomb criterion has been suggested as a description for yielding of metallic glasses since it depends not only on the applied shear stress, τ, but also on the stress normal to the shear displacement, σ_n:

$$\tau_y = \tau_0 - \alpha\sigma_n \qquad \text{eq. 1.14}$$

Here, τ_y is the effective shear yield stress, τ_0 is a constant, and α is a system-specific coefficient that controls the strength of the normal stress effect.

Atomistic simulations of metallic glass deformation under multiaxial stress states found a pronounced asymmetry between the magnitudes of the yield stresses in tension and compression [35]. Therefore, Schuh and Lund concluded that simulated amorphous metals plastically yield in a manner consistent with the Mohr-Coulomb criterion, and that this behaviour is intrinsic to the atomic-scale processes involved in metallic glass deformation.

1.1.7.3 Plastic deformation and shear transformation zones

In metallic glasses, the plastic response occurs in two distinct regimes:

i. Homogeneous flow, in which each volume element of the material contributes to the strain, resulting in uniform deformation for a uniformly stressed specimen. Homogeneous flow occurs at low stresses and temperatures near and above the glass transition. It is measured in creep or stress relaxation tests.

ii. Inhomogeneous flow, where the deformation is localized in discrete, thin shear bands, leaving the rest of the material plastically undeformed. Inhomogeneous flow occurs at high stresses and low temperatures and is observed in tensile/compression tests, hardness tests and cold working processes such as rolling and wire drawing.

However, the deformation mechanism of plastic flow is, for any combination of stress and temperature, the same. In the view of shear transformation zone (STZ) type models [20] it is envisioned that the fundamental unit of plastic flow is the same for both regimes, and only the spatial distribution of these units is influenced by changes in stress, strain rate and/or temperature.

Spaepen first proposed a free-volume theory to account for plastic deformation at any stress, rate and/or temperature [36]. The original work of Argon extended the free volume model by introducing the concept of shear transformation zone (STZ) [20]. This model depicts glass deformation as a collective effect arising from the operation of many small atomic-scale shear events, in which a group of atoms collectively shuffle in a shear mode under the combined action of stress and temperature. The physical basis for such local shear events was provided by early simulations of amorphous systems [37,38] and more recent simulations have continued to support this picture of glass plasticity [39].

The relation of anelastic deformation with plastic deformation in metallic glasses was accounted by Argon [20]. Anelastic local transformations can be thermally assisted under applied shear stresses and a threshold stress, τ_0, would be sufficient to plastically deform this STZ. Therefore, the free energy for activation of flow under a given applied shear stress, τ, less than τ_0 that can transform a STZ at a terminal rate governed by inertia effects alone, can be obtained by the difference in free energy between the stable and unstable equilibrium positions of the system

$$\Delta G = \Delta F - \Delta W \qquad \text{eq. 1.14}$$

ΔF and ΔW are respectively the changes in Helmholz free energy of the system and the deformation work done on the system. Finally, the rate of activation of the STZ is governed by the availability of thermal fluctuation equalling or exceeding this required amount of ΔG. It is expected that the sites of largest free volume will have the smallest free energy barrier for shear transformation, and that sites with smaller free volume will have increasingly larger free energies for rearrangement.

Under a small applied stress at temperatures well below T_g, only the few and isolated free-volume sites with the smallest free energies can be transformed in meaningful times of laboratory experiments while much of the background structure acts substantially as an elastic medium. This produces delayed elasticity through which the structure becomes mechanically polarized with only a minimum of accompanying irrecoverable deformation. Under substantially higher stresses, larger fractions of STZ's with higher threshold stresses can be transformed into sheared states until at a certain well defined stress the shearable STZ's give contiguously sheared regions throughout the volume. At a certain stress range, the elastic background is removed, i.e. the reverse reaction against the applied stress makes a totally negligible contribution, resulting in plastic deformation.

In order to quantify the plastic deformation in a metallic glass and using the connection of anelastic relaxations with the STZ's, Argon calculated the Helmholtz free energy required to

sustain a local shear strain γ_0 for a STZ of volume Ω_0 in terms of the elastic properties of the glass obtaining

$$\Delta F_0 = \left[\frac{7-5\nu}{30(1-\nu)} + \frac{2(1+\nu)}{9(1-\nu)}\beta^2 + \frac{\tau_0}{2\gamma_0\mu(T)} \right] \cdot \mu(T)\gamma_0^2\Omega_0 \qquad \text{eq. 1.15}$$

where $\mu(T)$ and ν are the temperature-dependent shear modulus and Poisson's ratio of the glass, respectively. The parameter β is a numerical constant that describes the volumetric dilatation of the STZ relative to its shear distortion, and is about equal to unity for amorphous metals. It is assumed that this elastic shear strain energy is short lived and that it may be dissipated soon after the transformation by other surrounding transformations resulting in loss of memory for the initial state in the first region. But as stated above, plastic deformation may occur at sustained shear stresses, even below τ_0. Thus, for a metallic glass subjected to a shear stress τ, the strain rate resulting from the superposition of many individual STZ operations is then given as

$$\dot{\gamma} = \alpha_0 \nu_0 \gamma_0 \cdot \exp\left(-\frac{\Delta F_0}{kT}\right) \sinh\left(\frac{\tau\gamma_0\Omega_0}{kT}\right) \qquad \text{eq. 1.16}$$

in which α_0 is a constant incorporating the fraction of material that is capable of undergoing shear transformation and ν_0 is the natural frequency (attempt rate) of the STZ's.

Argon originally derived eq. 1.16 for high temperature viscous flow, in which STZ's are roughly spherical and there is no spatial correlation between them. He proposed that at lower temperatures (where shear banding occurs) the STZ might change character somewhat, transitioning from spherical to disk-shaped, with a somewhat different value for ΔF_0.

Recently, Johnson and Samwer [40] have introduced the concept of cooperative shear model (CSM) to describe plastic yielding of metallic glasses in the glassy state below T_g. Following the idea of STZ cooperative movements, the elastic energy of an STZ is described by a periodic elastic energy density and the barrier W for shear flow is related by a scaling law to a universal critical yield strain γ_{C0}, the shear modulus μ for a fixed glass configuration, and the effective volume of cooperative shear zones (CSZ) $\Omega_{eff} = \zeta\Omega$.

$$W = \left(\frac{8}{\pi^2}\right)\mu\gamma_{C0}^2\zeta\Omega \qquad \text{eq. 1.17}$$

The core volume of CSZ is Ω, and ζ is an "Eshelby" factor correcting for matrix confinement of the CSZ. This relation predicts that the barrier height for shear flow for a given glass or liquid configuration is proportional to μ. Therefore, yielding occurs when the applied stress causes a critical density of "minimum" barrier STZ's to become unstable.

Furthermore, recent molecular dynamic simulations [41] have shown that plastic deformation occurs through the movement of mobile clusters of the order of 10-15 Å within a rigid glass matrix, which are interconnected via single strings of mobile atoms. Both clusters and interconnections together seem to form a dynamic network of plastic deformation, which controls the macroscopic behaviour. Furthermore, comparable networks of clusters and

interconnects are observed for any strain, strain rate and temperature below the corresponding yielding point. Only the number of clusters and the distance that atoms move plastically seems to vary, increasing for higher strains or temperatures.

1.1.7.4 Factors determining the metallic glasses strength

Interestingly, there exist remarkable similarities between the physical processes of plastic deformation and glass transition of metallic glasses. Both phenomena are facilitated by collective atomic motions, which require sufficient energy to overcome the bonding force between atoms and result in an increase of the free volume [20,21,36]. Whereas the thermal energy for glass transition spreads around the entire body of the solids during heating, the mechanical energy of shearing at low temperatures (below T_g) is highly confined in the localized shear bands in metallic glasses. Following this reasoning, Yang et al. [42] have recently found a relation for the strength of metallic glasses which may be expressed as

$$\sigma_f = 55\frac{\Delta T_g}{V} \qquad \text{eq. 1.18}$$

where ΔT_g is the temperature difference between T_g and room temperature, σ_f is the fracture strength and V is the molar volume. This simple equation indicates that the strength of metallic glasses at room temperature is governed by both the glass transition temperature and the molar volume.

Given a similar energy density between localized shear deformation and glass transition, the heat dissipated from STZ's should be able to raise their temperatures close to T_g. In other words, a stress slightly higher than the yield strength will be able to increase the shear band temperature to T_g, which will result in rapid viscosity drop and significant softening inside the shear bands. Temperature raise above T_g in shear bands have recently shown by Lewandowsky and Greer [43].

1.2 Metallic-Glass-Matrix Composites

Below T_g, plastic deformation of metallic glasses occurs by the initiation and propagation of shear bands [20,36]. Many important mechanical properties of metallic glasses, including ductility and toughness, are therefore determined by the individual and collective behaviour of shear bands. Although, metallic glasses show high fracture strength, the final fracture is produced after yielding by the propagation of a shear band along the specimen after a little percent of deformation. Therefore, the ductility of metallic glasses is severely limited by their plastic deformation mechanism.

There have been many studies of shear band behaviour and structure, and several theories of shear localization in metallic glasses have been proposed [20,21,36,40,41]. Therefore, the understanding of how the structure of metallic glasses affects shear band initiation and propagation becomes every time more accurate.

However, several groups have explored the behaviour of composite materials in order to further improve the ductility of metallic glasses in the inhomogeneous flow regime. These composite materials consist of:

i. crystalline second phases in an amorphous metallic matrix,

ii. metallic glasses decomposed in two amorphous phases.

Any of these structures may provide higher ductility than a monolithic metallic glass; however the followed strategy is different for any of the above morphologies.

1.2.1 Crystalline Second Phase in an Amorphous Matrix

Obtaining a crystalline second phase in a metallic-glass-matrix is possible by different routes:

a) a crystalline phase is precipitated from the melt during cooling or by partial devitrification of the metallic glass (in situ composites)

b) the reinforcing phase is physically added to the metallic glass prior to casting (ex situ composites).

1.2.1.1 In situ composites

I) Precipitated from the melt during cooling

The precipitation of a second phase during casting gives rise to a two-phase microstructure consisting of a metallic glass matrix reinforced with a crystalline second phase. Usually, this kind of alloys are prepared by forcing the precipitation of one of the constituent elements to a crystalline phase, or by a mix of a good glass former composition plus a high melting element which will precipitate in form of a second phase [44]. While in the first case the alloys are prepared by simple Cu-mould casting, in the second case, the alloys are prepared by a two-step process before casting. One of the elements of the glass composition is mixed with the high melting element and later, the rest of the elements are melted together obtaining a master alloy. In the first step, the high melting element and the other element form a supersaturated

solid solution, in which the high melting element is dissolved in the structure of the other element. When this ingot is melted together with the other elements, the high melting alloy precipitates out to form micrometer sized particles. These particles have a very high melting point, so it is likely that they remain solid when the ingot is melted and cast to form the metallic-glass-matrix composite. During casting, these small particles apparently agglomerate to form larger particles. The result of this processing route is shown in Fig. 1.4.

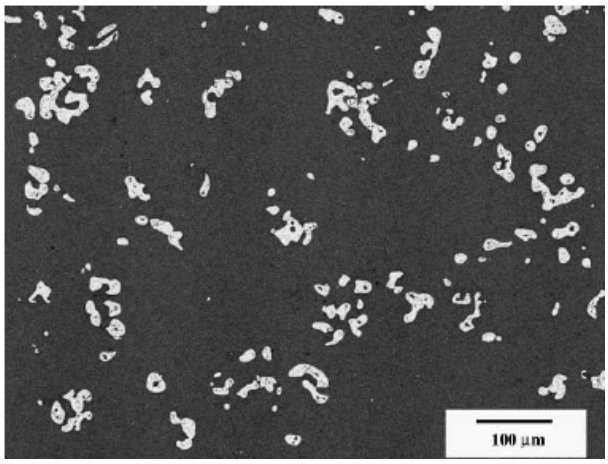

Figure 1.4. Backscattered electron micrograph of as-cast sample of $Zr_{56}Ni_8Cu_{16}Ta_{10}Al_{10}$ showing Ta micron-scale particles dispersed in amorphous matrix [44].

The mechanical properties of these metallic-glass-matrix composite differ from the monolithic metallic glasses. In fact, these second-phase particles cause the plastic strain to be distributed over a larger volume of material, delaying the onset of fracture and therefore, increasing the plasticity of the alloys [45-47]. Unlike conventional metal-matrix composites, the reinforcing phase in these alloys typically has a lower yield stress than the matrix. Recently, Ott et al. [47] have shed light on the micromechanics of deformation of an in situ formed metallic-glass-matrix composite. During loading, the particles experience plastic deformation, while the stronger glass matrix remains elastic, leading to the development of a plastic misfit strain in both phases. At applied stresses below the yield stress of the matrix, the matrix yield criterion is only satisfied in the regions immediately around the particles, as shown in their finite element modelling of Fig. 1.5. Thus, if a shear band initiates at the particle and propagates away, it will quickly encounter a region where the yield criterion is not satisfied and the shear stress is insufficient to sustain shear band propagation. This situation is exacerbated for systems of multiple particles, in which the stress state is highly inhomogeneous and there can even be regions where the applied stress is higher than the von Mises stress. In addition to reducing the driving force for shear band propagation under these conditions the plane of maximum shear stress can deviate locally from 45º, creating an opportunity for shear bands to be deflected. Therefore, it is expected that it is more difficult for shear bands to propagate under these conditions, and that this may explain why the composites can exhibit significant plastic strains prior to failure.

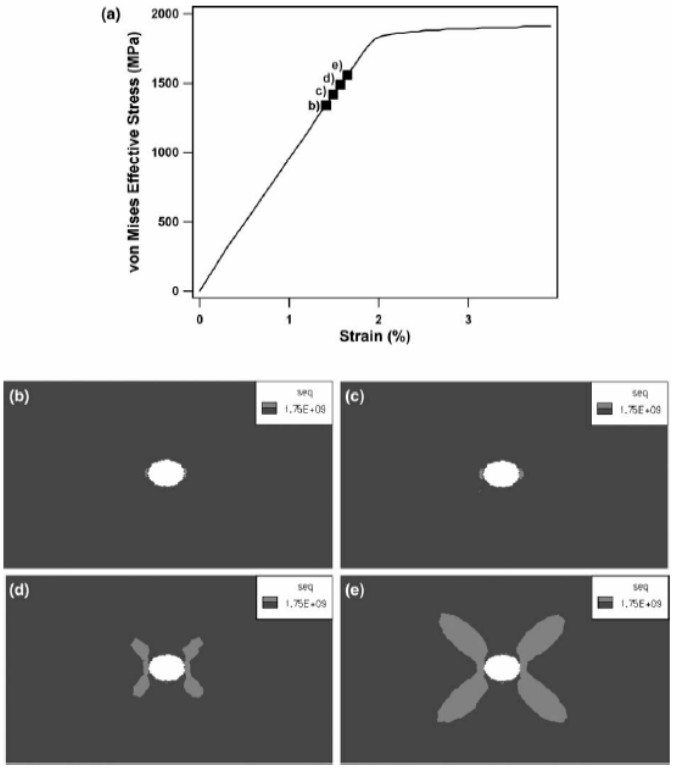

Figure 1.5. Contour maps of von Mises effective stress for a single particle (white) embedded in an amorphous matrix. The images show the results for successive displacement steps increasing from (b) through (e). The light coloured areas correspond to regions in the matrix where the von Misses stress is greater than 1750 MPa (the matrix yield stress). The corresponding stress for the contour maps is noted on the stress–strain curve (a), [47].

II) Devitrification of the metallic glass

Metallic glasses are in a metastable state, as explained in section 1.1.6. Therefore, heat treatments below or above T_g may lead to the crystallization of the metallic glass. In order to produce a composite material, the nucleation and growth mechanisms of the crystallization of a metallic glass must be understood. The importance of distribution of a specific crystalline/quasicrystalline phase and effects due to remaining amorphous matrix, which may change its composition or the extent of free volume/relaxation during crystallization, may be studied for each alloy and heat treatment since the mechanical properties depend on them and their interacting effects [48,49].

A typical example of these types of alloys is the Al-based metallic glasses. A large number of studies have been reported that examine the first stage of crystallization in these alloys, when pure α-Al crystals form in the glass during heat treatment [50,51]. The first stage of crystallization, when α-Al crystals form, is thus fairly well understood, with an early period of crystal nucleation and rapid growth followed by a period with no more crystal nucleation and where crystal growth slows to very low rates or stops. Such slowing of growth has been interpreted in terms of the rejection of solute

from the pure α-Al crystals into the surrounding glassy matrix or in terms of the overlapping of such diffusion fields from the nearby crystals.

The influence of the distribution and size of the α-Al crystallites on the microhardness and ductility of an $Al_{90}Ni_4Ce_6$ metallic glass is studied in [49]. The appearance of nanosize α-Al crystals inside the glass after a thermal treatment initially increases the hardness while the alloy remains ductile. For longer annealing times, the nanocrystals do not grow and their amount remains almost the same, however, the alloy becomes brittle. It has been suggested that this loss of ductility is due to changes of the extent or morphology of crystallization or may instead be caused by changes in the glassy matrix.

1.2.1.2 Ex situ composites

The addition of a high melting temperature element or composite such as W, WC, SiC, Ta, C, etc… directly in the melt is used to improve the mechanical properties of the monolithic metallic glass. They may be added in the form of wire [52] or micrometer sized particles [53]. Another route to produce ex situ composites consists of adding reinforcing particles to amorphous powders and a posterior warm extrusion of the composite particles [54,55].

In the fabrication of ex situ composites directly in the melt, it is important that the reinforcement material does not react significantly with the matrix glass, the glass must wet well enough the reinforcement to make composites with good mechanical integrity and the thermal expansion coefficients of both materials should not be too different [52].

This composites show improved ductility compared to the monolithic glass depending on the volume fraction and the nature of the reinforcement material [52-55]. Therefore, the mechanisms of plastic deformation are also dependent on both parameters.

1.2.2 Decomposition of the Amorphous Matrix into two Amorphous Phases

Probably a metallic glass which has suffered decomposition into two amorphous phases of different composition may not be considered as a metallic-glass-matrix composite. However, the morphology exhibited by these alloys allows them to show different properties compared to a monolithic metallic glass.

The decomposition of a metallic glass into two amorphous phases is due to immiscibility composition gaps. Phase separation (or decomposition) occurs in a liquid when the free energy of the decomposed liquid is lower than in the homogeneous one. In a liquid composed of two elements A and B, the Helmholtz free energy of mixing, F_{mix}, may be related with the internal energy of mixing, U_{mix}, and the entropy of mixing, S_{mix}, at any temperature, T, by the following equation

$$F_{mix} = U_{mix} - TS_{mix} \,. \qquad \text{eq. 1.19}$$

The entropy of mixing in a ideal binary system for any given composition, c_A, is expressed as

$$S_{mix} = -Nk[c_A \cdot ln\ c_A + (1-c_A) \cdot ln\ (1-c_A)]\ , \qquad \text{eq. 1.20}$$

where N is the number of particles in the system. If a hypothetic AB system presents a higher U_{mix} for the homogeneous phases of the A and B elements than for any other composition, F_{mix}, it may present a minimum in two compositions (c_{A1} and c_{A2}) at a given temperature, as shown in Fig. 1.6. Therefore, an alloy of composition higher than c_{A1} and lower than c_{A2} will decompose into two liquids of different composition.

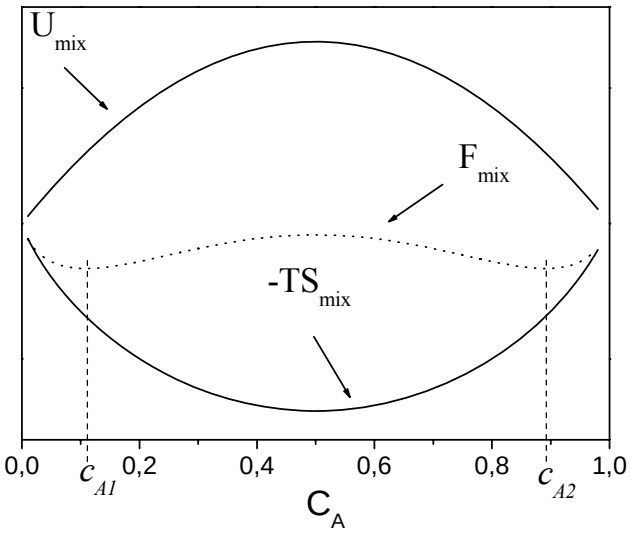

Figure 1.6. Hypotetic representation of F_{mix}, U_{mix}, and $-TS_{mix}$ for a binary A-B system in the liquid state at a given temperature T.

When the temperature of the system is increased, the $-TS_{mix}$ minimum becomes deeper and at a certain temperature, F_{mix} will present only one minimum and at that temperature the liquid will show a homogeneous phase. If a system shows a minimum temperature for phase separation lower than the melting temperature, the undercooled liquid will tend to decompose. The decomposition of the liquid may take place either during cooling if it is not fast enough or during a heat treatment below or above T_g.

The morphology of a decomposed glass depends on the mechanism and the kinetics of the phase separation. Therefore, two mechanisms can induce the decomposition of the liquid or glass and both can be classified according to their Helmholtz free energy dependence on the composition. Gibbs demonstrated that a phase is stable or metastable for infinitesimal fluctuations in the composition if the chemical potential of an element is higher for higher amounts of the element in the composition, or for $\partial^2 F/\partial c^2 > 0$. In this case, an activation energy, E_a, for the process must be supplied and hence, the phase separation will take place by a nucleation and growth process. However, if the system F_{mix} behaves $\partial^2 F/\partial c^2 < 0$ like with the composition, the homogeneous liquid or glass is unstable to any thermal fluctuation, and hence, the decomposition of the liquid does not require any activation energy, and only the diffusion of the constituent elements restricts the process. This second decomposition mechanism is called spinodal decomposition.

Recently, several systems presenting decomposition in the amorphous state have been studied because of their enhanced mechanical properties [56-58]. These alloys show larger plastic strain to failure than a monolithic metallic glass. The inhomogeneities in composition ultimately promote the nucleation of shear bands throughout the bulk material and enable their branching. The intersection of shear bands decreases their sharpness, hinders their rapid propagation and increases the flow stress of the material leading to enhanced plasticity.

1.3 Nanocrystalline Materials

Nanocrystalline materials are single or multi-phase polycrystals with nano scale grain size. At the upper limit of this regime, the term "ultrafine grain size" is often used (grain sizes of 250-1000 nm). Nanocrystalline materials are structurally characterized by a large volume fraction of grain boundaries, which may significantly alter their physical, mechanical, and chemical properties in comparison with conventional coarse-grained polycrystalline materials, which have grain sizes usually in the range 10-300 μm. Figure 1.7 shows a schematic depiction of a nanocrystalline material. The grain-boundary atoms are white and are not clearly associated with crystalline symmetry.

As the grain size is decreased, an increasing fraction of atoms can be ascribed to the grain boundaries. We can consider two types of atoms in the nanocrystalline structure: crystal atoms with neighbour configuration corresponding to the lattice and boundary atoms with a variety of interatomic spacing. As the nanocrystalline material contains a high density of interfaces, a substantial fraction of atoms lie in the interfaces. Assuming the grains have the shape of spheres or cubes, the volume fraction of interfaces in the nanocrystalline material may be estimated as $3\Delta/d$ (where Δ is the average interface thickness and d is the average grain diameter). Thus, the volume fraction of interfaces can be as much as 50% for 5 nm grains, 30% for 10 nm grains, and about 3% for 100 nm grains.

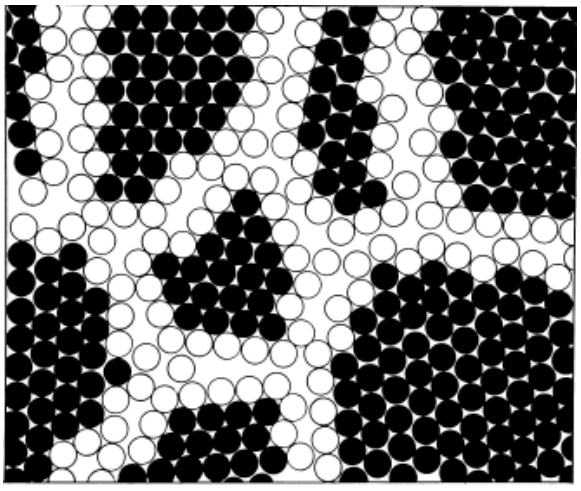

Figure 1.7. Two-dimensional model of a nanostructured material. The atoms in the centers of the crystals are indicated in black. The ones in the boundary core regions are represented as open circles [59].

Due to this high volume fraction of atoms forming the grain boundaries, nanocrystalline materials may exhibit increased strength/hardness, improved toughness, reduced elastic modulus and ductility, enhanced diffusivity, higher specific heat, enhanced thermal expansion coefficient, and superior soft magnetic properties in comparison with conventional polycrystalline materials.

1.3.1 Classification

The number of dimensions in which the material has nanometer modulations classifies the nanocrystalline materials. Thus, they can be classified into (a) layered or lamellar structures, (b) filamentary structures, and (c) equiaxed nanostructured materials. A layered or lamellar structure is a one-dimensional (1D) nanostructure in which the magnitudes of length and width are much greater than the thickness that is only a few nanometers in size. A rod-shaped nanostructure that can be termed filamentary is a typical two-dimensional (2D) nanostructure if the length is substantially larger than width or diameter, which are of nanometer dimensions. Equiaxed grains of nanometer size form a three-dimensional (3D) nanostructure and are termed nanostructured crystallites.

The nanostructured materials may contain crystalline, quasicrystalline, or amorphous phases and can be metals, ceramic, polymers or composites. Finally, it is worth mentioning that Gleiter has further classified the nanostructured materials according to the composition, morphology and distribution of the nanocrystalline component [59].

1.3.2 Microstructure

From the stated before and following Fig. 1.7, it is clear that nanocrystalline metals can be considered to consist of two structural components small crystallites and interfacial components. The small crystallites are formed of crystalline structures with long-range order and different crystallographic orientations, the interfacial components are a network of intercrystalline regions the structure of which differs from region to region. The interatomic spacing in the interfacial component have a wide distribution and further the average atomic density is considerably less than the crystal density depending on the type of chemical bonding between the atoms.

In nanocrystalline single-phase alloys and pure metals, the most important structural parameter is the grain size and, therefore, an accurate determination is important. Both direct (imaging) and indirect (scattering) techniques have been employed to determine the grain sizes. Nanocrystalline alloys composed of more than one phase can show different morphologies. For example, a microstructure of equiaxed grains of different phase can be formed by i.e. the crystallization of an amorphous alloy [60] or by mechanical alloying [61], and a eutectic

microstructure with lamellae width of nanometers may be also obtained by rapid quenching technique [62].

1.3.2.1 Atomic structure of the grains

The structure of the crystallites in nanocrystalline materials has been normally accepted to be the same as in a coarse-grained material. Consequently, there have not been many investigations into this aspect. High-resolution transmission electron microscopy has shown that nanocrystalline materials consist of small crystallites of different crystallographic orientation separated by grain boundaries. Even though not frequently reported, the grains contain a variety of crystalline defects such as dislocations, twin boundaries, multiple twins, and stacking faults.

Lattice distortions in the crystallites may occur in nanocrystalline materials like in coarse-grained materials, but some properties of the nanocrystalline materials produce these distortions. It is now well established that the solid solubility of elements is usually higher in the nanocrystalline state than in the coarse-grained condition. This change in solid solubility can lead to changes in lattice parameters. Furthermore, a significant change in vacancy concentration can also affect the lattice parameters. It has also been noted that nanocrystalline materials have large mean square lattice strains, which increase systematically with a decreasing grain size. This strain appears to depend on the thermal and mechanical history of the specimen, suggesting that at least part of the strain is not intrinsic to the nanocrystalline state [63].

1.3.2.2 Atomic structure of the grain boundaries

The structure of the grain boundaries has received a lot of attention, especially to decide whether it is different in the nanocrystalline and coarse-grained materials of the same composition. The grain boundary structure determines de diffusivity, and consequently the rate of deformation by grain boundary diffusion (Coble creep) and the rates of sintering and grain growth. The nature of atomic structure of the grain boundaries seems to be solved and it is accepted that it is similar to the coarse-grained materials. Although Gleiter [64] and co-workers showed that the grain boundaries in nanocrystalline materials may be random, the incomplete densification of the material may explain their observed results. Later, Siegel [65] has shown that the grain boundary structure in nanocrystalline materials is similar to that in coarser-grained conventional material based on the evidence from X-ray diffraction, EXAFS, Mössbauer spectroscopy, Raman spectroscopy, HRTEM images and computer simulations. So, one can assume a boundary a few atomic distances thick. However, it is safe to assume that the number of grain-boundary ledges is reduced because of the size. The reorientation/rotation of the nanosized boundaries is also significantly enhanced in comparison with conventional boundaries [66].

1.3.3 Elastic and Plastic Deformation of Nanocrystalline Materials

Because of the very fine grain sizes and consequent high density of interfaces, nanocrystalline materials exhibit a variety of properties that are different and often considerably improved in comparison with those of conventional coarse-grained materials. But it is becoming increasingly clear that the early results on the properties of nanocrystalline materials are not reliable, mainly due to the significant amount of porosity present in those samples.

1.3.3.1 Yield Stress

Grain size is known to have a significant effect on the mechanical behaviour of materials, in particular, on the yield stress. The dependence of yield stress on grain size in metals is well established in the conventional polycrystalline range (micrometer and larger sized grains). Yield stress, σ_y, for materials with grain size d, is found to follow the Hall-Petch relation,

$$\sigma_y = \sigma_0 + kd^{-1/2} \qquad \text{eq. 1.21}$$

where σ_0 is the lattice friction stress to move individual dislocations and k is a material dependent constant. Even though the above relationship was obeyed by a number of nanocrystalline materials, some instances are also available when, below a critical grain size, the hardness was found to decrease with a decreasing grain size [67]. That is, the slope k has a negative value and this has been called as inverse Hall-Petch relationship. Furthermore, a more general formulation is used with exponent $-n$, where $0.3 \leq n \leq 0.7$, to account deviations in the value of n.

The Hall-Petch trends for a range of grain sizes from the micro to the nanocrystalline are plotted in Fig. 1.8 for four different metals: Cu, Fe, Ni and Ti [66]. Note that the data points in the conventional coarse-grained state for most of these plots overlap while they are more spread out in the nanocrystalline range. The Hall-Petch curve for the nanocrystalline range clearly shows a deviation from the regular trend in the microcrystalline range; there is a significant decrease in the slope for small grain sizes. However, there is no clear evidence on the nature of the curves at grain sizes below 10-15 nm. It seems that there is insufficient information to validate the existence of the negative Hall-Petch effect. The most probable behaviour is that the yield strength plateaus below a critical grain size. The real trend is still to be determined along with the knowledge of whether it varies for different materials.

In fact, the Hall-Petch relationship was derived on the basis of strengthening resulting from dislocation pile-ups at physical obstacles like grain boundaries. Nanocrystalline materials have extremely small grain sizes, therefore, enough number of dislocations will not generate and migrate to have a pile-up, and so it is doubtful if strengthening could occur by this mechanism; other mechanism may have to be invoked. While some people accept that the

inverse Hall-Petch relationship (i.e., a decrease of strength for decreasing crystallite size) is real and some theoretical explanations have been offered for its occurrence, others believe that this is an anomaly.

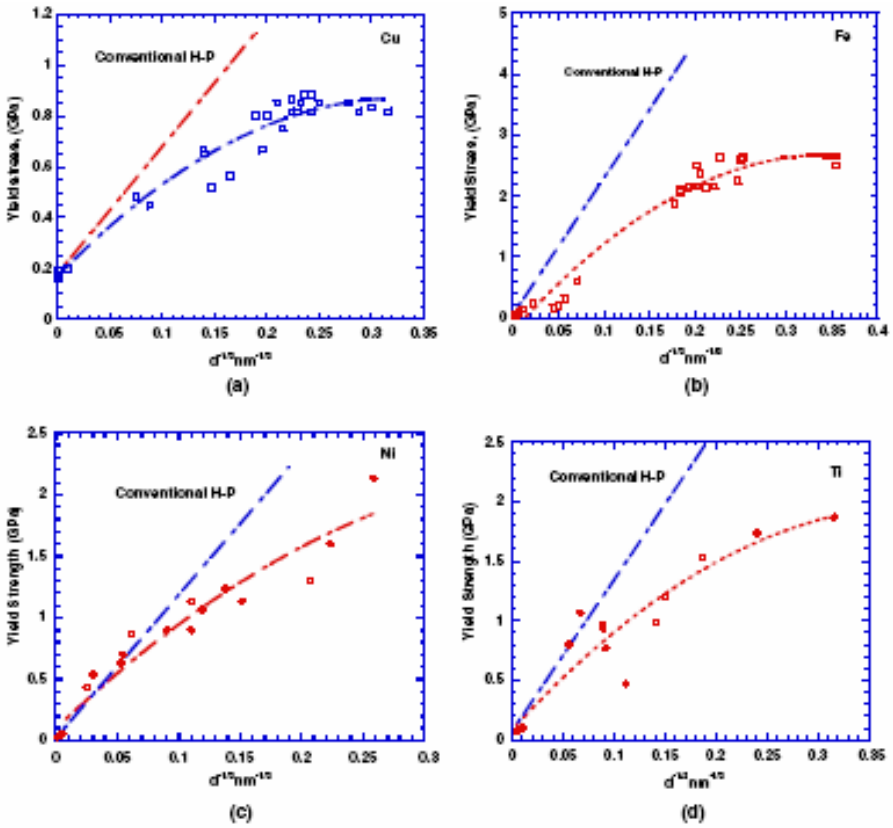

Figure 1.8. Plots showing the trend of yield stress with grain size for different metals as compared to the conventional Hall-Petch response: (a) Cu, (b) Fe, (c) Ni and (d) Ti, [66].

1.3.3.2 Ductility and Toughness

It is well known that grain size has a strong effect on ductility and toughness of conventional grain size (>1μm) materials. For example, the ductile/brittle transition temperature in mild steel can be lowered about 40ºC by reducing the grain size by a factor of 5. Grain size can make crack propagation more difficult and therefore increase the apparent fracture toughness in conventional grain size materials. But materials that exhibit ductile behaviour when tested with a coarse-grained size microstructure show reduced ductility -sometimes brittle behaviour- at the smallest nanometer grain sizes. This is presumably due to the inability of usual dislocation generation and motion to occur at these nanometer grain sizes. Furthermore, nanocrystalline metals are characterized by a low work-hardending rate, which is a direct consequence of the low density of dislocation encountered after plastic deformation. This low work hardening rate leads to tensile instability and a low tensile ductility.

However, nanocrystalline materials can show some ductility at room temperature if the plastic deformation mechanism is not based on the dislocation generation and motion. A grain

size distribution consisting of a 30% volume fraction of larger grains of 50 nm combined with smaller nano-scale grains exhibited more strain hardening and therefore more ductility than the same material with smaller grain size [68]. Dislocation activity occurred in the larger grains while the smaller grains provided the strengthening. Furthermore, it has also been shown that the ductility of a nanocrystalline material is enhanced by increasing significantly the density of growth twins by annealing [69].

1.3.3.3 Mechanisms of plastic deformation

Different mechanisms have been proposed for the plastic deformation in nanocrystalline materials. The more important are described below,

i. Pile-up break down: As the grain size is decreased, the number of dislocations piled up against a grain boundary decreases, at a fixed stress level, since this number is a function of the applied stress and of the distance to the source. Conversely, an increased stress level is needed to generate the same number of dislocations at the pile-up. At a critical grain size, we can no longer use the concept of a pile-up to explain the plastic flow.

ii. Grain-boundary sliding: Under an applied shear stress, one layer of grains slides with respect to the other, producing a shear strain in the process. Plastic deformation takes place by virtue of the top layer of grains translating to one direction with respect to the bottom layer of grains.

iii. Core and mantle model: The model is based on dislocation generation at or adjacent to grain boundaries and on the formation of work-hardened grain boundary layers. The existence of grain-boundary ledges with spacing of 10-100 nm provides an ample supply of nucleation sites of dislocations that, upon emission into the grains, cross-slip and multiply, creating a work hardened layer close to the grain boundaries. As the grain size is reduced, the ratio between volume fractions of the mantle and core increases, providing an increase in yield stress. At critical grain size, the ledges can no longer operate and do not promote plastic deformation in the nanocrystalline regime.

iv. Shear band formation: For all smaller grain sizes (d < 300nm) shear band development is often observed to occur immediately after the onset of plastic deformation. This has been correlated to changes in strain hardening behaviour at those grain sizes, since the ability to work harden by the increase in dislocation density is lost.

v. Mechanical twinning: Mechanical twinning and slip can be considered as competing processes. In FCC metals and alloys, the twinning stress is directly related to the stacking fault energy. The decrease in grain size is expected to render deformation twinning more difficult. At least, this is what conventional materials science predicts in the micrometer regime [66].

It is therefore surprising that molecular dynamic (MD) simulations by Yamakov et al. [70] predicted mechanical twinning in the deformation of a nanocrystalline aluminium-like metal, and later, first observation of twins in aluminium by Chen et al. [71] were carried out.

Although mechanisms for deformation twinning in nanocrystalline metals are not proposed, some preliminary comments are of order: (a) the conventional nucleation mechanism breaks down in the nanoscale; (b) there are local stress concentrations (triple points, etc.) that raise the stress significantly, propitiating twinning; (c) the partial dislocation separation increases in the nanoscale domain, aiding twinning. The last possibility is discussed in the next point.

vi. Grain boundary dislocation creation and annihilation: When the grain size is reduced to the nanocrystalline regime, the mean free path of dislocations generated at grain-boundary sources is severely limited. Rather than cross slipping and generating work hardening, these dislocations can run freely until they meet the opposing grain boundary, which acts as a sink. Thus, the dislocation density remains low throughout the plastic deformation process, and work hardening is not significant. Dislocations, which were generated at one grain boundary, run unimpeded until they encounter the opposing grain boundary. Grain boundary ledges are responsible for generation of plastic flow in the conventional polycrystalline regime. However, as the grain size falls below 20 nm, the grain boundaries will become virtually free of ledges, and intrinsic and extrinsic grain-boundary dislocations have to be pushed out into the grains. Another significant difference is that the mean free path of dislocations is limited by the grains size, and therefore dislocation reactions, cross slip, and other mechanisms of dislocation multiplication are effectively prohibited.

Although all these mechanisms may play a role under specific internal (grain size, composition …) or external (temperature, strain rate, stress state) parameters, a few seem dominant in the nanocrystalline regime. Therefore, three domains of grain size may be invoked:

a) $1\ \mu m > d > 100\ nm$: commonly referred as "ultrafine grain size, a core-and-mantle model seems to describe the response during plastic deformation.

b) $100\ nm > d > 20\ nm$: in this region, the H-P slope gradually decreases with decreasing d. The grain-boundary ledges can no longer supply dislocations in this regime because their spacing ($l < 30\ b$, b is the burger's vector of a dislocation) becomes large with respect to the grain size. The dislocations emitted from the grain boundaries can hardly cross-slip and multiply in the grains. Dislocations generated at grain boundaries can, in the lower limit of this size range, travel through the grains relatively unimpeded and annihilate in the opposing boundary. This can be carried out without significant work hardening, since the density remains constant. This leads to shear localization.

c) $20\ nm > d > 1nm$: the grain boundary effects dominate the deformation process in this regime. Grain-boundary sliding becomes important in this regime and has been identified by Conrad [72] as the principal mechanism. Grain-boundary sliding cannot occur by itself and associated plastic deformation is needed. This was demonstrated by computer calculations of Fu et al. [73] and shown in Fig. 1.9. A nanocrystalline copper with a grain size of 20 nm was used for the MD simulations. The grain-boundary shear strength was completely eliminated for one of the simulations, effectively creating a grain-boundary layer with zero viscosity. Although, one would expect that the material strength would drop to zero, the nanocrystalline material retained approximately 2/3 of its original mechanical response. Hence, one concludes that grain-

boundary sliding can contribute, at most, one-third of the plastic strain, under the most favourable conditions.

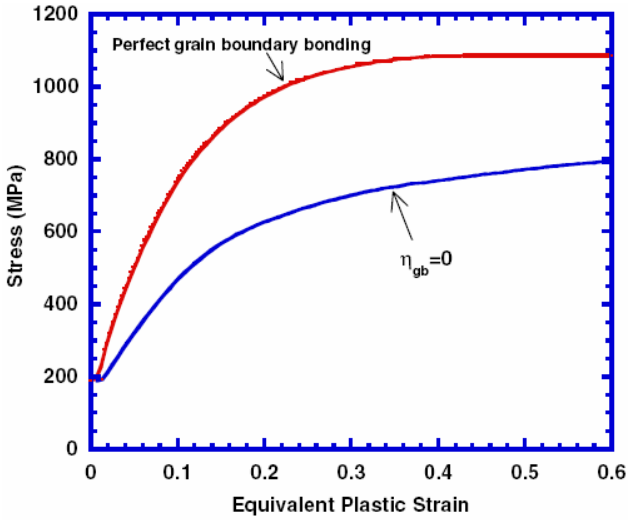

Figure 1.9. Computed mechanical response of nanocrystalline copper (d = 20 nm) assuming that grain boundaries have zero viscosity, and equivalent material with perfect grain boundaries [73].

The plastic deformation needed for grain-boundary sliding can be assisted by stacking faults and/or twinning. Chen et al. [71] have recently shown deformation twins in nanocrystalline aluminium. Aluminium has high stacking fault energy and a reduction of grain size makes twinning more difficult. However, there seem to be clear indications that there is a threshold grain size at which perfect dislocations decompose into partials [74]. This is because it is easier to emit a second partial dislocation from a boundary adjacent and at a twin separation from the first partial. Thus, once a partial is emitted, conditions become ripe for twinning. The mechanical twins observed and modelled by MD in nanocrystalline metals are only a few atomic layers thick and therefore only require a few partial dislocations gliding on parallel planes. Thus, the critical event for deformation twinning is the separation between partials.

References

[1] Christian JW, Haasen P, Massalski TB: Prog Mater Sci 1986; 30:81.

[2] Christian JW, The Theory of Transformations in Metals and Alloys, (2nd ed. Pergamon, Oxford, 1975).

[3] Turnbull D: Contemp Phys 1969; 10:473.

[4] Vreeswijk JCA, Gossink RG, Stevels JM: J Non-Cryst Solids 1974; 16:15.

[5] Cahn RW: Encyclopedia of Materials Science and Engineering, (Pergamon Press, Oxford, 1988, Collection: Advances in Materials Science and Engineering).

[6] Egami T, Waseda Y: J Non-Cryst Solids 1984; 64:113.

[7] Inoue A: Acta Mater 2000; 48:279.

[8] Zallen R: The Physics of Amorphous Materials, (John Wiley & Sons, New York, 1998).

[9] Mazurin OV: J Non-Cryst Solids 1977; 25:129.

[10] Egami T in: Amorphous Metallic Alloys, (Butterworth-Heinemann, London, 1983, Edited by: Luborsky FE).

[11] Miracle DB: Acta Mater 2006; 54:4317.

[12] Yavari AR: Nature 439:405.

[13] Doolittle AK: J Appl Phys 1951; 22:1471.

[14] Cohen MH, Turnbull D: J Chem Phys 1959; 31:1164.

[15] Turnbull D, Cohen H: J Chem Phys 1961; 34:120.

[16] Turnbull D, Cohen H: J Chem Phys 1970; 52:3038.

[17] Spaepen F, Turnbull D: Scripta Metall & Mater 1991; 25:1563.

[18] Bennett CH, Shone HE, Gustafson P: Phys Rev B 1979; 18:2027.

[19] Faupel F, Frank W, Macht M-P, Mehrer H, Naundorf V, Rätzke HR, et al: Rev Mod Phys 2003; 75:237.

[20] Argon AS: Acta Metall 1979; 27:47.

[21] Egami T: Intermetallics 2006; 14:882.

[22] Johnson MWA, Mehl KF: Trans Am Inst Min Metall Pet Eng 1939; 135:416.

[23] Avrami M: J Chem Phys 1939 7:1103.

[24] Avrami M: J Chem Phys 1940; 8:212.

[25] Avrami M: J Chem Phys 1941; 9:177.

[26] Kolmogorov AN: Izv Akad Nauk USSR Ser Mater 1937; 3:355.

[27] Hufnagel TC, Ott RT, Almer J: Phys Rev B 2006; 73:064204.

[28] Weaire D, Ashby MF, Logan J, Weins MJ: Acta Metall 1971; 19:779.

[29] Suzuki Y, Egami T: J Non-Cryst Solids 1985; 75:361.

[30] Ocelík V, Csach K, Kasardová A, Bengus VZ: Mater Sci Eng A 1997; 226-228:851.

[31] Kursumovic A, Cantor V: Scripta Mater 1996; 34:1655.

[32] Berry BS: Metallic Glass (American Society for Metals, Metals Park, OH, 1976).

[33] Donovan PE: Acta Metall 1989; 37:445.

[34] Zhang ZF, He G, Eckert J, Schultz L: Phys Rev Lett 2003; 91:045505.

[35] Schuh CA, Lund AC: Nature Mater 2003; 2:449.

[36] Spaepen F: Acta Metall 1977; 25:407.

[37] Argon AS, Kuo HY: Mater Sci Eng 1979; 39:101.
[38] Argon AS, Shi LT: Philos Mag A 1982; 46:275.
[39] Lund AC, Schuh CA: Acta Mater 2003; 51:5399.
[40] Johnson WL, Samwer K: Phys Rev Lett 2005; 95:195501.
[41] Zink M, Samwer K, Johnson WL, Mayr SG: Phys Rev B 2006; 73:172203.
[42] Yang B, Liu CT, Nieh TG: Appl Phys Lett 2006; 88:221911.
[43] Lewandowski JJ, Greer AL: Nature Mater 2006; 5:15.
[44] Ott RT, Fan C, Li J, Hufnagel TC: J Non-Cryst Solids 2003; 317:158.
[45] Hays CC, Kim CP, Johnson WL: Phys Rev Lett 2000; 84:2901.
[46] Lee ML, Li Y, Schuh CA: Acta Mater 2004; 52:4121.
[47] Ott RT, Sansoz F, Molinari JF, Almer J, Ramesh KT, Hufnagel TC: Acta Mater 2005; 53:1883.
[48] Concustell A, Alcalá G, Mato S, Woodcock T, Gebert A, Eckert J, Baró MD: Intermetallics 2005; 13:1214.
[49] Muñoz-Morris MA, Suriñach S, Gich M, Baró MD, Morris DG: Acta Mater 2003; 51:1067.
[50] Allen DR, Foley JC, Perepezko JH: Acta Mater 1998; 46:431.
[51] Gangopadhyay AK, Croat TK, Kelton KF: Acta Mater 2000; 48:4035.
[52] Conner RD, Dandliker RB, Johnson WL: Acta Mater 1998; 46:6089.
[53] Li H, Li K, Subhash G, Kecskes LJ, Dowding RJ: Mater Sci Eng A 2006; 429:115.
[54] Lee MH, Sordelet DJ: Appl Phys Lett 2006; 88:261902.
[55] Jang JSC, Chang LJ, Young JH, Huang JC, Tsao CYA: Intermetallics 2006; 14:945.
[56] Xing LQ, Li Y, Ramesh KT, Li J, Hufnagel TC: Phys Rev B 2001; 64:180201.
[57] Das J, Tang MB, Kim KB, Theissmann R, Baier F, Wang WH, Eckert J: Phys Rev Lett 2005; 94:205501.
[58] Concustell A, Mattern N, Wendrock H, Kuehn U, Gebert A, Eckert J, Greer AL, Sort J, Baró MD: Scripta Mater 2007; 56:85.
[59] Gleiter H: Acta Mater 2000; 48:1.
[60] Lu K, in: Processing and Properties of Nanocrystalline Materials (TMS, Warrendale, PA, 1996, Edited by: Suryanarayana C et al).
[61] Suryanarayana C, Koch CC: Hyper Inter 2000; 130:2.
[62] He G, Eckert J, Löser W, Schultz L: Nat Mater 2003; 2:3.
[63] Weismüller J, Löfler J, Kebler M: Nanostruct Mater 1995; 6:105.
[64] Gleiter H: Prog Mater Sci 1989; 33:223.
[65] Siegel RW, in: Materials Interfaces: Atomic Level Structure and Properties (Chapman & Hall, London, UK, 1992, Edited by: Wolf D, Yip S).
[66] Meyers MA, Mishra A, Benson DJ: Prog Mater Sci 2006; 51:427.
[67] Chokshi AH, Rosen A, Karch J, Gleiter H: Scripta Mater 1989; 23:1679.
[68] Zhang X, Wang H, Scattergood RO, Narayan J, Koch CC: Acta Mater 2002; 50:3527.
[69] Zhu YT, Liao X: Nature Mater 2004; 4:351.
[70] Yamakov V, Wolf D, Phillpot SR, Gleiter H: Acta Mater 2002; 50:5005.
[71] Chen M, Ma E, Hemker KJ, Sheng H, Wang Y, Cheng X: Science 2003; 300:1275.

[72] Conrad H: Met Mater Trans 2004; 35A:2541.
[73] Fu HH, Benson DJ, Meyers MA: Acta Mater 2004; 52:4413.
[74] Zhu YT, et al: Appl Phys Lett 2004; 85:5049.

2. Experimental Methods

This chapter will outline the main experimental techniques that have been used in this work. In section 2.1 the processing methods of the studied alloys are covered, i.e. arc furnace, melt spinning, Cu-mould casting and high pressure torsion. Arc furnace has been used to obtain master alloys of the different studied compositions. The metallic glasses studied in this work have been processed by melt-spinning and Cu-mould casting, while the samples subjected to severe plastic deformation have been processed by high pressure torsion. Afterwards, in section 2.2, the characterization techniques used (thermal, microstructural and mechanical) are described. The basic operation of differential thermal analysis and differential scanning calorimetry is explained and the Kissinger method used to extract the activation energy of a process is deduced. The fundamentals of electron microscopy and x-ray diffraction are presented. Finally, the compression tests, the viscosity measurements and the methods of measurement of hardness and elastic modulus by nanoindentation are also explained.

2.1. Processing Methods

2.1.1. Arc-melting

An electric arc furnace is a system that heats charged material by means of an electric arc. Arc furnaces range in size from large units of approximately one ton capacity used in foundries for producing cast iron products, down to about 50 grams in research laboratories.

In the 19th century, a number of men had employed an electric arc to melt iron. Sir Humphry Davy conducted an experimental demonstration in 1810; welding was investigated by Pepys in 1815. Pinchon attempted to create an electrothermic furnace in 1853 and, in 1878-79, Sir William Siemens took out patents for electric furnaces of the arc type.

2.1.1.1. Description of the technique

An electric arc furnace used for alloy making consists of a refractory-lined vessel, usually water-cooled in larger sizes, covered with a retractable roof, and through which one or more tungsten electrodes enter the furnace. Electrodes may be pyramidal allowing the formation of an electric arc between the material and the electrode. The material is heated both by current passing through the charge and by the radiant energy evolved by the arc.

The tungsten electrodes are automatically raised and lowered by a positioning system, which may use either electric winch hoists or hydraulic cylinders. The regulating system

maintains an approximately constant current and power input during the melting of the alloy, even though scrap may move under the electrodes while it melts.

The arc furnace described above can be used extensively for the preparation of different alloys. This includes systems with high-melting point elements like tungsten, rhenium, and molybdenum. In order to make an alloy melt as homogeneously as possible, generally the samples are remelted numerous times. If the alloys are brittle then the standard procedure is to crush the melt with mortar and pestle and, then remelt it. If the alloy samples are not brittle they can be machined into chips which then can be remelted. However, quite homogenous melt can be made by simply distributing the constituents in a random manner in the mould and repeating the arc melting several times with successive inversions of the sample [1].

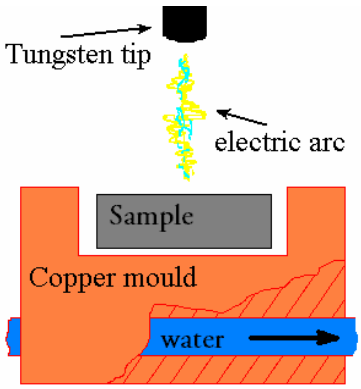

Figure 2.1. Scheme of an arc furnace.

Different ingots with nominal composition of $Cu_{60}Zr_xTi_{40-x}$ (x = 15, 20, 22, 25, 30), $Ni_{59.5}Nb_{40.5}$, $Ni_{57.5}Y_{42.5}$, $Ni_{58.5}Nb_{20.25}Y_{21.25}$, and $Ti_{60}Cu_{14}Ni_{12}Sn_6Nb_{10}$ (at%) were produced by arc melting of pure elements on a water-cooled copper mould under a high purity argon atmosphere. The ingots were remelted at least three times to obtain a macroscopic homogeneous distribution.

2.1.2. Introduction to metallic glass formation

An amorphous material represents the ultimate metastable state of solid matter and may be obtained in a number of different ways, including solidification from the liquid or vapour state, deposition from a chemical solution or an electrolyte.

The vitrification of a melt requires a high cooling rate in order to avoid the crystallization and therefore the atoms are frozen in their liquid configuration [2]. Thus, a glass may be implicitly defined as a material that contains an insignificant quantity of crystals. A time-temperature-transformation (TTT) curve may be calculated using the JMAK theory (section 1.1.6.1), which relates a crystallized volume fraction, *x*, to the rates of nucleation (*I*)

and growth (u). Under isothermal conditions, when I and u are constant, and for x small enough, the following expression is obtained,

$$x \approx \frac{\pi}{3} I u^3 t^4 \qquad \text{eq. 2.1}$$

The TTT curve can be constructed using eq. 2.1 together with measured or calculated values for I and u, as in Fig. 2.2. From Fig. 2.2, the existence of a critical cooling rate is observed in order to obtain a really small volume fraction of crystallites during cooling and hence, a glass can be formed.

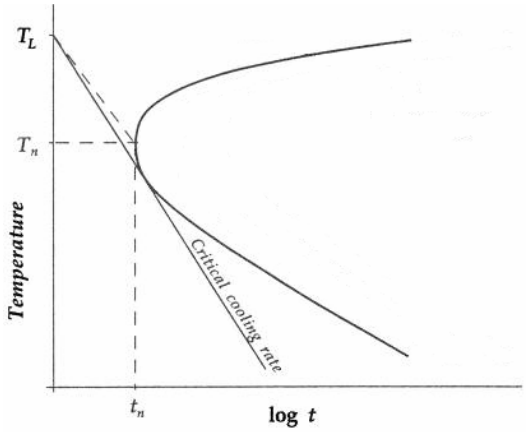

Figure 2.2. Time-temperature-transformation (TTT) diagram showing the conditions for metallic glass formation [3].

From Fig. 2.2 and eq. 2.1, there is no clear-cut separation between glass-formers and non-glass-formers; instead, the glass-forming tendency of a liquid may be quantified in terms of the critical cooling rate. Therefore, glass formation occurs easily in some familiar classes of non-metallic materials such as silicates and organic polymers. In these materials, the nature of the bonding imposes severe limits on the rearrangement rate of the atoms or molecules, which are necessary for maintaining the thermodynamic equilibrium during cooling. Consequently, the melt solidifies to a glass even at low cooling rates, often less than 10^{-2} K/s. In contrast, metallic melts have non-directional bonding, and hence the crystallization occurs very rapidly, even at high undercooling states below their equilibrium solidification temperature. For these reasons, high cooling rates, greater than 10^5 K/s, are necessary to obtain some amorphous materials, although some metallic alloys are able to form a metallic glass at cooling rates in the order of 10^2-10^3 K/s.

2.1.3. Melt-spinning processing

The melt spinning process derives its name from the fact that it involves the extrusion of molten metal to produce fine fibbers or ribbons. The melt can be broadly solidified in flight or against a chill depending on the method used.

In this work, the metallic glass ribbons have been obtained by chill-block melt-spinning. This process involves directing a molten metal jet onto a cold and rotating wheel where the jet is reshaped and solidified. The jet on impingement with the disk forms a melt puddle, as the solidification begins, the ribbon is expelled from the surface of the wheel, as schematically illustrated in Fig. 2.3.

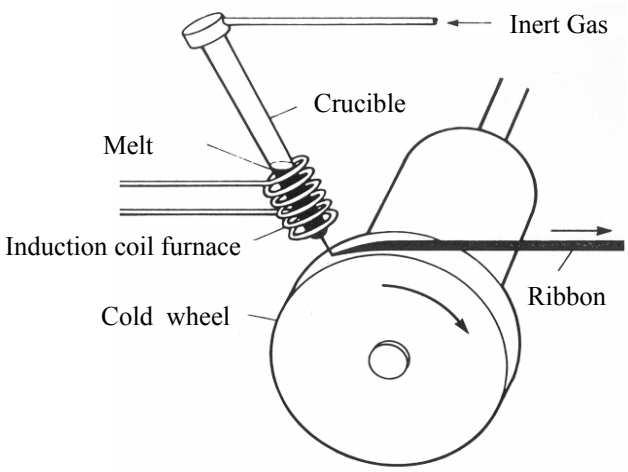

Figure 2.3. Schematic illustration of a chill-block melt-spinning.

The fundamental principle to obtain an amorphous metal by chill-block melt-spinning is based on the heat transfer from the melt to the rotating wheel. The ribbon of thickness X at an initial temperature (T_i) is in contact with a heat conducting material (the wheel) at a temperature T_S, therefore the process may be describe by the Fourier law,

$$\frac{dQ}{dt} = -kA\frac{dT}{dx} \qquad \text{eq. 2.2}$$

where x is the coordinate perpendicular to the wheel surface, k is the thermal conductivity of the absorbing heat media (the wheel in our case), and A is the contact surface. From eq. 2.2, the cooling rate decreases with the ribbon thickness, with high contact area and high thermal conductivity of absorbing heat media. But intrinsic parameters of the melt such as heat capacity, density and thermal conductivity also affect the cooling rate. Therefore, the cooling rate will be higher for low heat capacities and higher thermal conductivity of the melt.

A chill-block melt-spinning consists of different parts: induction furnace, crucible and injection system, the wheel and pressure/atmosphere control system, as shown in Fig. 2.3. Optimizing the parameters for casting is an essential work to obtain metallic glassy ribbons and control the quality of the final product.

Crucibles: The main materials used for crucibles are alumina, quartz and graphite. Selection of crucible material is based on chemical compatibility with the melt, temperature capability, thermal shock resistance, low thermal conductivity and low porosity. When melting is complete, the alloy is ejected by applying overpressure in the crucible.

Wheels: Primarily, the aim is to select a wheel material which will extract heat from the ribbon as quickly as possible, i.e. with high thermal conductivity, while allowing the puddle to wet the wheel and form the ribbon. Wheel surface texture and cleanliness influence both product quality and form. The homogeneity of the puddle depends on the roughness or imperfections in the surface wheel. If the flow is not laminar and stable the quality of the obtained ribbon may be affected.

The hardness of the substrate is found to be one of the factors that influence the wear resistance because a roll made of age-hardened Cu-2%Be alloy showed comparatively little wear even after much longer service than pure copper.

Distance between crucible and wheel: The distance between the crucible and the wheel has to ensure a laminar and stable flow. Longer distances than the optimum one may provoke turbulences in the puddle, while too short distances may cause the contact between the puddle and the crucible.

Chamber atmosphere: Spinning can be carried out in vacuum, air, inert atmosphere, or reactive gas depending upon the chemical and physical properties of the charge. Alloys susceptible to oxidation can be cast in vacuum or inert gas.

Ejection Pressure: Ejection of the melt from the crucible is accomplished by gas pressurization. Although an inert gas is generally used, any gas compatible with the melt can be used. Ejection pressure depends upon the desired melt delivery rate.

Wheel speed: Increasing the wheel speed leads to the formation of thinner ribbons and therefore, to higher cooling rates. The time of contact of the solidifying material on the chill block is of decisive importance in the fabrication of amorphous metallic ribbons. If the ribbon detaches from the disk too soon, crystallization and phase decomposition may occur.

2.1.3.1. Experimental procedure

The casting of the Cu-base ribbons studied in this work has been done in the *SZFKI* (Solid State Physics Research Institute) in Budapest, while the Ni-base ribbons have been cast in the *IFW Dresden* by Prof. Mattern.

The $Cu_{60}Zr_xTi_{40-x}$ (x = 15, 20, 22, 25, 30) amorphous ribbons were obtained by single-roller melt spinning technique. The parameters used for the casting are the followings:

- Cu-2%Be wheel of 35 cm in diameter.
- Wheel speed: 39 m/s.
- Crucible material: graphite.
- Working atmosphere: inert (Ar).
- Injection temperature: 1300ºC.
- Ejection pressure: 1.5 bar.

2.1.4. Copper mould casting

The method used in this work to produce amorphous bulk alloys is the copper mould casting (CMC). A part of the master alloy is introduced in a graphite crucible where it will be melted by the action of an induction furnace, similar to the case of melt spinning. Then, the melt is injected into a copper mould (see Fig. 2.4) by applying an over-pressure in the crucible. The cooling rate is generally 10^2-10^3 K/s and therefore only some metallic alloys, with high glass forming ability, may be cast by this method obtaining them with an amorphous structure.

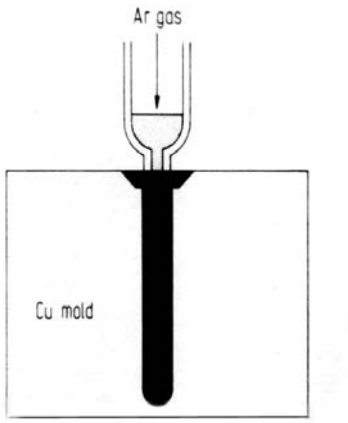

Figure 2.4. Schematic view of the Cu mould casting process.

Similarly to the chill-block melt-spinning, the optimization of the casting parameters is an essential work to obtain a metallic glass and to control the quality of the final product. Crucibles and chamber atmosphere depend on the reactivity of the alloy with them, similar to the melt-spinning case. The main parameters controlling the cooling rate are the temperature and pressure of ejection. A high temperature of ejection may lead to a low cooling rate due to its difference with the glass transition temperature. A low temperature of ejection results in a high viscosity of the melt and therefore, the alloy may solidify before filling the mould.

The casting of the Cu-base cylinders studied in this work has been done in the *IFW Dresden*. The initial ingots of composition $Cu_{60}Zr_xTi_{40-x}$ (x = 15, 20, 22, 25, 30) obtained by arc-melting were remelted in a graphite crucible an injected in a copper mould. Cylinders of 50 mm in length and 3 mm diameter were obtained using the following casting conditions:

- Crucible material: graphite.
- Working atmosphere: inert (Ar).
- Injection temperature: between 1250 - 1300ºC.
- Ejection pressure: 1.5 bar.

2.1.5. Severe plastic deformation by torsion straining under high pressure

2.1.5.1. High-pressure torsion (HPT) method

High pressure torsion (HPT) method is used for fabrication of disk type sample, see Fig. 2.5 a). An ingot or master alloy is held between anvils (plunger and support) and strained in torsion under an applied pressure (P) of several GPa at a given temperature. Torsion strain is imposed through rotation of the lower support and surface frictional forces deform the disk by shear. Due to the specific geometric shape of the sample, the main volume of the material is strained in conditions of quasihydrostatic compression under the applied pressure. Figure 2.5 b) depicts the variables used in estimating the strain imposed in HPT method where, for an infinitely small rotation, $d\theta$, and a displacement, dl, it follows that $dl = r d\theta$, where r is the radius of the disk and the incremental shear strain, $d\gamma$, is given by $d\gamma = dl/h = r d\theta/h$, where h is the disk thickness [4].

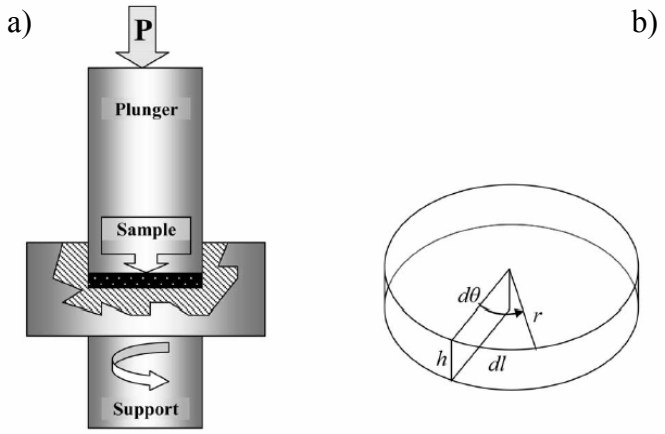

Figure 2.5. (a) Schematic illustration of HPT processing and (b) parameters used in estimating the total strain in HPT [5].

Different relationships have been developed to account for the imposed strain in HPT, as discussed in [5]. However, based on the uncertainties in calculating strain and following an earlier suggestion [6], the strain may be specified in terms of the total number of whole revolutions applied to the disk.

Pieces from the ingots of $Ti_{60}Cu_{14}Ni_{12}Sn_6Nb_{10}$ (at%) alloys were processed by HPT, subjecting them to 5 whole-turn torsion under an applied pressure of 4 GPa, using a modified *Bridgeman* anvil type device [4] located at the "*Institute for Physics of Advanced Materials*" in Ufa. Several disks, of approximately 10 mm in diameter and 0.3 mm in thickness were obtained.

2.2. Characterization techniques

Differential Scanning Calorimetry (DSC) has been used to study the thermal stability and the crystallization kinetics of several metallic glasses. The different processing routes and posterior heat treatments induce several morphological and structural changes in the studied materials, which have been analyzed by means of scanning electron microscopy (SEM) and X-ray diffraction (XRD), respectively. The structural changes occurring in metallic glasses subjected to different heat treatments have also been studied by transmission electron microscopy (TEM). Nanoindentation has been used to determine the mechanical properties of the studied metallic glasses and nanocomposite materials.

2.2.1. Differential Thermal Analysis (DTA) and Differential Scanning Calorimetry (DSC)

2.2.1.1 Basic principles for DTA and DSC

Following the temperature of a substance as a function of time, i.e., thermal analysis, has been a scientific tool since long age. Le Chatelier, however, added the feature of considering the rate of change of temperature, differential thermal analysis. His very clever experimental method displayed marks at equal increments of time and the spacing between marks corresponded to the change in temperature. Marks were close together during slow rates and further apart during rapid changes.

An improvement of the technique consisted of placing an inert reference material, having a similar heat capacity, along side the specimen of interest and following the difference in temperature between the reference and sample. Unintended fluctuations in the rate of heating and cooling are much less likely to cause a significant disturbance in the signal. Both the sample and reference will react similarly cancelling the potential effect leaving the baseline unperturbated.

The principle and a scheme of a DTA apparatus are illustrated in Fig. 2.6. As the specimen is heated or cooled in a controlled manner, its temperature (T_S) will depart from the normal rate as it undergoes a reaction or transformation. Considering the heating curve, if the event is endothermic then the sample will slow its rate of heating while it is undergoing the particular process. Similarly, if the event is exothermic, then the sample's temperature would increase at a more rapid rate during that period. A change in the thermal conductivity or heat capacity of the sample would give a change in slope during thermal analysis and an offset or step in the baseline of a DTA curve.

The typical DTA apparatus utilizes a pair of matched temperature sensors, generally thermocouples, one of which is in contact with the sample or its container and the other in

contact with the reference material, as shown in Fig. 2.6 b). The output of the differential thermocouple is amplified and fed to the recorder or data acquisition system. The ΔT is generally plotted as a function of either the actual sample temperature, reference temperature or time.

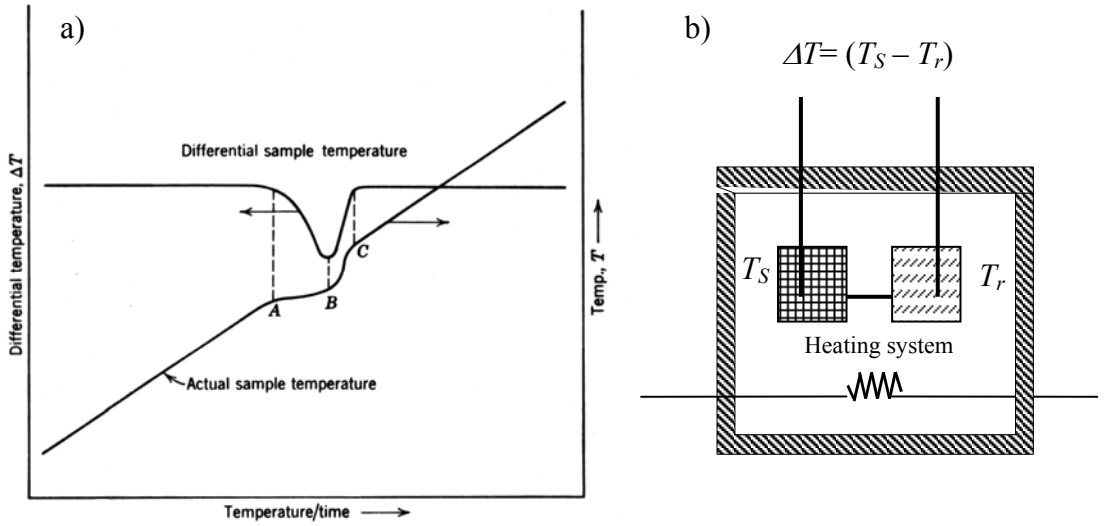

Figure 2.6. a) General principle for an endothermic event. b) Scheme of a DTA apparatus, where T_S and T_r are the sample and the reference temperature respectively [3].

The sample and reference systems are closely matched thermally and arranged within the furnace or oven in a symmetrical fashion so that they are both heated or cooled in identical manner. Under these circumstances the ΔT signal will be essentially zero until the sample undergoes one exothermic or endothermic event.

Ideally the area under the DTA peak should be proportional to the enthalpy of the process that gave rise to the peak. There are many factors, however, which influence the curve and which are not compensated in the traditional simple DTA plot. The changes in thermal transport properties of the system, detector sensitivity, etc. with temperature will generally diminish the response of the DTA with increasing temperature.

The DSC was very cleverly developed to either avoid these difficulties or to quantitatively compensate for their effects. A schematic representation of a power compensating DSC is shown in Fig. 2.7. The inventive concept keeps the value of ΔT equal to zero by placing the temperature sensor, Pt resistance thermometers, into a bridge circuit. Any imbalance is used to drive a heater in the appropriate sample or reference portion of the cell. The power needed to keep the bridge circuit in balance is proportional to the change in heat capacity or enthalpy occurring. The integral of the power over the time of the event gives the energy difference between the sample and the reference, which corresponds to the enthalpy difference of the process. Therefore, if power is supplied to the sample, the process is endothermic, if it is supplied to the reference side, then the process is exothermic.

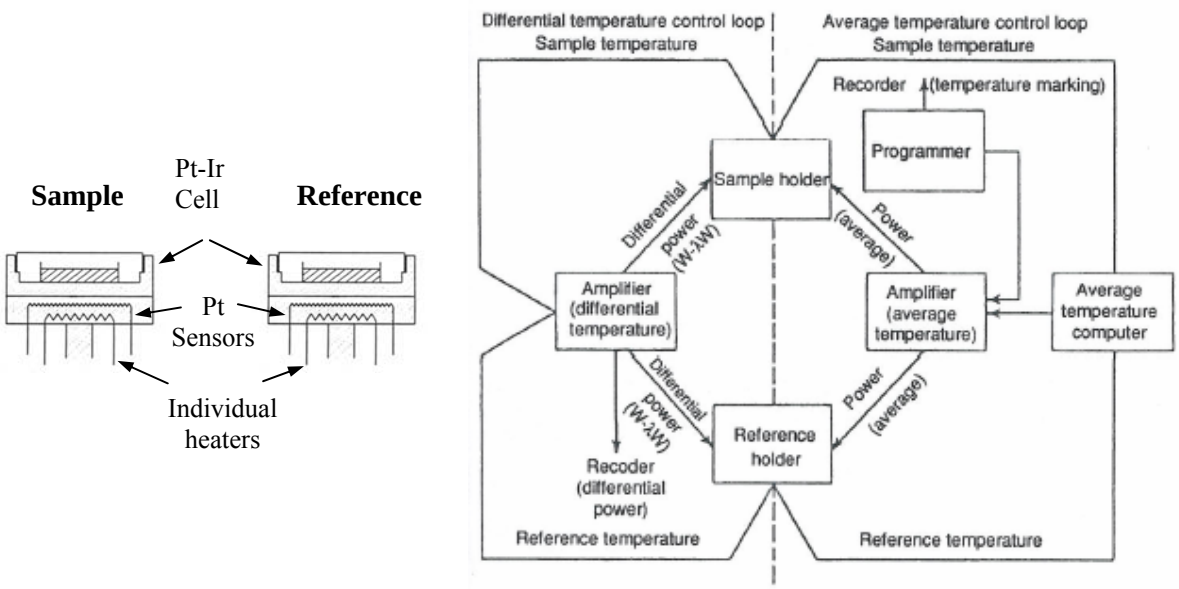

Figure 2.7. Schematic representation of a power compensating DSC instrument and its operation [3].

The transformations experimented by a material display a peak in the DSC signal which represents the power supplied (*dQ/dt*) to the sample to keep the same temperature for the sample and the reference. Figure 2.8 shows a schematic representation of a DSC curve. The interpretation of this curve, following the IUPAC (International Union of Pure and Applied Chemistry), helps us to find the transformation temperature of a process, to study its kinetics and measure its enthalpy [7].

The IUPAC has given precise definitions of the terminology used for the interpretation of the DSC curves.

- *Baseline*: part or parts of the DSC curve in which *dQ/dt* is nearly zero (lines AB and DE in Fig. 2.8)
- *Peak*: part of the curve which initially goes off and later goes back the baseline (line BCE in Fig. 2.8). Those transformations with $dQ/dt < 0$ are exothermic.
- *Peak width*: interval of temperature or time in which the DSC curve goes off the baseline (line B'D' in Fig. 2.8).
- *Peak height*: distance, perpendicular to the temperature o time axis, between the interpolation of the baseline and the peak vertex (line CF in Fig. 2.8).
- *Peak area*: closed area by the peak and the interpolation of the baseline (area limited by the lines BCDB in Fig. 2.8).
- *Initial temperature of the transformation*: temperature corresponding to the intersection point between the tangent at the maximum slope point at the beginning of the peak and the interpolation of the baseline (point G in Fig. 2.8).

- *Final temperature of the transformation*: temperature corresponding to the intersection point between the tangent at the maximum slop point at the end of the peak and the interpolation of the baseline (point H in Fig. 2.8)

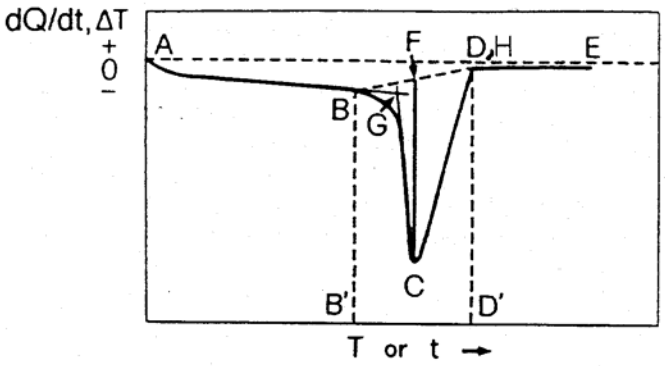

Figure 2.8. Schematic representation of a DSC curves and its interpretation following the IUPAC rules [7].

2.2.1.2. Applications of the DSC technique in the present study

Linear heating and isothermal treatments have been performed by DSC. Linear heating have allowed us to study the thermal stability of the different metallic glasses and to determine the activation energy of the crystallization processes. The crystallization kinetics of a metallic glass has been studied by isothermal treatments.

The calorimetric curves obtained by DSC may be related to kinetic variables. In agreement with the Borchard approximation [8,9], the heat flux generated in the transformation (the DSC signal) is directly proportional to the transformation rate, *dx/dt*:

$$\frac{dx}{dt} = A\frac{dQ}{dt} \qquad \text{eq. 2.3}$$

where *A*, is a proportionality constant and *dQ/dt* is the amount of energy absorbed or emitted by a sample. Integrating the area under the transformation peak to a specific time or temperature, T_f or t_f, the transformed fraction, $x(T_f,t_f)$ is:

$$x = A\int_{T_0,t_0}^{T_f,t_f}\frac{dQ}{dt}dt' \qquad \text{eq. 2.4}$$

imposing $x = 1/\Delta H_{total}$, where ΔH_{total} is the enthalpy of transformation of one reference material, the *A* constant may be determined.

Since the DSC signal corresponds to the *dQ/dt* absorbed or emitted by the sample during the transformation as a function of temperature (in linear heating) or time (in isothermal

treatments), the peak area, S, of the DSC curve is proportional to the transformation enthalpy, $\Delta H(t_f)$,

$$S = \int_{T_0,t_0}^{T_f,t_f} \frac{dQ}{dt} dT = \int_{T_0,t_0}^{T_f,t_f} \frac{dQ}{dt}\frac{dT}{dt} dt = \beta \int_{T_0,t_0}^{T_f,t_f} \frac{dQ}{dt} dt' = \beta C \Delta H(t_f) \text{ (for a linear heating)} \quad \text{eq. 2.5}$$

$$S = \int_{T_0,t_0}^{T_f,t_f} \frac{dQ}{dt} dt' = C\Delta H(t_f) \text{ (for an isothermal treatment)} \quad \text{eq. 2.6}$$

where β is the heating rate. Supposing that the crystallization enthalpy is constant during the process, the transformed or crystallized fraction, x, may be calculated dividing ΔH over $\Delta H(t_f)$. Figure 2.9 shows a DSC curves corresponding to a transformation process, the transformed fraction may be calculated for an isothermal treatment by

$$x = \frac{\Delta H(t)}{\Delta H(t_f)} = \frac{\int_{t_0}^{t} \frac{dQ}{dt} dt}{\int_{t_0}^{t_f} \frac{dQ}{dt} dt} = \frac{S_t}{S} \quad \text{eq. 2.7}$$

where S_t is the area at a given time t during the treatment and S the total area closed under the peak. From eq. 2.7, the transformation rate is given by

$$\frac{dx}{dt} = \frac{d}{dt}\left(\frac{\int_{t_0}^{t} \frac{dQ}{dt} dt}{S} \right) = \frac{1}{S}\frac{dQ}{dt} = \frac{h}{S}. \quad \text{eq. 2.8}$$

Equation 2.8 is the same for a linear heating, since the heating rate, β, is cancelled. Therefore, the transformed fraction and the transformation rate can be evaluated at any time of the transformation process.

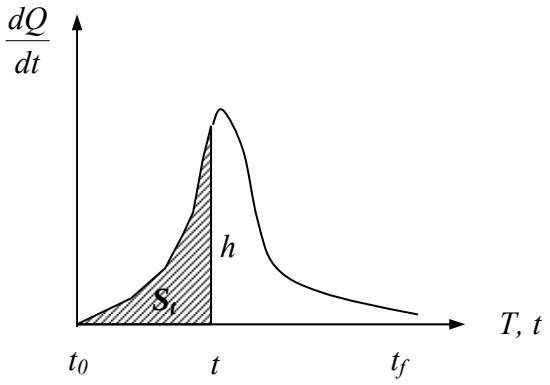

Figure 2.9. Schematic representation of a DSC curve corresponding to a transformation process.

2.2.1.3. Kissinger Method

The most common application of DSC technique in the study of the crystallization kinetics is the determination of the activation energy by the Kissinger method [10]. This method starts from the fundamental kinetic equation:

$$\frac{dx}{dt} = K(T) f(x) \qquad \text{eq. 2.9}$$

where *dx/dt* is the transformation rate of the transformed fraction, *K(T)* is the constant rate and *f(x)* is a characteristic function of the studied process. Considering the constant rate, *K(T)* as a function of temperature of the Arrhenius type hence results that:

$$K(T) = K_0 \exp\left(\frac{-E_a}{RT}\right) \qquad \text{eq 2.10}$$

where K_0 is a pre-exponential factor, E_a is the activation energy of the process (related with the potential barrier of the process, supposing that the studied temperature range is constant), T is the temperature and R is the universal gas constant.

On the assumption that the transformation rate is maximum $(d^2x/dt^2=0)$ in the maximum of the peak and the transformed fraction in this point, x_p, is the same for all heating rates, the eq. 2.10 is brought in differential form:

$$\left[\frac{d^2x}{dt^2}\right]_{x=x_p} = K(T)\left[\frac{df(x)}{dt}\right]_{x=x_p} + \left[\frac{dK(T)}{dt}\right]_{x=x_p} f(x_p) = 0 \qquad \text{eq. 2.11}$$

evaluating the equation terms, it is seen:

$$\frac{df(x)}{dt} = \frac{df(x)}{dx}\frac{dx}{dt} = f'(x)K(T)f(x) \qquad \text{eq. 2.12}$$

adopting the Arrhenius expression for *K(T)* results that:

$$\frac{dK(T)}{dt} = \frac{dK(T)}{dT}\frac{dT}{dt} = \frac{E_a}{RT^2}K(T)\frac{dT}{dt} = \frac{E_a}{RT^2}K_0\beta\exp\left(-\frac{E_a}{RT}\right) \qquad \text{eq. 2.13}$$

Finally, substituting these expressions in eq. 2.11, one obtains:

$$\left[\frac{d^2x}{dt^2}\right]_{x=x_p} = K_0 f'(x_p)\exp\left(-\frac{E_a}{RT}\right) + \frac{E_a}{RT^2}\beta \qquad \text{eq. 2.14}$$

from where the following relation it is reached:

$$\ln\left(\frac{\beta}{T_p^{\,2}}\right) = -\frac{E_a}{RT_p} + \ln\left(\frac{RK_0}{E_a}\left(-f'(x_p)\right)\right) \qquad \text{eq. 2.15}$$

The $ln(f'(x_p)) \cong 1$ and is much lower than E_a/RT for the reactions which take place in solid state, so the eq. 2.15 will be written in the approximate form:

$$\ln\left(\frac{\beta}{T_p^{\,2}}\right) \cong -\frac{E_a}{RT_p} + \ln\left(\frac{RK_0}{E_a}\right) \qquad \text{eq. 2.16}$$

The Kissinger method consists of plotting $ln(\beta/T_p^2)$ versus $1/T_p$ for different heating rates. The slope of the linear regression of the data gives, $-E_a/RT$, from where it is possible to calculate the activation energy.

2.2.1.4. Experimental method and working conditions

DSC experiments have been performed in the different metallic glasses studied. A *DSC-7 (Perkin Elmer)* has been used for the calorimetry studies. For linear heating treatments, the mass of sample treated is 8-12 mg for the ribbons and 25 mg for the bulk samples. For the isothermal treatments 35-50 mg has been used for ribbons and bulk samples. The samples have been placed in graphite crucibles for any kind of treatments, avoiding any reaction between the sample and the crucible. In the reference cell, similar graphite crucibles have been used.

A heating rate of 1.67 K/s has been used in isothermal treatments to raise the temperature at the desired one. Once the heat treatment is finished, a linear heating is performed in order to ensure the complete crystallization of the sample. Furthermore, this linear heating allows calculating the transformed fraction during the isothermal treatment. A subsequent isothermal treatment of the crystallized sample was used as baseline for the first isothermal treatment, while a final linear heating was used as baseline for the first linear heating.

2.2.2. Scanning Electron Microscopy

2.2.2.1. Origins and fundamentals of the technique

In 1835 Knoll demonstrated, theoretically, that it was possible to build up a scanning electron microscope (SEM) [11]. In 1938, Von Ardenne constructed the first prototype [12,13]. Scanning electron microscopes became elaborated at an industrial scale in 1965, by the *Cambridge Instruments* company. Since then, they have become an essential tool in many fields of scientific research, such as biology or materials science [14-16].

The main characteristic of electron microscopes, compared to conventional optical microscopes, is that they use electrons instead of light and electromagnetic lenses instead of glass lenses. Under certain assumptions, electrons can be considered as waves, with

wavelengths much smaller than visible light. This allows the observation of very small structures that would remain unobservable using optical microscopes, due to diffraction effects.

Basically, it is possible to distinguish between: (i) transmission electron microscopy (TEM), where one can directly observe on a fluorescent screen the image obtained by electrons that go through a thinned sample and (ii) scanning electron microscopy (SEM), where the electron beam scans over the surface of the sample, inducing electronic transitions and reemission of new electrons that can be used to form the image of the scanned surface.

2.2.2.2. Interaction between the electron beam and the sample

When an electron beam arrives at the surface of a sample, some electrons can penetrate into it. The depth of this penetration directly depends on the atomic number of the constituents of the specimen. The electrons lose their kinetic energy as they go deeper into the sample. In the zone of penetration, a certain number of interactions between the electrons of the beam and the atoms of the sample take place. And, as a consequence, in this zone, several kinds of signals are emitted (see Fig. 2.10):

- Auger electrons.
- Secondary electrons.
- Backscattered electrons.
- X-rays.
- Transmitted electrons.

Auger Electrons: This type of electrons are emitted when an electron of one of the atoms of the specimen, belonging to an external electronic shell, is transferred to an inner shell due to the interaction with the electrons of the incident beam. These electrons have typically low energy values and, therefore, they can only escape the sample from its surface (from a depth range between 0.5 and 2 nm), thus not giving information about more internal parts of the sample. Nevertheless, the energy of this type of electrons is characteristic of the atom that emits them. Thus, these electrons give compositional information of the specimen.

Secondary electrons: These electrons originate from the impacts between high energetic incident electrons and the atoms of the specimen. If the energy of the incident electrons is large enough, the electrons of the atoms in the sample may have enough energy to be expelled out. These are the so-called secondary electrons, which have energies in the range of 0-50 eV. The secondary electrons give information about the density of the sample and the surface topography. However, all the information obtained from secondary electrons is restricted to a penetration depth of 10 nm.

Backscattered electrons: These electrons are originated when the electrons of the incident beam hit the sample but are not able to penetrate it and are consequently reflected back. Therefore their energy depends very much on the energy of the primary incident beam. The information they give also depends on the atomic number of the elements on the surface and also on its topography. Hence, for example the brightness of the image will depend on the atomic number of the specimen since for higher atomic numbers a larger number of backscattered electrons will be obtained.

X-rays: Energy Dispersive X-ray analyses (EDX): When an incident electron hits one atom of the sample inducing the emission of another electron, the corresponding "hole" is immediately occupied by a third electron initially located in a more external electronic shell. As a consequence, some energy in the frequency range of x-rays, is emitted. The wavelengths of the emitted x-rays are characteristic of the atoms that compose the sample. Thus, the resulting spectrum is often used to make compositional analyses of the material. This process is usually denoted as *energy dispersive x-ray analysis* (EDX). If some regions of the sample are scanned selecting the part of the x-ray spectra corresponding to one of the elements in the sample, it is possible to obtain the distribution of this element at the surface. This technique is commonly known as *x-ray mapping*. Therefore, regions with higher densities of this element will appear as bright in the image, while lack of this element will result in a dark area.

Transmitted electrons: When the penetration depth of the electronic incident beam is larger than the sample thickness, some electrons are able to go through it, i.e. they are transmitted. These electrons can be detected so as to obtain a two-dimensional image of the internal structure of the sample. Although a detector for transmitted electrons can be incorporated to a scanning electron microscope, it is rather uncommon and specific transmission electron microscopes are more frequently used for this purpose.

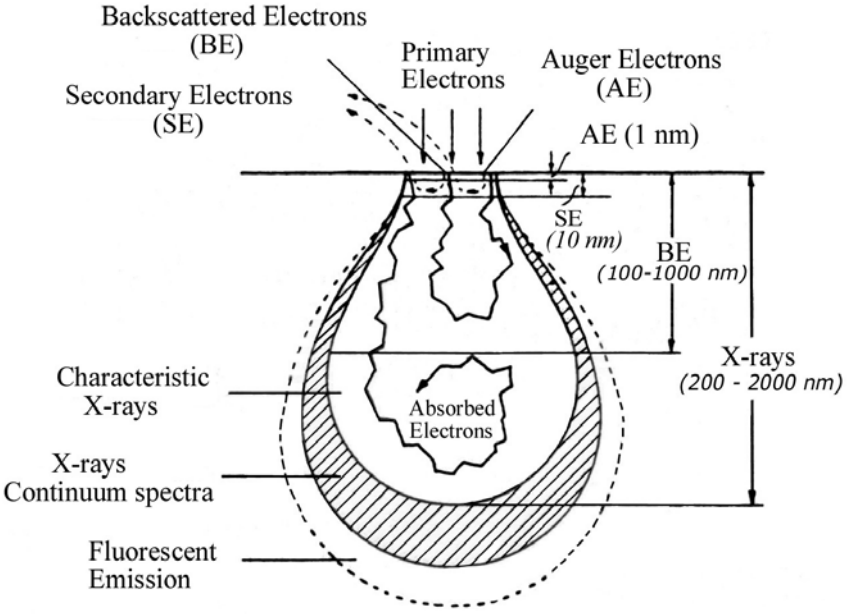

Figure 2.10. Types of electrons and radiation generated inside the sample in a scanning electron microscope.

The main components of a scanning electron microscope are:

- Filament.
- System of electromagnetic lenses and diaphragms.
- Sample chamber.
- Scanning generator system.
- Detectors.

When the *filament* (generally a tungsten wire) is heated it produces a beam of electrons, which are accelerated under application of a voltage between cathode and anode, in the range between 1 and 30 kV. Since electrons have a net charge they can be deviated by applying electric and magnetic fields and, therefore, the beam diameter can be significantly reduced by using a system of *electromagnetic lenses*. Moreover, the beam can be further refined and homogenized by means of several metallic *diaphragms*. Furthermore, the electromagnetic lenses also contribute in accelerating the particles and, thus, they can influence the sharpness of the resultant image.

In the *sample chamber* one can find: the holder, with mechanical mechanisms to move the sample along the three spatial directions and, also, several detectors of the different types of radiation emerging from the sample (x-rays, secondary electrons, backscattered electrons, etc.).

In order to systematically scan the sample, there are two *electromagnetic spirals*, located among the electromagnetic lenses that produce oscillating magnetic fields, along the X-Y directions. This allows precise control of the scan speed.

2.2.2.3. Experimental method and working conditions

Our observations were carried out using a *JEOL JSM-6300* microscope and a *Gemini device (Zeiss)*, located at the *Servei de Microscopia* at the *Universitat Autònoma de Barcelona* and the *IFW Dresden*, respectively. The first microscope was equipped with EDX data acquisition system (model *Link Pentafet*).

The versatility of SEM has allowed observing many different samples. The images of fracture surface after compression tests were obtained by direct observations. The observation of the microstructure of the studied samples was carried out according to the following metallographic procedure:

a) The samples are embedded in a conducting epoxy resin.

b) They are subsequently polished in order to eliminate the surface and to be able to observe their interior. This process is first carried out using silicon carbide sand paper. Afterwards a more refined polishing is performed using diamond paste (of 6, 3 and 1 μm in

particle size) and finally with a colloidal suspension of 0.04 μm SiO_2 particles mixed with H_2O_2 in the ratio 9:1 and etched.

c) Only the Ti-base samples were chemically etched in a dilute aqueous solution of HF and H_2O_2 (100:5:2).

d) some of the studied samples are subsequently metallized with Au (i.e. $Ti_{60}Cu_{14}Ni_{12}Sn_4Nb_{10}$ alloy)

The samples were imaged using both secondary and backscattered electrons. Their composition was analyzed by means of EDX mappings.

2.2.3. Transmission Electron Microscopy

Although this technique has only been used in this work to study the structural changes during heat treatments on the $Cu_{60}Zr_{20}Ti_{20}$ metallic glass, in this section a brief description of the fundamentals of the technique and the experimental procedure will also be given following [17].

In a conventional transmission electron microscope (TEM) a thin specimen is irradiated with an electron beam of uniform current density. The electrons, which are emitted in the electron gun by thermionic emission from tungsten cathodes, have typical energies in the range 60-150 keV. If the penetration depth of the electrons is larger than the thickness of the sample they can go through it. The transmitted electrons are then focused onto a fluorescent screen.

Electrons interact strongly with atoms by elastic and inelastic scattering. The specimens must therefore be very thin, typically of the order of 5 nm – 0.5 μm for 100 keV electrons, depending on the density and elemental composition of the specimen and the resolution desired. Therefore, special preparation procedures are usually required: mechanical thinning, electropolishing, ion milling, etc. In the present work, ion beam thinning has been used to prepare the samples for TEM observation. The TEM apparatus utilized in our study were a *Phillips CM30 SuperTwin*, a *HITACHI 600AB* and a *JEOL 2010F* microscopes.

Furthermore, TEM observations were complemented by selected area electron diffraction (SAED). To perform this experiment, a selected part of the sample is illuminated with electrons, which similar to x-ray diffraction (XRD), are diffracted as they go through the sample. The cone of diffracted electrons, which has an amplitude of a few mrad, goes then through a system of electromagnetic lenses and is finally focused onto the screen, giving an image consisting of a combination of spots (for single crystals) and rings (for polycrystals). The diameter of the area selected in our case cannot be decreased below 1 μm owing to the spherical aberration of the objective lens.

If the area illuminated by the electron beam includes a large number of randomly oriented crystallites, then a *powder* pattern is generated. In this case, a family of rings is

displayed in the fluorescent screen. The radius R of a specific ring is related to the d-spacing of the reflection and the wavelength of the electron beam, λ, by the following relationship:

$$d = \frac{\lambda L}{R} \qquad \text{eq. 2.17}$$

where L is the effective camera length of the electron microscope when used as a diffraction camera. Therefore, by using eq. 2.17 and measuring the relative diameter of the rings it is possible to determine the Miller indexes corresponding to each ring.

2.2.4. X-ray diffraction

2.2.4.1. Origins and fundamentals of the technique

The first experimental evidence concerning x-ray diffraction was given by Max von Laue who in 1912 demonstrated that x-rays could have a comparable wavelength to the atomic spacing in crystals and, therefore, they could be diffracted. This was immediately confirmed by Walter Friedrich and Paul Knipping [18].

In 1914 Darwin elaborated a Kinematic Theory of Diffraction, which assumed that x-rays diffracted by each element in the volume of the material were independent of x-rays diffracted by the other elements [19]. Once diffracted, the beam could not be diffracted again by other elements. Two years later Ewald proposed the Dinamical Theory of Diffraction, which took into account the possibility of having more than one reflection inside the material before the beam emerged from it [20].

If one assumes that the incident x-ray beam is perfectly collimated and monochromatic (with a single wavelength λ) and makes an incident angle θ with respect to the reticular planes of the crystal, it can be demonstrated (see appendix I) that when the following condition is fulfilled:

$$n\lambda = 2d\ sin\theta \qquad \text{eq. 2.18}$$

where n is the reflection order and d is the interplanar distance of one family of crystallographic planes, x-rays will be completely in phase and will, therefore, give constructive interferences. This condition is known as *Bragg's law* and it can be used to determine the angular positions of the XRD peaks diffracted by each family of planes [21-23].

The Bragg's law assumes the crystal is ideal (without structural defects) and the incident beam is perfectly monochromatic and collimated. These conditions are never fulfilled completely. Moreover, usually, the materials are found to be composed of several grains, with different orientation and with certain amount of defects. Each of these grains is called a *crystallite*. The size of these crystallites and the microstrains present in them can also be obtained from the XRD spectra, since both effects contribute to the width of the diffraction

peaks [22,23]. The most frequent procedure to evaluate these effects is to consider that the peaks can be fitted using a pseudo-Voigt function (see appendix I), which is a linear combination of a gaussian and a lorentzian (or Cauchy) profile [24,25]. Using this formalism, the crystallite size can be deduced from the Cauchy contribution to the integral width of the diffraction peak, β_{fC}, as follows:

$$d_{hkl} = \frac{\lambda}{\beta_{fC} \cos\theta_B} \qquad \text{eq. 2.19}$$

where θ_B is the angular position of the peak (measured in radians) and λ is the wavelength (measured in Å). The value of d_{hkl} represents the coherent diffraction domain and is measured also in Å. This equation is commonly known as the *Scherrer formula* [26]. Analogously, microstrains can be determined from the Gaussian contribution to the integral peak width, β_{fG}, using the expression:

$$microstrain = < e > = \frac{\beta_{fG}}{4tg\theta_B} \qquad \text{eq. 2.20}$$

where $<e>$ represents the upper limit of microstrains. However, it is more frequent to use the mean square root of microstrains, $<\varepsilon^2>^{1/2}$ (*rms strain*), which is related to $<e>$ in the following way: $<e> = 1.25 <\varepsilon^2>^{1/2}$. Deduction of eq. 2.19 and 2.20 and a detailed description of the methods used in this work to fit the XRD data is presented in appendix I.

When a powder sample, composed of several phases, is analyzed by x-ray diffraction, each phase originates its own diffraction pattern. The relative intensity of the several peaks in the pattern depends on the relative concentration of the different phases. The phase identification can be carried out by comparison with the *Powder Diffraction Files* database [27].

In general, a powder diffractometer is composed of the following parts [22,23]:

- X-ray generator
- Monochromator.
- Entrance *Soller* slits
- Divergence slits
- Sample
- Exit *Soller* slits
- Reception slits
- Detector

a) The x-ray generator is based on the impacts between source electrons and metal atoms, which result in the emission of electrons of the metal, leaving a large number of holes inside the inner electronic shells. These holes become immediately occupied by electrons from more external shells and the excess of energy is liberated as x-ray radiation, whose energy depends on the energy difference between the energy levels of the electrons and, hence, has discrete values.

b) The monochromator is a filter used to make the radiation as monochromatic as possible, eliminating unwanted radiations.

c) The x-ray generator emits radiation in all directions. The entrance *Soller* slits are used to obtain a parallel and collimated beam. This is accomplished by several fine metallic foils, very close to each other that are located parallel to the diffraction circle plane.

d) There are two divergence slits that are located in front of and behind the *Soller* slits. Their role is to allow the emitted x-rays to diverge as little as possible, in an angle that can usually vary between (1/30)º and 4º.

e) The sample in general needs to be flat, so that x-rays can be well focussed on its surface.

f) The exit *Soller* slits have a similar role to the entrance *Soller* slits, i.e. to keep the diffracted beam, to some extent, collimated.

g) The divergence slits are used to make the x-rays diffracted by the sample more convergent. The width of these slits determines the maximum intensity in the detector.

h) There are several types of detectors: gas, Geiger, semiconductors, etc. The detectors are calibrated so as to count the number of photons per second, so that the intensities are relative to each specific equipment.

2.2.4.2. Experimental method and working conditions

XRD experiments were carried out at the *Servei de Difracció* at the *Universitat Autònoma de Barcelona*, using a *Phillips PW3050* diffractometer.

For XRD experiments, the different types of samples were held on a circular silicon or iron holder. While the ribbons were simply cut and fixed onto silicon holders by water, the bulk samples were cut and fixed by plasticine onto iron holders ensuring that the sample surface is at the Bragg plane of the diffractometer.

Some technical specifications are presented here:

Tube:

Anticathode: Cu

Voltage: 40 kV

Current: 50 mA

Radiation: Cu-K_α $\lambda(K_{\alpha 1}) = 1.54060$ Å

$\lambda(K_{\alpha 2}) = 1.54439$ Å

$I(K_{\alpha 2}) / I(K_{\alpha 1}) = 0.500$

Primary beam optics:

Soller slits: 0.04 mm

Divergence at the entrance: ½º

Secondary beam optics:

Soller slits: 0.04 mm

Divergence at the exit: ½º

Monochromator: pyrolitic graphite

The x-ray spectra were obtained in a *step-scan* mode. This means that the sample and the detector rotated in steps instead of in a continuous way. The appropriate step size for each experiment was selected in order to have at least 10 experimental points above the half height width. Therefore, depending on the peak widths, 2θ steps of 0.04º or 0.08º were chosen. Moreover, the time for step was selected to be relatively long (10 to 20 s) in order to reduce the statistical error.

The powder diffractometer used in our study was set up in *Bragg-Brentano* geometry (see Fig. 2.11). In this geometry, both the x-ray source and the detector are located in the focalization circle. Since the detector has to follow the diffracted radiation, when the sample rotates at an angular speed θ, the detector has to rotate at 2θ. Thus, if the sample rotates an angle θ the diffracted beam is deviated 2θ with respect to the incident direction. As a consequence, the *Bragg-Brentano* geometry is also known as *"θ - 2θ scan"*.

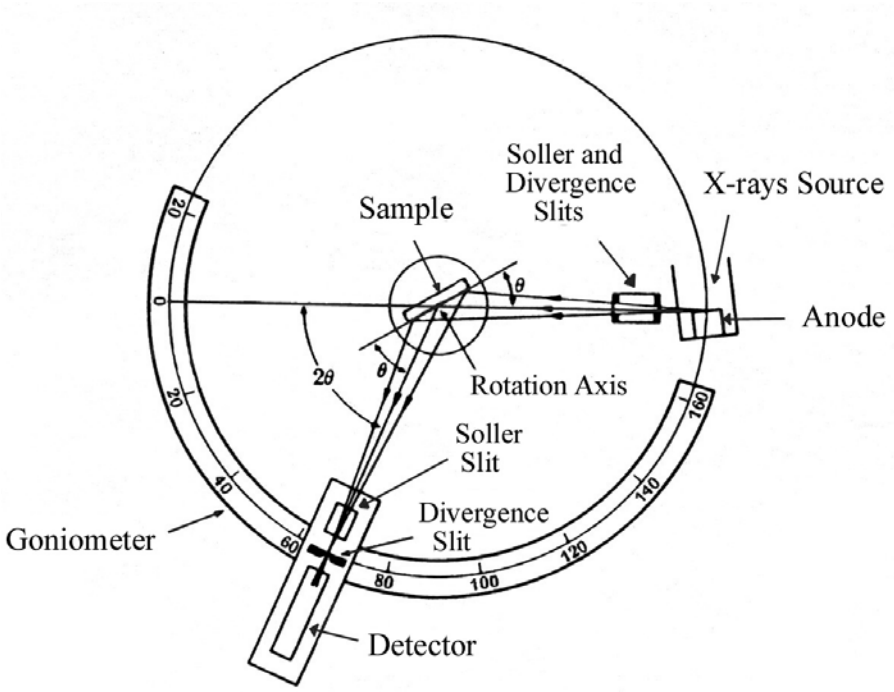

Figure 2.11. Schematic picture of an x-ray diffractometer.

2.2.4.3. Synchrotron radiation

Synchrotron radiation is electromagnetic radiation generated by the acceleration of ultrarelativistic electrons through magnetic fields. This may be achieved artificially by storage rings in a synchrotron. The radiation typically includes infrared, optical, ultraviolet and x-rays.

In synchrotrons, electrons are accelerated to high speeds in several stages to achieve a final energy that is typically in the GeV range. The electrons are stored in an ultrahigh vacuum ring on a closed loop and thus circle the ring a vast number of times. The electrons are forced to travel in a closed loop by strong magnetic fields. The magnets also need to repeatedly recompress the Coulomb-exploding space charge electron bunches. A dramatic effect of relativity is that the radiation pattern is also distorted from the isotropic dipole pattern expected from non-relativistic theory into an extremely forward-pointing cone of radiation. This makes synchrotron radiation sources the brightest known sources of X-rays.

The advantages of using synchrotron radiation for spectroscopy and diffraction have been realized by an ever-growing scientific community. These advantages are due to the following characteristics of the synchrotron radiation:

- High brightness and high intensity, many orders of magnitude more than with X-rays produced in conventional X-ray tubes.
- High brilliance, exceeding other natural and artificial light sources by many orders of magnitude.
- High collimation, i.e. small angular divergence of the beam
- Widely tunable in energy/wavelength by monochromatization.
- High level of polarization (linear or elliptical).
- Pulsed light emission (pulse durations at or below one nanosecond).

In this work, time resolved in-situ X-Ray diffraction studies were performed at the ID11 beam line of the *European Synchrotron Radiation Facilities (ESRF)* using a monochromatic beam of 95 keV (0.1304Ă). The rolled-up ribbons were sealed in a quartz tube under vacuum of 10^{-2} torr and placed in the centre of an induction heating apparatus. The X-ray beam with a size of 200x200 μm^2 passed the sample in transmission mode. The crystallization behaviour during heating of the as-quenched materials was observed by taking 2-dimensional diffraction patterns, using a CCD detector (FRELON) coupled to an image intensifier, with an exposure time of 2 or 3 seconds. The delay between consecutive patterns, due to read-out time of the CCD (2048x2048 pixels) and write-time to hard-disc was 2 seconds. The 2-dimensional patterns were integrated, after dark-current and spatial distortion correction. The sample temperature was constantly monitored (500 ms interval) with an optical pyrometer (IGAQ, 10 LO, IMPAC) with a working range of 623-1573 K and with an uncertainty of ±3 K below 773 K.

2.2.5. Mechanical properties

The mechanical properties of a material are those properties that involve a reaction to an applied load. The mechanical properties of metals determine the range of usefulness of a material and establish the service life that can be expected. Mechanical properties are also used to help classify and identify material. The most common properties considered are strength, ductility, hardness, impact resistance, and fracture toughness.

The mechanical properties of a material are not constants and often change as a function of temperature, rate of loading, and other conditions. For example, temperatures below room temperature generally cause an increase in strength properties of metallic alloys; while ductility, fracture toughness, and elongation usually decrease. Temperatures above room temperature usually cause a decrease in the strength properties of metallic alloys. Ductility may increase or decrease with increasing temperature depending on the same variables.

It should also be noted that there is often significant variability in the values obtained when measuring mechanical properties. Seemingly identical test specimen from the same lot of material will often produce considerable different results. Therefore, multiple tests are commonly conducted to determine mechanical properties and values reported can be an average value or calculated statistical minimum value. Also, a range of values are sometimes reported in order to show variability.

In our work, compression tests have been performed to different metallic glasses. The intrinsic brittleness in tension of metallic glasses makes compression tests a useful tool to evaluate yield stress, ultimate stress and modulus of elasticity of these materials, always regarding that they are obtained in compression.

2.2.5.1. Compression tests

The application of a force to an object is known as loading. Materials can be subjected to many different loading scenarios and a material's performance is dependant on the loading conditions. There are five fundamental loading conditions: tension, compression, bending, shear and torsion. Tension is the type of loading in which the two sections of material on either side of a plane tend to be pulled apart or elongated. Compression is the reverse of tensile loading and involves pressing the material together.

In compression testing the sample is squeezed in a very controlled manner, while the load and the displacement are carefully recorded. Compression tests result in mechanical properties that include the compressive yield stress, compressive ultimate stress, and compressive modulus of elasticity.

The main product of a compression test is a load versus elongation curve which is then converted into a stress versus strain curve. The stress-strain curve relates the applied stress to

the resulting strain and each material has its own unique stress-strain curve. A typical engineering stress-strain curve is shown below. If the true stress, based on the actual cross-sectional area of the specimen, is used, it is found that the stress-strain curve increases continuously up to fracture.

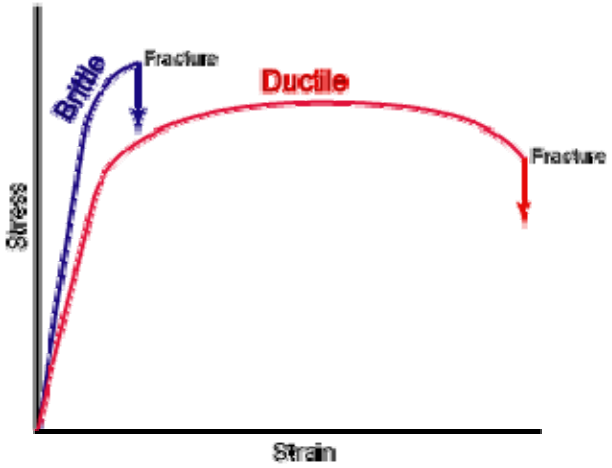

Figure 2.12. Engineering stress-strain curve of a brittle and a ductile material.

The elastic moduli, yield stress and ultimate strength are obtained from the stress-strain curve. As can be seen in the figure, the stress and strain initially increase with a linear relationship. This is the linear-elastic portion of the curve and it indicates that no plastic deformation has occurred. The slope of the line is called the modulus of elasticity or Young's modulus. To compute the modulus of elasticity, the stress is simply divided by the strain in the elastic region of the stress-strain curve. It is interesting to note that Young's moduli are generally greater in compression for most of the commonly used structural materials.

Compressive yield stress is the stress required to produce a small-specified amount of plastic deformation and is measured in a manner identical to that done for tensile yield strength. When testing metals, it is defined as the stress corresponding to 0.002 of plastic strain. Finally, the ultimate compressive strength is the stress required to rupture a specimen.

2.2.5.2. Experimental procedure and working conditions

Macroscopic compression tests were carried out using an *Instron 8562* testing machine at a strain rate of 1×10^{-4} s^{-1} at room temperature located at the *IFW Dresden*. The compression samples with an aspect ratio of 2:1.

2.2.6. Thermomechanical Analysis

In thermomechanical analysis (TMA), dimensional changes in a sample are the primary measurement, while the sample is heated, cooled, or studied at a fixed temperature. A simple schematic figure of a typical TMA instrument is shown in Fig. 2.13.

The sample sits on a support within the furnace. Resting upon, it is a probe to sense changes in length, which are measured by a sensitive position transducer, normally a Linear Variable Displacement Transducer (LVDT). The probe and support are made from a material such as quartz glass (vitreous silica), which has a low, reproducible, and accurately known coefficient of thermal expansion, and also has low thermal conductivity, which helps to isolate the sensitive transducer from the changing temperatures in the furnace. A thermocouple near the sample indicates its temperature. There is usually provision for establishing a flowing gas atmosphere through the instrument, to prevent oxidation for example, and also to assist in heat transfer to the sample.

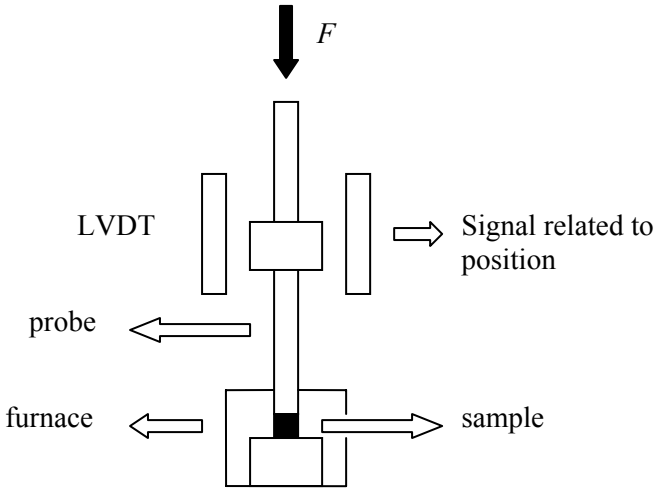

Figure 2.13. Schematic representation of a thermomechanical instrument

The load may be applied by static weights or by a force motor. This latter method gives the advantage that the applied load can be programmed to allow a greater range of experiments.

2.2.6.1. Viscostity measurements

Using a thermomechanical analyser, it is possible to measure the viscosity at any temperature of an undercooled liquid. By measuring the height of the sample in function of time, the viscosity, η, is given by the equation

$$\eta = \frac{F \cdot h}{3\pi a^2 \frac{dh}{dt}} \qquad \text{eq. 2.21}$$

where F is the applied load, a the radius of the sample, and h the height of the sample.

2.2.6.2. Experimental procedure and working conditions

Our experiments were carried out using a *TMA 7 (Perkin Elmer)* located at the *IFW Dresden*. Viscosity measurements were performed in $Cu_{60}Zr_xTi_{40-x}$ (x = 15, 20 and 30) metallic glasses. The instrument was calibrated for position measurements by heating a sample whose expansion coefficient is accurately known. It was important to prepare samples with clean, flat and parallel faces to avoid artefacts in the recorded curves. The samples for viscosity measurements were disks of 0.3 mm in height and 3mm of diameter, which were carefully prepared by a metallographic procedure to ensure parallel faces.

2.2.7. Nanoindentation

2.2.7.1. Origins of the technique

Traditionally indentation has been used to measure the hardness by applying a known load to a pyramid or sphere. After the load is removed the area of the residual imprint is measured, generally by optical microscopy. However, as interest has increased in smaller indents, the resolution of optical microscopy has become inadequate. SEM or atomic force microscopy (AFM) can be used although finding the indents is problematic and the whole process can be very time consuming, especially if large numbers of indents need to be measured. To increase the accuracy and speed of the hardness testing instrumented nanoindenters, where the force and displacement are constantly measured throughout the indentation cycle, are now routinely used.

2.2.7.2. Instrumented Pyramidal nanoindentation

As this procedure does not involve directly observing the residual area, such area must be calculated from the depth of penetration of the indenter into the surface and the associated load. Early work showed that in metals the area of contact between the indenter and the surface at maximum load is equal to the residual area after the indenter has been removed [28]. Furthermore, work on ceramic materials has revealed this to be also the case [29]. This is interesting because elastic relaxation during unloading only affects the depth of the indent.

Therefore, if the vertical elastic component of the deformation can be removed then only the plastic deformation will remain. If the depth of plastic penetration is evaluated the contact area (residual area) can be calculated if the shape of the indenter is also known.

For materials that exhibit little elastic deformation during indentation the maximum depth of indentation would be expected to give a good approximation to the plastic depth. However, this would not be suitable for elastic materials and it has been shown that for both cases the final depth would be more suitable [30]. A better approximation involves using the early stages of the unloading slope to calculate the elastic depth of the indent. This can then be removed from the total depth to give the plastic deformation. The early part of the unloading slope is also used as it is the stiffness measured across the whole contact area. This stiffness can then be extrapolated down to zero load to extract the elastic depth. Initially the stiffness was calculated from the first third of the unloading slope (assuming it to be linear) [31]. However, subsequent work indenting Aluminium, Tungsten, soda-lime glass, fused silica, quartz and sapphire showed that the unloading data was rarely linear but could be fitted with a power law relationship. More specifically the unloading data was fitted to Sneddon's solution [32] of elastic deformation of a surface by a parabola of revolution and was found to be more consistent than previous fits that had been used with either flat punch or conical indenters [29]. This formed the bases for the widely used analysis technique developed by Oliver and Pharr, which has been used in this work and will be described below.

2.2.7.3. The method of Oliver and Pharr

The method was developed to measure the hardness and elastic modulus of a material from indentation load-displacement data obtained during one cycle of loading and unloading. Although it was originally intended for application with sharp, geometrically self-similar indenters like the Berkovich triangular pyramid, it has been recognized that it is much more general than this and applies to a variety of axisymmetric indenter geometries including the sphere.

A schematic representation of a typical data set obtained with a Berkovich indenter is presented in Fig. 2.14, where the parameter F designates the load and h the displacement relative to the initial undeformed surface. During unloading, it is assumed that only the elastic displacements are recovered; it is the elastic nature of the unloading curve that facilitates the analysis. For this reason, the method does not apply to materials in which plasticity reverses during unloading. However, finite element simulations have shown that reverse plastic deformation is usually negligible [33].

There are three important quantities that must be measured from the F-h curves: the maximum load, F_{max}, the maximum displacement, h_{max}, and the elastic unloading stiffness, $S = dF/dh$, defined as the slope of the upper portion of the unloading curve during the initial stages of unloading (also called the contact stiffness). The accuracy of hardness and modulus measurement depend inherently on how well these parameters can be measured experimentally.

Another important quantity is the final depth, h_f, the permanent depth of penetration after the indenter is fully unloaded.

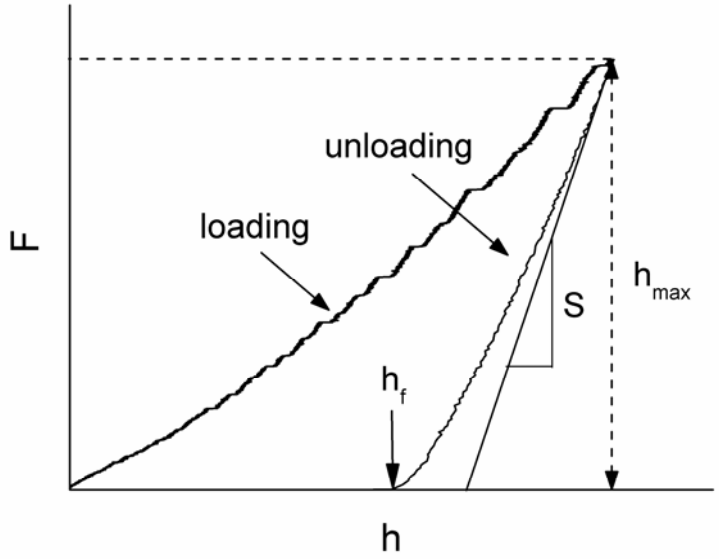

Figure 2.14. Schematic illustration of indentation load-displacement data showing important measured parameters.

The analysis used to determine the hardness, H, and the elastic modulus, E, is essential to fit the unloading curve. In the work of Oliver and Pharr, the unloading data was fitted to a relationship of the form

$$F = A'(h-h_f)^m, \qquad \text{eq. 2.22}$$

where A', m, and h_f are all described by a least squares fitting procedure. This relationship describing the unloading curve could then be differentiated to yield the initial unloading slope and therefore the initial stiffness.

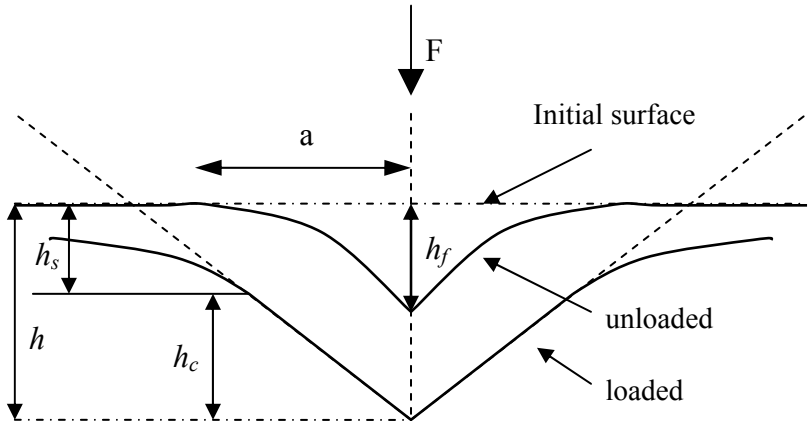

Figure 2.15. Schematic illustration of the unloading process showing parameters characterizing the contact geometry [29].

The exact procedure used to measure H and E is based on the unloading processes shown schematically in Fig. 2.15. The basic assumption is that the contact periphery sinks in in a manner that can be described by models for indentation of a flat elastic half-space by rigid punches of simple geometry [32,34]. Assuming, that pile-up is negligible, the elastic models show that the amount of sink-in, h_s, is given by:

$$h_s = \varepsilon \frac{F_{\max}}{S} \qquad \text{eq. 2.23}$$

where ε is a constant that depends on the geometry of the indenter. Using eq. 2.22 to approximate the vertical displacement of the contact periphery, it follows from the geometry of Fig. 2.15 that the depth along which contact is made between the indenter and the specimen, $h_c = h_{max} - h_s$, is:

$$h_c = h_{\max} - \varepsilon \frac{F_{\max}}{S} \qquad \text{eq. 2.24}$$

Letting $f(h)$ be an area function that describes the projected (or cross sectional) area of the indenter at a distance h back from its tip, the contact area A is then

$$A = f(h_c). \qquad \text{eq. 2.25}$$

The area function, also sometimes called the indenter shape function, must carefully be calibrated by independent measurements so that deviations from nonideal indenter geometry are taken into account. These deviations can be quite severe near the tip of the Berkovich indenter, where some rounding inevitably occurs during the grinding process.

Once the contact area is determined, the hardness is calculated using:

$$H = \frac{F_{\max}}{A} \qquad \text{eq. 2.26}$$

Note that because this definition of hardness is based on the contact area under load, it may deviate from the traditional hardness measured from the area of the residual hardness impression if there is significant elastic recovery during unloading. However, this is generally important only in materials with extremely small values of E/H [35].

Measurement of the elastic modulus follows from its relationship to contact area and the measured unloading stiffness through the relation

$$S = \beta \frac{2}{\sqrt{\pi}} E_{eff} \sqrt{A}\,, \qquad \text{eq. 2.27}$$

where E_{eff} is the effective elastic modulus defined by

$$\frac{1}{E_{eff}} = \frac{1-\nu^2}{E} + \frac{1-\nu_i^2}{E_i}. \qquad \text{eq. 2.28}$$

The effective modulus takes into account the fact that elastic displacements occur in both the specimen, with Young's modulus E and Poisson's ratio ν, and the indenter, with elastic

constants E_i and ν_i. Equation 2.27 was originally derived for elastic contact only [36], it has subsequently been shown to apply equally well to elastic-plastic contact [37].

The determination of the contact area is of crucial importance for the values of H and E. Therefore, the shape of the indenter and the compliance of the whole system must be known. Unfortunately the two are linked but the compliance is addressed first. The total compliance of the system C is made up of the load frame compliance C_f and the specimen compliance C_s

$$C = C_f + C_s \qquad \text{eq. 2.29}$$

As sample compliance is equal to $1/S$, system calibrations are generally based on the relation

$$C = C_f + \frac{\sqrt{\pi}}{2E_{eff}} \frac{1}{\sqrt{A}}. \qquad \text{eq. 2.30}$$

Then if C vs $A^{-1/2}$ is plotted the intercept will be the load frame compliance but to achieve this, the diamond area function needs to be known. In this case, it can be seen that the best results will be when $A^{-1/2}$ is small i.e. large indents. As the exact diamond area function is not known the relationship for a perfect Berkovich indenter is used, and is given by

$$A = 24.5\, h_c^2 \qquad \text{eq. 2.31}$$

After C_f has been determined the contact area can be calculated for a range of indentation loads. The contact areas are then plotted again h_c and fitted to the relationship

$$A = \sum_{n=0}^{8} C_n (h_c)^{2-n} \qquad \text{eq. 2.32}$$

where C_n are constants. This will then yield new values for the contact areas, and influence the load frame compliance and reduced modulus values. The new values are then submitted into eq. 2.30 and new values calculated, the process is iterated until convergence is achieved. At convergence C-C_f = 0, eq. 2.29.

2.2.7.4. Possible measurement errors

When using this technique and indentation in general a few problems should be kept in mind. Firstly, the method of Oliver and Pharr takes all measurements of height from the surface. Therefore, if the material flows plastically and piles up around the indenter the contact height could actually be above the surface. This would mean that some of the area supporting the load would not be accounted for. This was elegantly demonstrated by indentation experiments in copper [38]. Indents were made and the hardness measured. Pile up of material was observed surrounding the indents, and it was ground away. Later the indenter was again placed in the indent with the same load as before, and it was shown that the indenter sank into the material, yielding a lower measured hardness.

Further problems can arise with very shallow indents. This is because in all work with pyramidal indenters, the tips are assumed to be sharp even when their shape may deviate from a perfect Berkovich or Vickers pyramid. However, a pyramidal tip is never perfectly sharp; it is always rounded at some length scale. This results in shallow indents being carried out with a spherical tip, which do not induce plastic deformation immediately. Instead, they produce an elastic response from the material. This could mean, in an extreme case, a perfect elastic indent being formed, which would give rise to a material with an infinite hardness.

Detecting the surface of the sample accurately arise problems for the *H* and *E* determination. This might be insignificant for large indents but if the indent depth is around 50 nm, inaccuracies in surface detection of even a few nanometres will lead to significant errors.

2.2.7.5. Experimental procedure

Nanoindentation tests were carried out using different nanoindenters: *Triboscope nanoindenter (Hysitron)*, *Nano Test 600 machine (Micro Materials Ltd.)* and *Nano Indenter XP (MTS Systems Corp.)*, located at the *IFW Dresden*, *University of Cambridge* and *MATGAS (Barcelona)*, respectively. The second nanoindenter was equipped with a hot stage. The analysis software employed in all the cases uses the method of Oliver and Pharr to determine the *H* and *E* of the studied specimens.

High temperature indentation was carried out using a hot stage designed by *Micro Materials* for their nanoindenters. The sample was mounted onto a heated stage, and the tip was also heated by a resistance coil. A heat shield was fitted between the stage and the rest of the indenter to limit the temperature rise of the electronic components during indentation.

The samples for nanoindentation measurements were carefully prepared by the following metallographic procedure:

a) The samples are embedded in epoxy resin.

b) They are subsequently polished in order to leave the surface to a mirror appearance.

This process is first carried out using silicon carbide sand paper. Afterwards a more refined polishing is performed using diamond paste (of 6, 3 and 1 μm in particle size) and finally with a colloidal suspension of 0.04 μm SiO_2 particles.

References

[1] Blackburn MJ, Malley DR: Materials & Design 1993; 14:19.

[2] Löffler JF: Intermetallics 2003; 11:529.

[3] Cahn RW: Encyclopedia of Materials Science and Engineering, (Pergamon Press, Oxford 1988, Collection: Advances in Materials Science and Engineering).

[4] Bridgeman J: Processing of Metals under High Pressure Conditions, (Tehizdat, Moscow 1936).

[5] Zhilyaev AP, Nurislamova GV, Kim BK, Baró MD, Szpunar JA, Langdon TG: Acta Mater 2003; 51:753.

[6] Valiev RZ, Ivanisenko YV, Rauch EF and Baudelet B: Acta Mater 1966; 44:4705.

[7] Inczédy J, Lengyel T, Ure AM: Compendium of Analytical Nomenclature: definitive rules 1997, (Blackwell, Oxford, 1998).

[8] Borchard HJ: J Am Chem Soc 1957; 78:41.

[9] Borchard HJ: J Inorg Nucl Chem 1960; 12:552.

[10] Kissinger HE: Anal Chem 1957; 29:1702.

[11] Knoll M: Z Tech Phys 1935; 16:467.

[12] von Ardenne M: Z Tech Phys 1938; 109:553.

[13] von Ardenne M: Z Tech Phys 1938; 19:407.

[14] Ojeda Sahún JL: Métodos de Microscopía Electrónica de Barrido en Biología, (Servicio de Publicaciones de la Universidad de Cantabria, Santander, 1997).

[15] Goldstein JI: Scanning Electron Microscopy and X-Ray Microanalysis, (Plenum Press, Nova York, 1981).

[16] Goldstein JI: Practical Scanning Electron Microscopy, (Plenum Press, Nova York, 1976).

[17] Amelinckx S: Electron Diffraction and Transmission Electron Microscopy, Materials Science and Technology – A comprehensive treatment, (VCH, Weinheim, 1992, Edited by: Cahn RW, Haasen P, Kramer EJ).

[18] Friedrich W, Knipping P, Laue MV: Ann Phys 1912; 41:971.

[19] Darwin CG: Phil Mag 1914; 27:315.

[20] Ewald PP: Ann Phys 1916; 49:117.

[21] Bragg WL: Proc Camb Phil Soc 1912; 17:43.

[22] Cullity BD: Elements of X-Ray Diffraction, (Addison-Wesley Publishing Company Inc., Boston 1978).

[23] Klug HP, Alexander LE: X-Ray Diffraction Procedures, (Wiley, Nova York, 1974).

[24] Keijser TH, Landford JI, Mittemeijer EJ, Vogels ABP: J Appl Cryst 1982; 15:308.

[25] Galí S: Boletín de la Sociedad Castellonense de Cultura 1989; LXV:627.

[26] Scherrer P: Gött Nachr 1918; 2:98.

[27] PCPDFWIN, JCPDS-ICDD ©, 1997.

[28] Tabor D: The Hardness of Metals, (Oxford University Press, London, 1951).

[29] Oliver WC, Pharr GM: J Mater Res 1992; 7:1564.

[30] Pethica JB, Hutchings R, Oliver WC: Philos Mag A 1983; 48:593.

[31] Doerner MF, Nix WD: J Mater Res 1986; 1:601.

[32] Sneddon IN: Int J Eng Sci 1965; 3:47.
[33] Pharr GM, Bolshakov A: J Mater Res 2002; 17:2660.
[34] Sneddon IN: Fourier Transforms, (McGraw-Hill, New York, 1951).
[35] Bolshakov A, Pharr GM: J Mater Res 1998; 13:1049.
[36] Pharr GM, Oliver WC, Brotzen FR: J Mater Res 1992; 7:613.
[37] Cheng CM, Cheng YT: Appl Phys Lett 1997; 71:2623.
[38] Chaudhri MM, Winter M: J Phys D: Appl Phys 1998; 21:370.

3. Results and Discussion

3.1 Deformation behaviour of a Pd-based metallic glass under an indenter

Pd-based bulk metallic glasses have been investigated for a long time due to their high glass-forming ability [1]. However, the first report of the quaternary $Pd_{40}Cu_{30}Ni_{10}P_{20}$ metallic glass appeared on 1996 [2]. This alloy possesses an extremely high glass-forming ability, and high thermal stability against crystallization. For example, a cooling rate of merely 0.1 K/s is required to suppress crystallization, and to form a metallic glass sample with diameter up to 72 mm. Due to its high thermal stability and large supercooled liquid region, many studies on the basic fundamentals of metallic glasses have been published using this alloy, i.e. measurements of viscosity [3], crystallization [4], diffusion [5] and structural changes in the glass transition [6]. But the possibility of casting large bulk samples has allowed extensive and detailed investigations on the fundamentals of the mechanical properties of metallic glasses. Namely, the deformation dependence on the strain rate in compressive and tensile tests at room temperature was studied by Mukai et al. [7,8]. According to Mukai et al., serrated flow was clearly visible in compression, but at high strain rates, the specimens fractured near the yield stress due to the activation of multiple shear bands. Therefore, as will be shown in the next section, nanoindentation studies on this alloy shed light on the shear band formation and propagation in metallic glasses, and its dependence with the strain rate. Furthermore, its high thermal stability allows nanoindentation studies at temperatures above room temperature.

3.1.1 Thermal and structural characterization of $Pd_{40}Cu_{30}Ni_{10}P_{20}$ bulk metallic glass

A master alloy with composition $Pd_{40}Cu_{30}Ni_{10}P_{20}$ has been prepared by arc melting a mixture of the pure elements in an Ar atmosphere. A cylinder of 5 mm diameter and 50 mm length has been obtained by Cu mould casting in an Ar atmosphere.

3.1.1.1. Thermal stability of $Pd_{40}Cu_{30}Ni_{10}P_{20}$ metallic glass

Figure 3.1 shows the DSC curve of the studied alloy obtained at 0.167 K/s between 500 and 760 K. This curve presents a glass transition temperature (T_g), followed by a supercooled liquid region ($\Delta T_x = T_x - T_g$) and one exothermic crystallization peak. T_x is the temperature of the onset of the crystallization peak and is 663 K. Therefore, the supercooled liquid region spreads

over about ΔT_x = 95 K. After the crystallization peak, an endothermic peak is also present and corresponds to the melting of the alloy, with a liquidus temperature (T_l) of 750 K. Hence, the reduced glass transition temperature (T_g/T_l) of this alloy is 0.75 and thus it is really a good glass former.

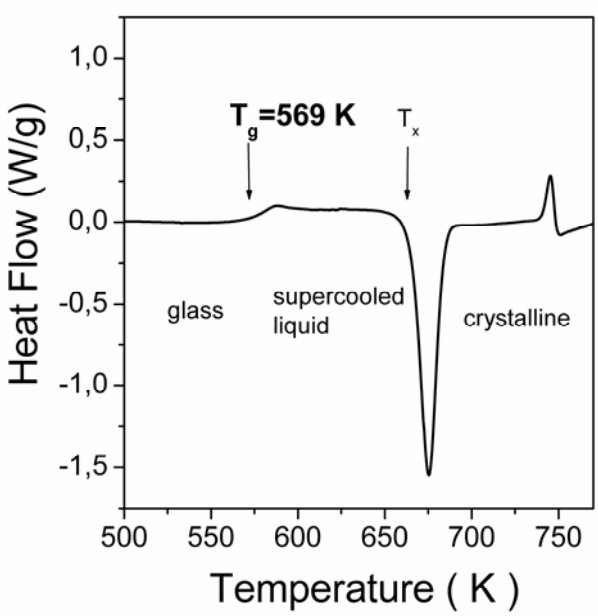

Figure 3.1. Continuous heating DSC curve obtained at 0.167 K/s for $Pd_{40}Cu_{30}Ni_{10}P_{20}$ bulk metallic glass.

3.1.1.2. Microstructural characterization $Pd_{40}Cu_{30}Ni_{10}P_{20}$ metallic glass

Figure 3.2 shows the XRD pattern of the as-quenched rod. A broad and symmetric halo is present at Q = 2.88 A^{-1}, the first halo is followed by a subsequent smaller halos, typical for a fully amorphous phase. Similar results on the same alloy are found in the literature [6].

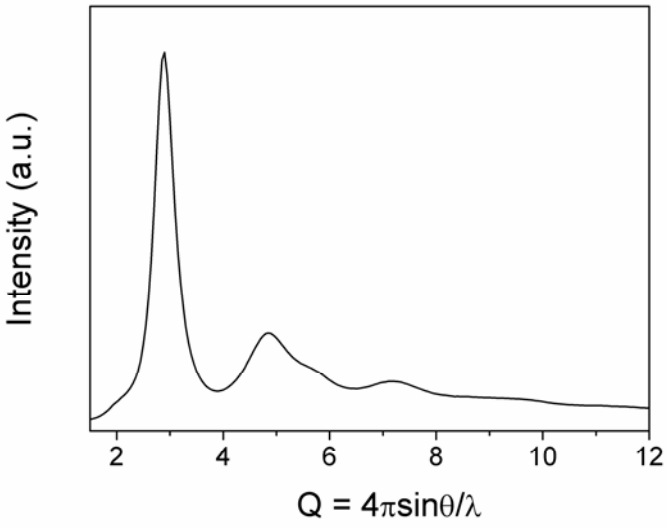

Figure 3.2. X-ray diffraction pattern of $Pd_{40}Cu_{30}Ni_{10}P_{20}$ alloy corresponding to the BMG sample.

3.1.2 Anelastic, plastic deformation and mechanical softening during nanoindentation in $Pd_{40}Cu_{30}Ni_{10}P_{20}$ bulk metallic glass

Time-dependent deformation processes (i.e., anelasticity) during nanoindentation have been investigated. Deformation under constant load has been characterized as a function of prior loading rate and temperature. The constant-load displacement of the indenter into the sample shows classic relaxation kinetics and reveals the importance of anelasticity for the overall mechanical behavior of metallic glasses at the nanoscale.

Furthermore, plastic effects during nanoindentation tests of this $Pd_{40}Cu_{30}Ni_{10}P_{20}$ bulk metallic glass have been studied after loading over a wide range of indentation rates (from 0.04 up to 6.4 mN s^{-1}) under the standard load control mode. New results using the feedback displacement control mode are also presented. The plastic deformation manifests as pop-in events during loading. The dependence of the pop-in formation on the loading rate is analysed. A softening effect occurs when increasing the loading rate. This is explained by the differences in plastic deformation at different indentation rates. The displacement control mode was used to avoid the shear localization of the free volume, leading to the almost complete absence of pop-ins along the loading curve. The obtained results suggest that plastic flow in bulk metallic glasses is governed by the rate of creation of free volume, which depends on the strain rate, and its localization into shear bands.

3.1.2.1 Deformation under constant-load

The load-time function employed under the load control mode is shown in Fig. 3.3. It consists of two loading segments, two holding force segments of 150 s at a maximum force of 10 mN and two unloading segments at 1 mN s^{-1}. The two load holding segments are labeled as hold 1 and 3 in Fig. 3.3. Different loading rates (0.2, 0.5, 1.0 and 2.0 mN s^{-1}) were used, keeping the same in both cycles, to study the influence of this parameter on the holding segment. A low-load segment of 60 s was introduced between the two cycles to measure the thermal drift and also the relaxation time (labelled as hold 2). The second cycle was added to investigate time-dependent plastic deformation that could take place during the first one. Finally, a low-load holding segment was added to determine whether the thermal drift rate has changed significantly during the course of the experiment. Furthermore, nanoindentation experiments have been performed at different temperatures (298, 311, 323 and 336 K) in air. The number of tests at every indention condition was 10 in all the cases. The high reproducibility of the material response allowed statistical calculations from the raw data giving standard deviations lower than 10% of the average calculated values. The hardness and the reduced elastic modulus were derived from these load-displacement curves using the method of Oliver and Pharr [9].

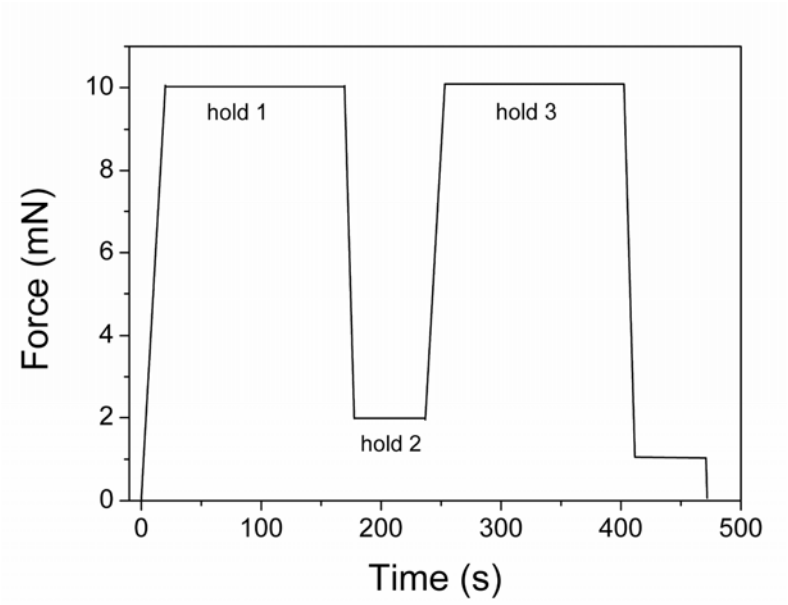

Figure 3.3. Load function used to study anelasticity by nanoindentation tests.

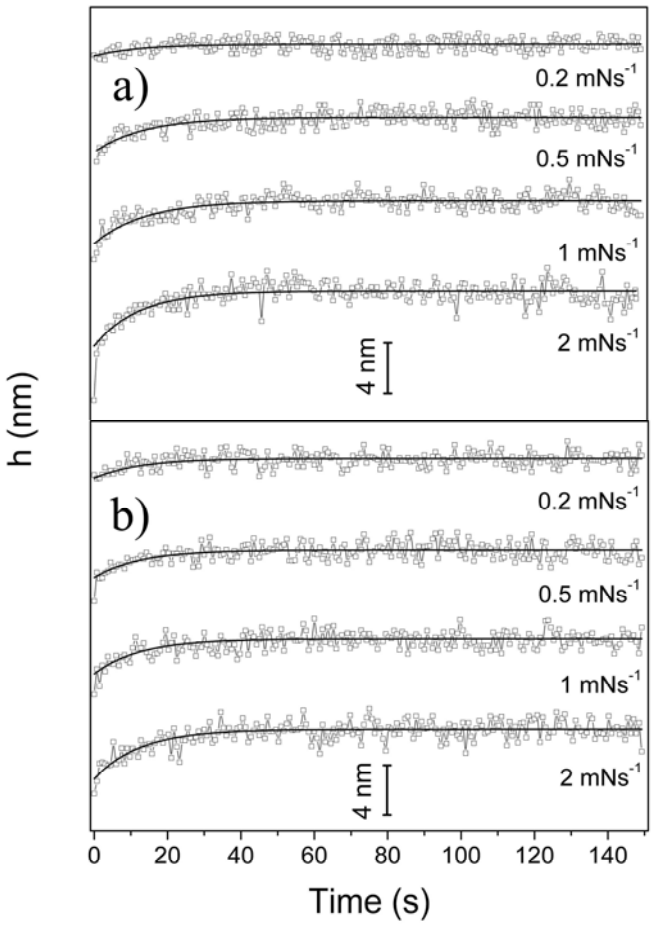

Figure 3.4. Evolution of the indenter displacement into the sample (h) during the first, a), and third, b), load holding segment for different loading rates at 298 K. The continuous lines are the fits of the data using eq. 3.1.

From the maximum penetration depths at the end of hold 1 and hold 2 it is possible to evaluate the overall plastic deformation occurring during the first load-unload cycle. For sharp indenters with fully elastic loading and unloading, the penetration depth h is linearly proportional to $F^{1/2}$ [10,11], where F is the applied load. Thus, plotting h versus $F^{1/2}$ and extrapolating to $F = 0$, one can obtain the overall plastic deformation, which was found to be around 150 nm for all the investigated loading rates.

Figures 3.4 a) and b) show the evolution of the indenter displacement into the sample during the first and third load holding segment, respectively, for different loading rates at 298 K. To facilitate comparison, the starting points at maximum load for different loading rates are aligned. Similar tendencies can be observed over the range of indentation rates. Once the maximum force has been reached, the indenter still penetrates into the material, and for higher loading rates the penetration is more pronounced. Nevertheless, the overall maximum indentation depth achieved at the end of the holding segment is similar. As a consequence, the measured hardness and reduced elastic modulus are independent of the loading rate, as shown in Table 3.I. Remarkably, for a given loading rate, the overall penetration depth obtained after the second loading+hold 3 is the same as that after the first loading+hold 1.

	dF/dt (mN s^{-1})			
	2.0	1.0	0.5	0.2
H (GPa)	4.7 ± 0.2	4.6 ± 0.2	4.6 ± 0.2	4.5 ± 0.2
E_r (GPa)	114 ± 2	110 ± 3	110 ± 3	109 ± 3

Table 3.I. Influence of the indentation rate on the hardness, H, and the reduced Elastic modulus, E_r.

The nanoindentation experiments were also performed at different temperatures. Figures 3.5 a) and b) show the h versus time dependences for first and third load holding segment, respectively, at different temperatures for experiments with a loading rate of 2 mN s^{-1}.The ultimate penetration is more pronounced at lower temperatures. But at a given temperature, the final indentation depth after the loading+constant-load segments is approximately independent of the loading rate.

The displacements of the indenter into the sample during the different load holding segments show classic relaxation kinetics, described by:

$$h(t) = h_0\left[1 - \exp\left(-\frac{t}{\tau}\right)\right] \qquad \text{eq. 3.1}$$

where t is the time, h_0 is the ultimate additional penetration that takes place during the load holding segment and τ is the relaxation time. Data shown in Figs. 3.4 and 3.5 are all fitted with eq. 3.1. The values obtained for τ are quoted in Table 3.II. Furthermore, the ultimate additional

penetration during the load holding segment evaluated directly from the experimental data ($h_{0,exp}$) is shown in Table 3.II. Both values have been averaged over the experiments performed at the different conditions. For the experiments performed at the same temperature, τ is similar for all load-holding segments independent of the loading rate. However, $h_{0,exp}$ increases with the loading rate and is larger for hold 1 than for hold 3, Table 3.II. Moreover, comparison of the different curves in Fig. 3.5 shows that time-dependent deformation occurs faster at higher temperatures. Therefore, τ clearly decreases with increasing temperature.

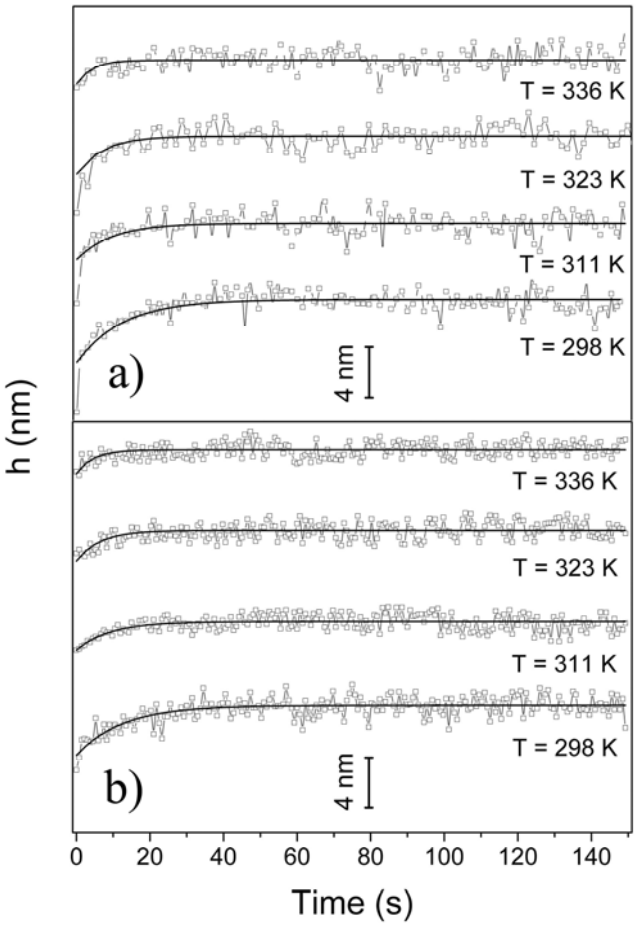

Figure 3.5. Evolution of the indenter displacement into the sample (h) during the first, a), and third, b), load holding segment at different temperatures for experiments with a loading rate of 2 mN s^{-1}. The continuous line is the fit of the data using eq. 3.1.

The similarity of the relaxation times at the same temperature independently of the loading rate and the load holding segment, see Table 3.II, leads to the idea that the underlying mechanism governing this behaviour must be the same. Furthermore, the overall maximum depth is the same after the first and third load holding segments, denoting that the material behaves anelastically and has almost no time-dependent plastic deformation during the holding segments. It is noteworthy that anelasticity has already been described in metallic glasses [12,13]. Moreover, the penetration during the holding segments ($h_{0,\exp}$) is larger for faster

loading rates (see Table 3.II) since the material has less time, during the loading segment, for anelastic strains to reach the stable elastic state.

Fitted parameters	dF/dt (mN s^{-1})	Temperature							
		298 K		311 K		323 K		336 K	
		Hold 1	Hold 3	Hold 1	Hold 3	Hold 1	Hold 3	Hold 1	Hold 3
τ (s)	2.0	12.5	13.6	9.3	9.0	6.5	6.1	4.6	4.6
	1.0	12.7	13.1	9.5	9.1	6.2	6.3	-	-
	0.5	13.2	11.4	9.4	9.3	6.2	6.3	-	-
	0.2	12.5	12.7	-	-	-	-	-	-
$h_{0,\mathrm{exp}}$ (nm)	2.0	7.5	5.3	4.8	2.8	2.6	1.3	2.2	1.4
	1.0	6.1	3.3	3.2	2.3	2.2	1.6	-	-
	0.5	5.0	3.8	2.4	1.7	1.5	1.4	-	-
	0.2	3.4	1.6	-	-	-	-	-	-

Table 3.II. Dependence of relaxation time, τ, and the penetration depth during the holding segments, $h_{0,exp}$, on the temperature and the loading rate. Note that standard deviations of the data are < 10% of the average calculated values. Some values are missing because they are too small to be reliably evaluated.

The effects of anelasticity on the elastic contribution to the overall material deformation are schematically represented in Fig. 3.6 [14]. This figure explains why the penetration during hold 1 is larger than during hold 3. During hold 2 the material shows anelasticity and it is completely relaxed. Hence, when the indenter again applies a constant loading rate during the second loading segment, the material deforms from a different elastic state, with higher elastic modulus, than in the first loading segment. As a result, $h_{0,\mathrm{exp}}$ for hold 3 is always lower than for hold 1 (Fig. 3.6).

Since anelasticity is a thermally activated process, the relaxation time is expected to decrease with increasing temperature, as observed experimentally. Namely, for a thermally activated relaxation, each value of the distributed relaxation time has the form [12-15]:

$$\tau = \tau_0 \exp\left(\frac{Q}{kT}\right) \qquad \text{eq. 3.2}$$

where Q is the activation-energy of the process, τ_0 is a pre-exponential factor, k is Boltzmann's constant and T is the absolute temperature. In Fig. 3.7, the logarithm of the mean of the

observed relaxation times at each temperature is plotted as a function of 1/*T*. The temperature dependence of τ is described by an effective activation energy of 0.26 eV, evaluated from the slope of the linear fit in Fig. 3.7.

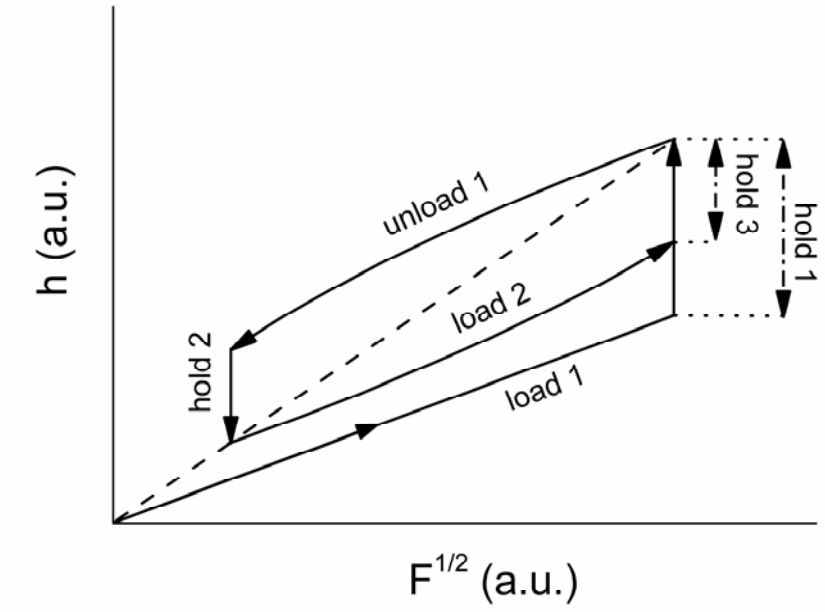

Figure 3.6. Schematic representation of the overall anelastic material behaviour during the nanoindentation experiments. The discontinuous line indicates the equilibrium elastic response of the material (i.e., if there were no anelastic strain).

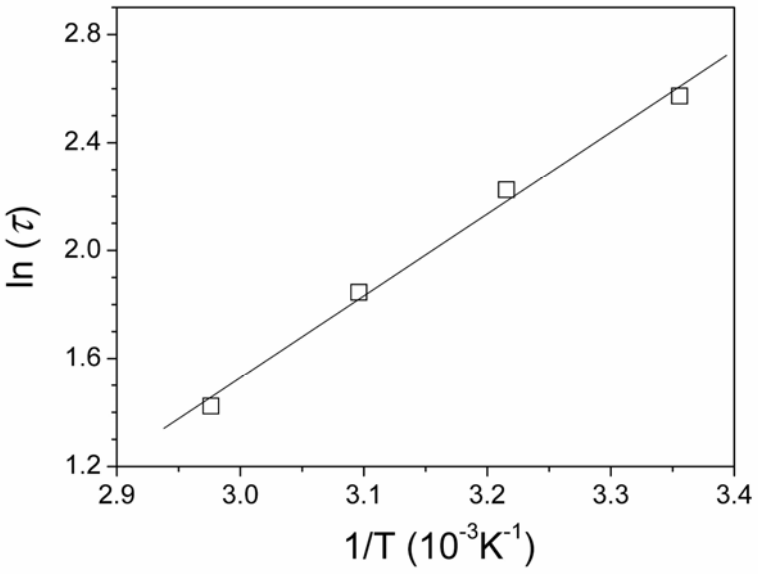

Figure 3.7. Logarithm of the mean of the observed relaxation times (t_0) at each temperature plotted as a function of 1/T. The straight line is the fit of the data using eq. 3.2.

It is well-known that anelasticity in metallic glasses is a process distributed over a certain range of activation energies [13], and Ocelik et al. already studied the influence of the

loading time on the calculated spectra of activation energies for the anelastic processes in an amorphous ribbon [12]. In particular, a fully developed spectrum was only observed for long enough loading times (around 100 s) at 618 K. It was concluded that not all of the anelastic deformation defects with longer relaxation time were activated at faster loading rates and therefore did not take part in the creep recovery process. The low temperatures and the high loading rates used in the present nanoindentation experiments favour anelastic deformation processes with shorter relaxation times, failing to be activated the ones with longer τ and therefore not taking part in the creep recovery [12], and finally leading to the low observed Q. The scatter on the collected data does not allow calculating the distribution on the activation energies. Moreover, at high temperatures, the penetration during the constant-load segments decreases because the characteristic relaxation time is so short that partial anelastic recovery can occur during the loading.

The microscopic mechanisms of anelasticity for short time and low temperature anelastic relaxations are similar to those for reversible annealing-induced structural relaxation, according to Kursumovic and Cantor [13]. Therefore, the low activation energy together with the short relaxation time found in our case indicate that local atomic shear motions which change only the local shear stress, but break no atomic bonds, should be the mechanism responsible of the anelasticity process observed.

3.1.2.2. Plastic deformation and mechanical softening

Deformation and shear banding in metallic glasses has been investigated to some extent [7,8,15-21]. Early conventional uniaxial compression tests on BMGs showed that plastic flow was typically found to be serrated [21]. However, this was not the case for uniaxial tension tests, in which BMGs fail following the propagation of a single shear band without appreciable plastic deformation [8]. Moreover, Mukai et al. have shown that for a Pd-base BMG, the fracture strength depends on the strain rate applied during compression testing [7], while this dependence disappears when tensile testing the same material [8].

The plastic flow is a time dependent deformation and in a metallic glass is governed by the rate of the free volume creation. Defect concentration, c_f, as defined in section 1.1.5, depends on a certain critical amount of free volume necessary to form a defect [17]. It is already established that at a given temperature, thermal dilatation creates a certain amount of free volume and a relaxation process tends to annihilate free volume by structural rearrangements. This can be expressed as [22,23],

$$\frac{dc_f}{dt} = -k_r c_f \left(c_f - c_{f,eq}\right) \qquad \text{eq. 3.3}$$

in which k_r is the rate factor for the thermally activated process of structural relaxation, $c_{f,eq}$ is the defect concentration in equilibrium at the given temperature. Furthermore, eq. 3.3 has also been shown to be valid under low stress [24]. However, when a metallic glass is subjected to a

reasonable strain rate, van Aken et al. proposed that the defect concentration rate may be expressed as [24],

$$\frac{dc_f}{dt} = -k_r c_f \left(c_f - c_{f,eq}\right) + P\left(c_f, T, \dot{\varepsilon}\right) \qquad \text{eq. 3.4}$$

in which $P\left(c_f, T, \dot{\varepsilon}\right)$ is an additional production term, which depends on the strain rate, $\dot{\varepsilon}$. Furthermore, at an applied stress, the free volume is created when an atom squeezes into a neighbouring free volume site with slightly smaller volume, and annihilated by structural rearrangements [17]. In compression tests at high stresses, the creation rate exceeds the annihilation rate, resulting in a softening as the free volume increases. Once the stress drops after each serration, the driving force for free volume creation decreases and both rates become equal.

In order to study the plastic deformation under an indenter, load and depth control modes have been used. The mechanisms of plastic deformation during nanoindentation have been investigated using the load control mode and different loading rates. It is worth noting that the range of loading rates used in this study is among the widest reported in the literature [25-27], allowing a more complete analysis of the material behaviour. The depth controlled mode indentation has been used to control shear band formation and propagation.

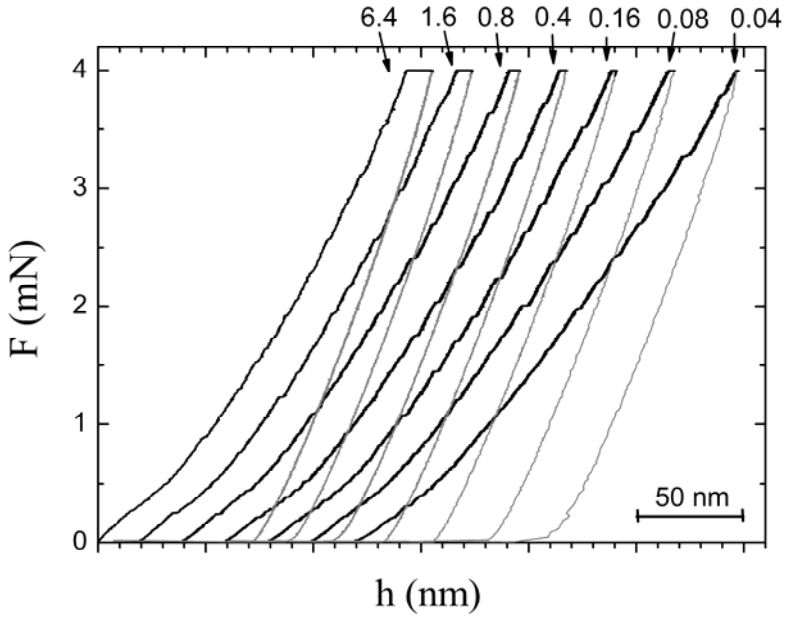

Figure 3.8. Load-displacement (F-h) curves measured during nanoindentation tests in load control mode, at different loading rates. Loading rates are shown on the top of the figure and are in mN/s.

Figure 3.8 shows load-displacement (F-h) nanoindentation curves obtained under load control mode for the different loading rates studied. The curves have been displaced by 20 nm from each other in order to facilitate their observation. Important differences and clear tendencies can be observed from rapid to slow indentation rates. Pop-in events or steps appear

in all the loading curves, but they decrease in size and number as the loading rate increases, tending to become imperceptible at the highest loading rate. The apparent absence of serrations at low depths may be due to either lack of resolution of the system [28], or the fully elastic response of the material in the first nanometers of penetration [29]. Similar results have also been previously reported in the literature [25-28]. Furthermore, the maximum indentation depth achieved at the end of the first indentation segment (loading part of the curve) for each experiment increases as the loading rate decreases. The difference in indentation depth between the highest and the lowest loading rate is around 40 nm, which is about 30 % of the total depth measured at 6.4 mN s^{-1}. Such a large difference has not been observed by other authors [25-28], probably because their experiments were performed in a narrower loading rate range, without reaching such low loading rates as in the present work.

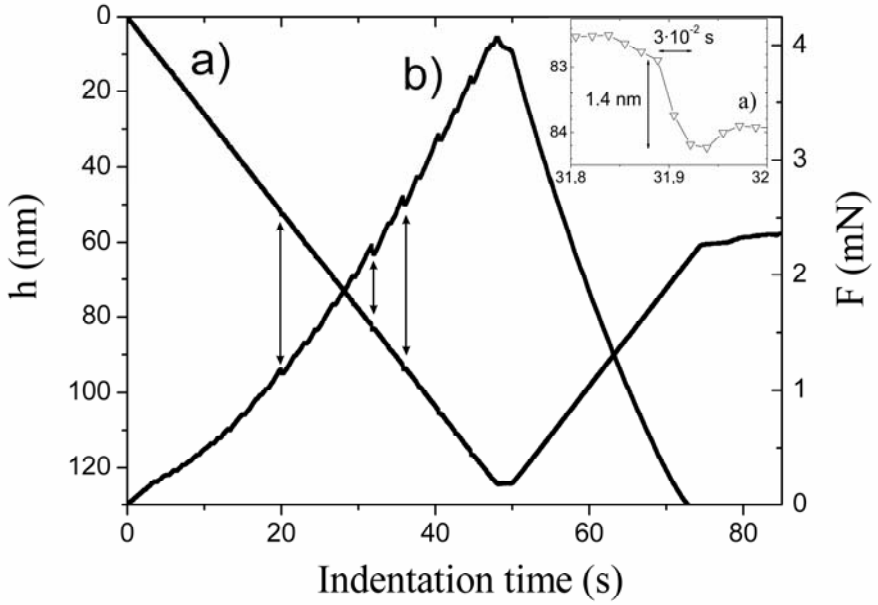

Fig. 3.9. Dependence of the displacement into the sample, h, curve a), and the applied force, F, curve b), on the indentation time in a displacement control mode test. The inset shows a detail of a pop-in event.

Figure 3.9 shows both the evolution of the applied force, *F*, and the displacement into the sample, *h*, as a function of time for a displacement control mode nanoindention. In this experiment the depth variation is kept as constant as possible by the feedback indenter position controller for every indentation segment. Since the material tends to produce sudden penetration steps at given loads, the applied force is reduced when this occurs in order to maintain the desired constant penetration rate. Nevertheless, the pop-in events occur in time intervals of around 10^{-2}s (see Fig. 3.9 inset) and, consequently, the feedback response of the equipment is not fast enough in some of the cases to completely avoid them, giving rise to steps of up to 2 nm. This can be seen in Fig. 3.9, where the applied force deviates from a continuous and smooth line, and the displacement curve exhibits some small steps but rapidly goes back to a straight line, in both cases at equal indentation times. Moreover, the displacement rate during loading, 2.6 nm s^{-1}, that would be approximately equivalent to a loading rate of 0.09 mN s^{-1} under load

control mode, considering the overall duration of the loading indentation segment, leads to a maximum penetration depth of the loading segment (120 nm) more similar to the maximum depth achieved during loading at 6.4 mN s^{-1} (144nm), than at 0.08 mN s^{-1} (165 nm).

The average pressure, P_m, applied to the sample during the indentation experiments was calculated dividing the instantaneous force by the projected contact area. The dependence of the average applied pressure on the indenter penetration is shown in Fig. 3.10. Apparently, P_m decreases after the pop-in events for the load control mode experiments [see curves a), b) and c)], and the drops are more marked when the loading rate is lower. Moreover, the average pressure is always higher for the experiments performed at higher loading rate.

A strain softening (i.e. a progressive decrease of P_m) is also observed during the force holding segment [16]. The displacement control mode experiment presents a serrated average pressure, with a roughly constant maximum value in each serration, except for h = 80, 100 and 115 nm, where the maximum values of the serrations become lower. This can be related with uncontrolled pop-ins in the displacement into the sample, also visible in Fig. 3.9. Therefore, the strain softening in the displacement control mode mainly occurs at these displacement values and compared to experiments carried out in the load control mode, is overall lower as evidenced by the larger values of the average pressure obtained in this case in the overall range of displacement into the sample.

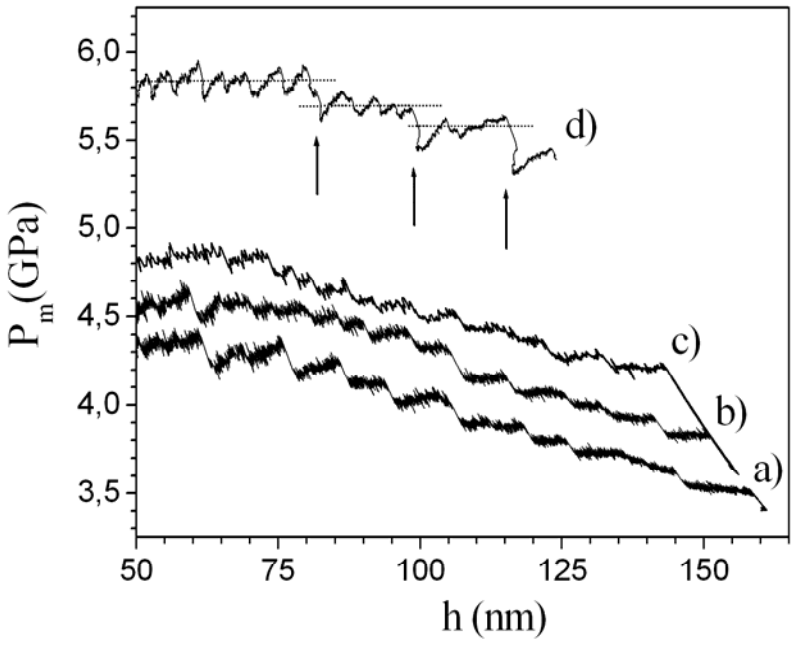

Fig. 3.10. Mean pressure applied to the material as a function of displacement into the sample, h, for the experiments at constant loading rate a) 0.08, b) 0.8 and c) 6.4 mN/s and constant displacement rate d) 2.6 nm/s.

The formation of pop-ins in the loading curve, see Fig. 3.8, may be associated with shear band propagation, where instantaneously, the nanoindenter drops into the material, in agreement with the literature [25-28]. Furthermore, Fig. 3.10 shows that the pop-in events, or

shear bands propagation, result in a reduction of the mean applied pressure to the material, related to a decrease of the stress into the material [30]. The relationship between these steps and the stress decrease with shear banding agrees with Argon's model for shear localization in metallic glasses [31]. Argon pointed out, by using a mechanistic model, that metallic glasses under high stress should be prone to shear localization. According to his results, the localization starts out slowly but then proceeds with a rapid, almost discontinuous, jump until all the plastic deformation is concentrated into a shear band in the material. Moreover, the localization is accompanied by a stress drop of several percent [31].

Shear band propagation can be minimized by displacement control mode experiments, as shown in Fig. 3.9. Once the shear localization starts to concentrate in a band, the nanoindenter releases some force from the tip leading to a stress drop in the material and, consequently, the shear localization stops. Nevertheless, some free volume is already created in each serration and accumulates in the material. Therefore, although it is not initially localized in a shear band, finally, at a critical amount, it localizes unavoidably, thus leading to a step in the displacement into the sample curve. It is worth noting that when a shear band is formed, the mean pressure necessary to start the shear localization for the subsequent bands is lower, see curve d) in Fig. 3.10, particularly appreciable around 80, 100 and 115 nm.

This mechanical softening is also observed and exacerbated in the load control mode experiments, see Fig. 3.10. Spaepen already predicted the softening in metallic glasses at high stresses due to a dramatic increase in the free volume [17]. Moreover, Steif et al. [32] suggested that once a shear band is created, the free volume accumulated in the shear band should increase the average free volume leading to a softening as observed in Fig. 3.10 for all the curves.

At the lowest loading rate investigated, the plastic deformation is mainly achieved during loading, since during the load holding segment virtually no further deformation occurs, as shown in Fig. 3.4. This implies that the free volume created as a consequence of the high stress localizes into the shear bands and has time to coalesce, as suggested by Li et al. [33,34], leading to a maximum decrease of the stress in each pop-in event, as can be seen in curve a) of Fig. 3.10. Consecutive shear bands progressively require a lower stress to form, since free volume has already been created in the material [32]. At higher loading rates, a lower plastic deformation is achieved during the loading segment. In this case, the term $P\left(c_f, T, \dot{\varepsilon}\right)$, in eq. 3.4, should be more important, because the rate of defect concentration should not create fast enough the necessary free volume to reach the equilibrium defect concentration and, hence, the equilibrium plastic deformation conditions. However, the localization of the free volume in a shear band should be limited by kinetics at high loading rates as suggested by Schuh et al. [35]. For these reasons, pop-in events are smaller at higher loading rates and, as a consequence, the plastic deformation during loading segment is lower, the mean pressure decrease in each pop-in event is smaller, and the stress in the material at the same displacement into the sample is higher for higher loading rates. Therefore, during the loading segments, at higher indentation rates, there has not been enough time to create and accommodate free volume into shear bands, and the excess stress accumulated in the material favours the higher anelastic deformation during the creep segment for higher loading rates [14,17,31].

3.1.2.3 Summary

In summary, during constant-load segments, the displacement of the indenter into the sample shows classic relaxation kinetics with relaxation times which are temperature-dependent but independent of the constant-load segment and the loading rate. The observations can be consistently interpreted in terms of anelasticity of the metallic glasses. Furthermore, plastic flow of a metallic glass under an indenter at low loading rate is accommodated by shear localization of the free volume into shear bands, leading to a serrated loading curve. High loading rates limit the localization and coalescence of free volume into shear bands. A strain softening is observed as a consequence of shear band formation. In displacement control mode tests, shear localization of the free volume is inhibited since the nanoindenter releases some force from the tip, leading to a stress drop in the material and, consequently, the shear localization stops. Shear band formation provokes a drop in the necessary mean pressure to start the shear localization for the subsequent bands.

3.2 Thermal, structural and mechanical characterization of Cu-based Bulk Metallic Glasses

Since the first synthesis of a La-based bulk glassy alloy by copper mould casting in 1989 [1], a number of bulk glassy alloys have been reported in multi-component systems such as Mg [36], Zr [37], Pd-Cu [38], Ti [39]. These systems with high glass-forming ability are usually composed of four and more elements. However, the search for good glass-forming systems as simple (i.e. two or three elements) and cheap as possible is important to extend the applications of metallic glasses. In 2001, the first report on the formation of a BMG alloy in Cu-based alloys containing more than 50 at.% appeared [40]. Inoue et al. obtained fully amorphous rods of 4 mm in diameter in the $Cu_{60}(Zr_xTi_{1-x})_{40}$ ternary system. The development of these Cu-based BMGs is important to broaden the applications of metallic glasses due to its low cost. The discovery of these new Cu-based BMGs has motivated many research studies on their crystallization behaviour and mechanical properties [41-46]. Furthermore, several authors have tried to improve their ductility [45].

In this section, results on the crystallization behaviour, the thermal stability and the mechanical properties of $Cu_{60}Zr_xTi_{40-x}$ amorphous alloys (x=15, 20, 22, 25, 30) prepared by melt-spinning and copper mould casting are presented.

3.2.1 Thermal characterization of $Cu_{60}Zr_xTi_{40-x}$ metallic glasses

3.2.1.1. Thermal stability of $Cu_{60}Zr_xTi_{40-x}$ metallic glasses

Figure 3.11 shows the DSC curves of the studied alloys obtained at 0.33 K/s between 670 and 870 K. These curves present a glass transition temperature (T_g), followed by a supercooled liquid region ($\Delta T_x = T_x - T_g$) and several exothermic crystallization peaks (T_{p1}, T_{p2}, T_{p3}). T_x, T_{p1}, T_{p2} and T_{p3} are the temperatures of the onset and the maximum of the crystallization peaks, respectively. The characteristic temperatures of the main transformations at this scanning rate are presented in Table 3.III. As can be seen, the crystallization process between 670 and 870 K depends on the Zr content. For x = 20, 22, 25 and 30 two crystallization stages were observed, whereas more complex crystallization behavior was found for x = 15. The supercooled liquid region reached a maximum for x = 22. However, the supercooled liquid region value may also be influenced by the quenching conditions [41]. The reduced glass transition temperature (T_g/T_l) is shown in Table 3.III for each composition and as can be seen from the table, it is not greatly influenced by the composition. This parameter indicates the glass forming ability. Therefore, the samples studied are relatively good glass formers. The apparent activation energies (E_a) of the different processes were evaluated and the values obtained, see table 3.III, indicate high thermal stability. It is worth mentioning that the x = 25 and 30 alloys

also presented crystallization peaks at higher temperatures. However, in this study, we focused in the two first crystallization stages.

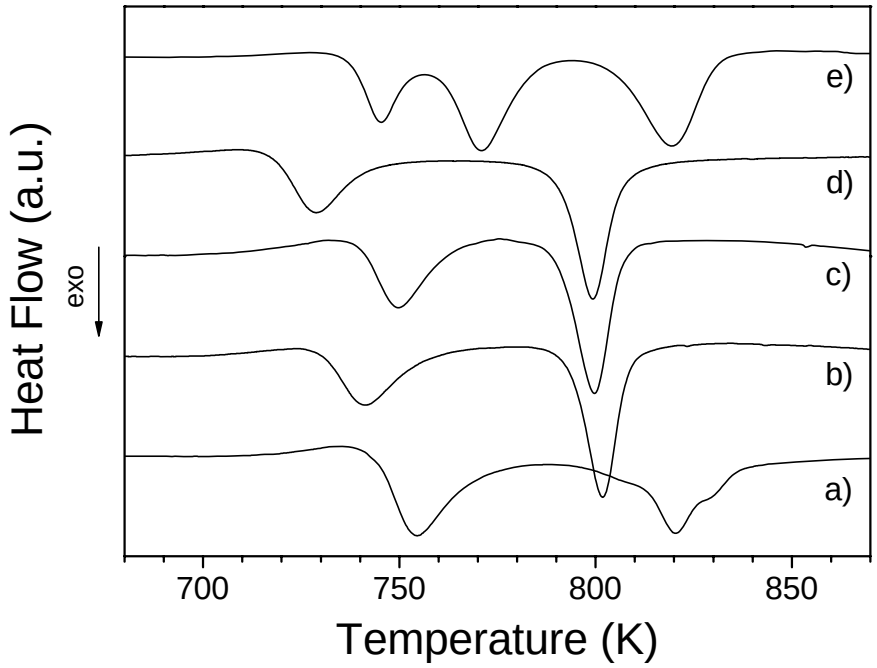

Figure 3.11. Continuous heating DSC curves obtained at 0.33 K/s for $Cu_{60}Zr_xTi_{40-x}$, a) x = 30, b) x = 25, c) x = 22, d) x = 20 and e) x = 15.

	T_g	T_g/T_l	T_x	ΔT_x	T_{p1}	E_{a1}	T_{p2}	E_{a2}	T_{p3}	E_{a3}
$Cu_{60}Zr_{15}Ti_{25}$	706	0.61	736	30	745	4.5	770	3.2	820	2.43
$Cu_{60}Zr_{20}Ti_{20}$	681	0.60	718	37	728	4.3	799	3.6		
$Cu_{60}Zr_{22}Ti_{18}$	694	0.60	735	41	749	4.2	800	3.6		
$Cu_{60}Zr_{25}Ti_{15}$	703	0.61	729	26	741	3.4	802	3.8		
$Cu_{60}Zr_{30}Ti_{10}$	715	0.61	741	26	754	3.9	820	4.2		

Table 3.III. Characteristic temperatures for the glass transition (T_g), the onset of crystallisation (T_x) and the peaks (T_{p1},T_{p2}, T_{p3}), obtained from the continous heating experiments between 670 and 870 K at 0.33 K/s for the $Cu_{60}Zr_xTi_{40-x}$ alloys and activation energies for each composition and each exothermic peak. Temperatures are in K and activation energies in eV.

3.2.1.2. Viscosity measurements of $Cu_{60}Zr_xTi_{40-x}$ metallic glasses

Viscosity is a key parameter to describe the kinetic slowdown when a melt is undercooled below its liquidus temperature, but also to monitor the glass transition and the

crystallization of a metallic glass during heating. The increase of viscosity with undercooling reflects the increasingly longer time scale for structural rearrangements in the supercooled liquid state. If the viscosity reaches a value of 10^{12} Pa·s upon undercooling, the intrinsic time scale for maintaining metastable equilibrium becomes comparable to the laboratory time scales, i.e. the cooling time. The liquid freezes to a glass, namely it vitrifies. However, when a metallic glass is heated, near the glass transition the mobility of the atoms is higher and the viscosity becomes measurable and lower than 10^{12} Pa·s, as shown in section 1.1.3. However, when the crystallization starts, the atoms are trapped in the crystalline net and at a critical volume fraction of crystals, the material cannot flow leading to a high viscosity, i.e. > 10^{12} Pa·s [47].

Figure 3.12 shows the viscosity dependence on the temperature for x = 15 a), 20 b) and 30 c), measured at a heating rate of 0.167 Ks^{-1}. In order to better understand the change in viscosity, DSC curves of each alloy are also presented in the same graph. In all the cases the viscosity starts to decrease near the glass transition temperature.

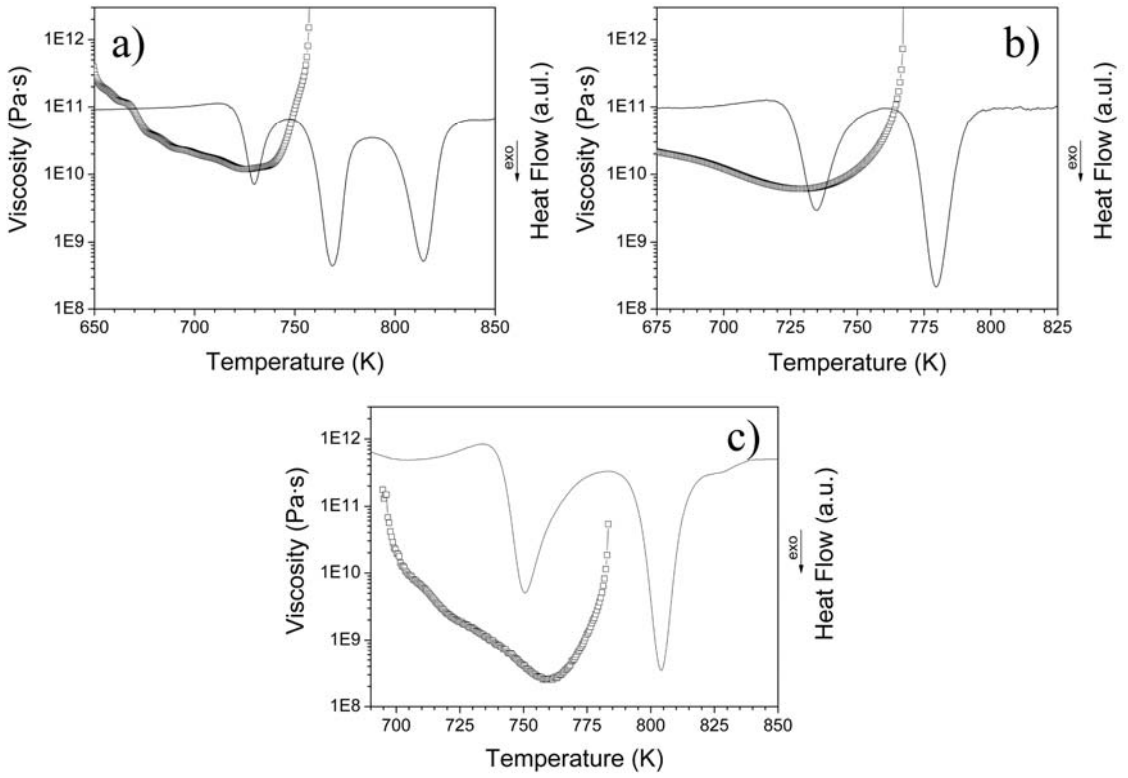

Figure 3.12. Viscosity(□) and heat flow (continuous line) as a function of the temperature for different studied alloys, both obtained at 0.167 Ks^{-1}, a) x = 15, b) x = 20 and c) x = 30.

During the first crystallization peak the viscosity continues to decrease. Therefore, the precipitation of nanocrystals is slow and does not provoke the increase of viscosity according to Einstein's equation for the flow of mixtures [48]. This equation accounts for the viscosity change due to a small volume fraction of spherical particles suspended in a medium of known viscosity, and may be expressed as

$$\eta_{eff} = \eta(1 + 2.5\xi) \qquad \text{eq.3.5}$$

η_{eff} is the viscosity of the mixture, η is the viscosity of the surrounding medium, and ξ is the volume fraction of particles. According to eq. 3.5, it is immediately apparent that any volume fraction of crystals would not cause an increase of the viscosity of two orders of magnitude as observed in all the cases and hence, the matrix dominates the change in viscosity during the first crystallization peak. Therefore, the equilibrium viscosity of the non-crystalline matrix has itself changed significantly probably because the matrix has changed its composition towards a state with a lower equilibrium viscosity [47].

The precipitation of crystals during the first crystallization process may reach a critical volume fraction after the peak temperature, the material flow is hindered and therefore the viscosity increases. Further precipitation of crystals leads to a high viscosity, , i.e. > 10^{12} Pa·s, since the material cannot longer flow.

3.2.2. Microstructural characterization of $Cu_{60}Zr_xTi_{40-x}$ metallic glasses

Figure 3.13 shows the XRD patterns of the as-quenched ribbons. As can be seen, they present a broad and symmetric halo, which is typical for a fully amorphous phase. The halo moves from 2θ=41.4º to 40.2º when increasing the Zr content. This may be due to the fact that the atomic radius of Zr is bigger than the Ti one.

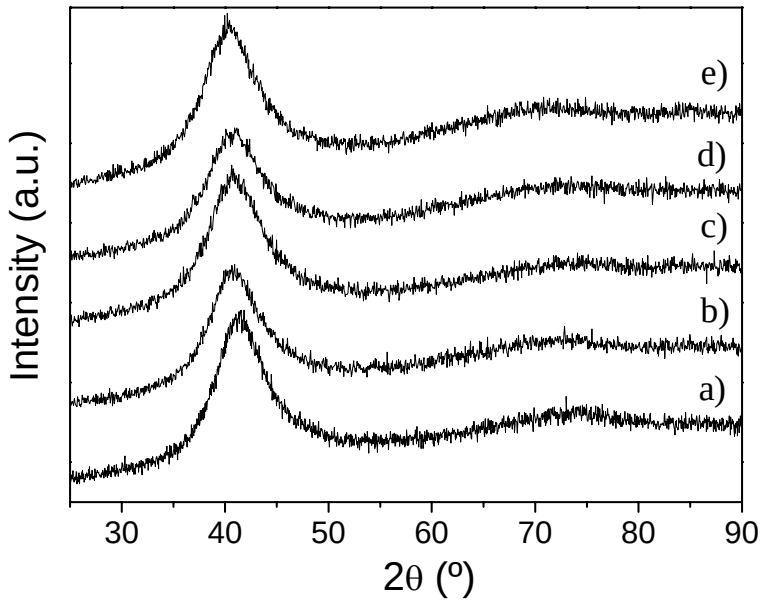

Figure 3.13. XRD patterns of the as-quenched state for $Cu_{60}Zr_xTi_{40-x}$ ribbons, a) x = 15, b) x = 20, c) x = 22, d) x = 25 and e) x = 30.

The XRD patterns obtained after the first crystallization stage, shown in Fig. 3.14, still indicate a strong amorphous halo for all the $Cu_{60}Zr_xTi_{40-x}$ alloys, but differ from the curves obtained for the as–quenched alloys. The first peak becomes narrower and its intensity increases

for all compositions, which indicates an atomic rearrangement in the initial amorphous matrix. This might be due either to a decomposition process or to the initial precipitation of some nanocrystals. Similar results were also found by Aronin et al. in $Cu_{50}Zr_{40}Ti_{10}$ alloy [49], and Jiang et al. in $Cu_{60}Zr_{20}Ti_{20}$ [42].

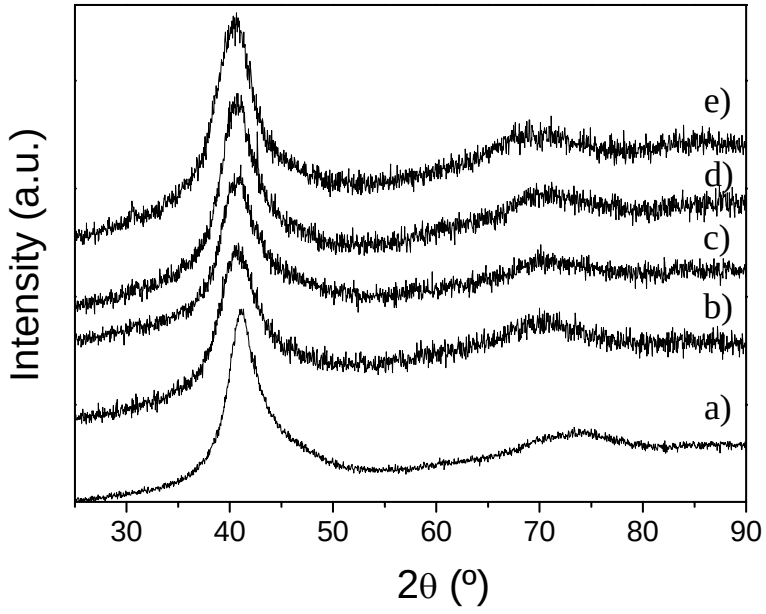

Figure 3.14. XRD patterns after first crystallization stage of $Cu_{60}Zr_xTi_{40-x}$ ribbons, a) x = 15, b) x = 20, c) x = 22, d) x = 25 and e) x = 30.

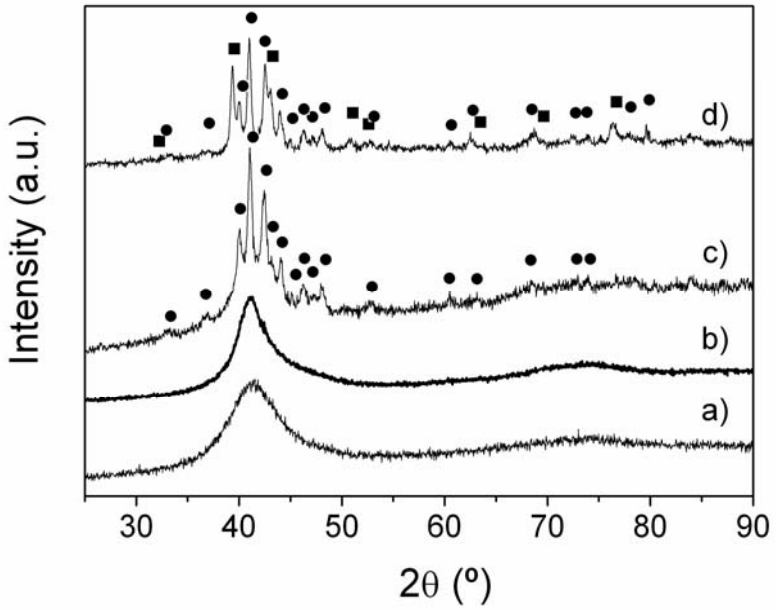

Figure 3.15. XRD patterns of $Cu_{60}Zr_{15}Ti_{25}$ ribbon of the as-quenched state, a), after first, b), second, c), and third, d), crystallization process. The symbols ● and ■ correspond to the Bragg peaks of hexagonal $Cu_{51}Zr_{14}$ and hexagonal $CuTi_2$, respectively.

Due to its different crystallization behaviour, the next step was to study the crystallization process of the $Cu_{60}Zr_{15}Ti_{25}$ alloy. Figure 3.15 shows the XRD patterns of this alloy in the as-quenched state and after heating at 0.33K/s to 745 K, 773 K and 835 K, curves a), b), c) and d) respectively.

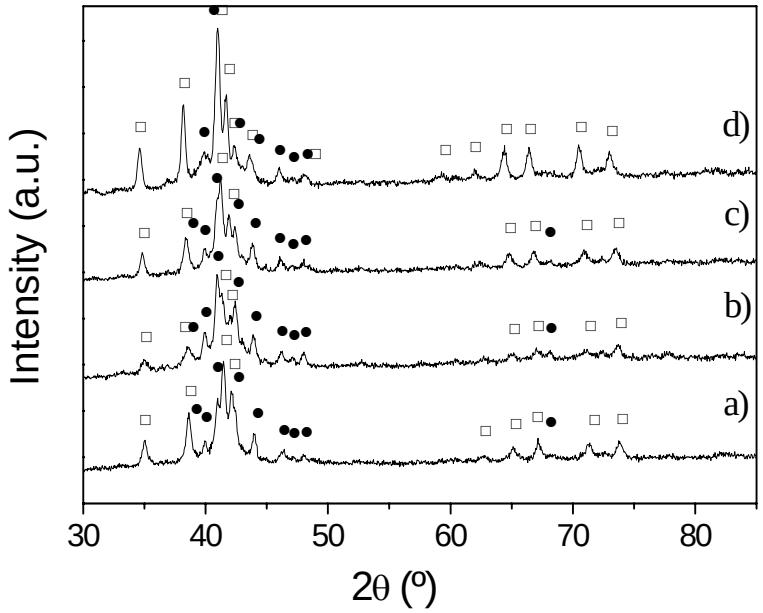

Figure 3.16. XRD patterns of $Cu_{60}Zr_xTi_{40-x}$ ribbons after second stage crystallization process, a) x = 20, b) x = 22, c) x = 25 and d) x = 30. The symbols ● and □ correspond to the Bragg peaks of hexagonal $Cu_{51}Zr_{14}$ and hexagonal Cu_2TiZr, respectively.

	2nd DSC peak				3rd DSC peak			
	hexagonal $Cu_{51}Zr_{14}$		hexagonal Cu_2TiZr		hexagonal $Cu_{51}Zr_{14}$		tetragonal $CuTi_2$	
	a (nm)	c (nm)	a (nm)	c (nm)	a (nm)	c (nm)	a (nm)	c (nm)
$Cu_{60}Zr_{15}Ti_{25}$	1.130	0.824	-	-	1.124	0.824	0.297	1.078
$Cu_{60}Zr_{20}Ti_{20}$	1.130	0.824	0.514	0.823	-	-	-	-
$Cu_{60}Zr_{22}Ti_{18}$	1.126	0.824	0.514	0.824	-	-	-	-
$Cu_{60}Zr_{25}Ti_{15}$	1.129	0.825	0.516	0.828	-	-	-	-
$Cu_{60}Zr_{30}Ti_{10}$	1.129	0.825	0.519	0.831	-	-	-	-

Table 3.IV. Cell parameters for second and third exothermic peaks of each composition.

After the second crystallization stage (continuous heating at 0.33 K/s up to 773 K), the XRD pattern curve c, reveals the presence of hexagonal $Cu_{51}Zr_{14}$ (P6/m, similar to what was reported by Liu et al. [50]) superposed to a halo produced by residual glassy phase. After continuous heating to 835 K, completion of the third exothermic peak, tetragonal $CuTi_2$

(I4/mmm) is formed and coexists with hexagonal $Cu_{51}Zr_{14}$. This result indicates that during the third crystallization peak, $CuTi_2$ nucleates and grows, while hexagonal $Cu_{51}Zr_{14}$ continues to grow. The cell parameters are quoted in Table 3.IV. The final microstructure (after heating at 0.33K/s up to 973K), consists in hexagonal $Cu_{51}Zr_{14}$-like, tetragonal $CuTi_2$-like and tetragonal CuTi-like phases.

Figure 3.16 shows the XRD patterns for x=20 until x=30 after linear heating up to the completion of the second crystallization stage. The microstructure reveals the coexistence of hexagonal $Cu_{51}Zr_{14}$-like phase and hexagonal Cu_2TiZr-like phase. In the case of x = 30, the final microstructure (after heating at 0.33 K/s up to 948 K), consists in hexagonal $Cu_{51}Zr_{14}$-like, hexagonal Cu_2TiZr-like and orthogonal Cu_8Zr_3-like phases.

3.2.3. Crystallization kinetics and microstructural evolution during first DSC peak of the $Cu_{60}Zr_{20}Ti_{20}$ amorphous alloy

In order to better understand the crystallization of the $Cu_{60}Zr_xTi_{40-x}$ alloys, the effect of continuous heating and isothermal heat treatments on $Cu_{60}Zr_{20}Ti_{20}$ amorphous ribbons was monitored by differential scanning calorimetry, X-ray diffraction, synchrotron radiation, transmission and high resolution transmission electron microscopy. Upon continuous heating, the alloy exhibited a glass-transition, followed by a supercooled liquid region and two exothermic crystallization stages, as shown in section 3.2.1.1. Decomposition of the amorphous phase was also observed and crystallization kinetics was studied by the classical nucleation theory. Deviations from the Johnson-Mehl-Avrami-Kolmogorov (JMAK) theory may be explained by the contribution of the decomposition of the amorphous matrix.

3.2.3.1. Crystallization kinetics of the $Cu_{60}Zr_{20}Ti_{20}$ amorphous alloy

Figure 3.17 shows the DSC curves obtained at different heating rates under continuous heating regimes. The characteristic temperatures of the main transformations at different heating rates (β) are presented in Table 3.V. The transformation enthalpies (ΔH_1 and ΔH_2) were obtained as the area of the first and second exothermic peak and the estimated values were 19±2 J/g and 30±3 J/g, respectively. The apparent activation energy values were evaluated from the Kissinger plots (shown in Fig. 3.17 as an inset) and found to be 4.3±0.5 and 3.6±0.3 eV for the first and second crystallization processes, respectively.

Figure 3.18.I. presents the isothermal DSC curves performed at different annealing temperatures (723, 728 and 733 K) above T_g. These curves present only an exothermic peak, with a transformation enthalpy of 20±2 J/g, which value is close to that obtained for the first crystallization peak of continuous heating.

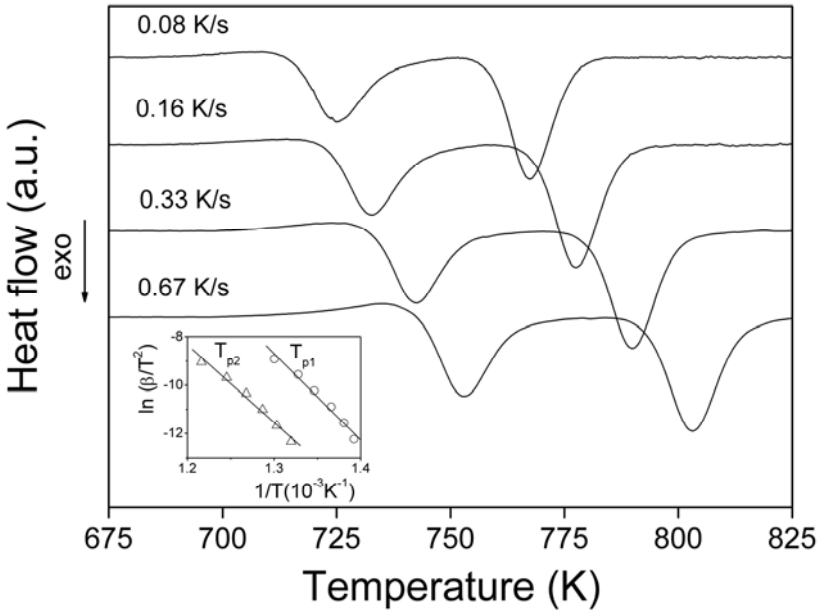

Figure 3.17. DSC curves obtained at several heating rates of the $Cu_{60}Zr_{20}Ti_{20}$. The inset shows the Kissinger plots.

β (K/s)	T_g (K)	T_x (K)	ΔT_x (K)	T_{p1}(K)	T_{p2}(K)
0.083	688.6	714.9	26.3	724.3	767.3
0.167	690.2	722.8	32.6	732.1	777.1
0.334	694.3	732.5	38.2	742.9	789.7
0.667	710.7	742.0	31.3	753.1	803.0

Table 3.V. Transformation parameters obtained from the continuous heating experiments for the $Cu_{60}Zr_{20}Ti_{20}$ alloy.

The crystallized fraction (*x(t)*) at a given time *t* is determined from the ratio between the subtended area at that time and the area of the complete exothermic crystallization peak and for each isothermal treatment are shown in Fig. 3.18.II, where dashed lines correspond to the experimental data and continuous curves are the JMAK fits to the experimental data using the theory of nucleation and growth [51-56]. The apparent activation energy of the crystallization process was calculated from the fundamental equation for the transformation rate in a solid [43], see section 2.2.1.3,

$$\ln\left(\frac{dx}{dt}\right) = \ln\left(k_0 \cdot f(x)\right) - \frac{E_a}{RT} \qquad \text{eq. 3.6}$$

where E_a is the apparent activation energy, k_0 the pre-exponential factor and *f(x)* the function which reflects the mechanism of crystallization. E_a can be evaluated from the slope of *ln(dx/dt)* vs *1/T*, at a constant transformed fraction, shown in the inset of Fig. 3.18.II. The apparent activation energy was found to be 4.2±0.5 eV, similar to the value obtained for the first

activation energy was found to be 4.2±0.5 eV, similar to the value obtained for the first crystallization peak of the continuous heating. For each isotherm, the transformed fraction curves were fitted by the JMAK model [51-56]. The calculated Avrami exponent was 1.05±0.05 corresponding to one dimensional nucleation and subsequent interface-controlled grain growth processes [51-56].

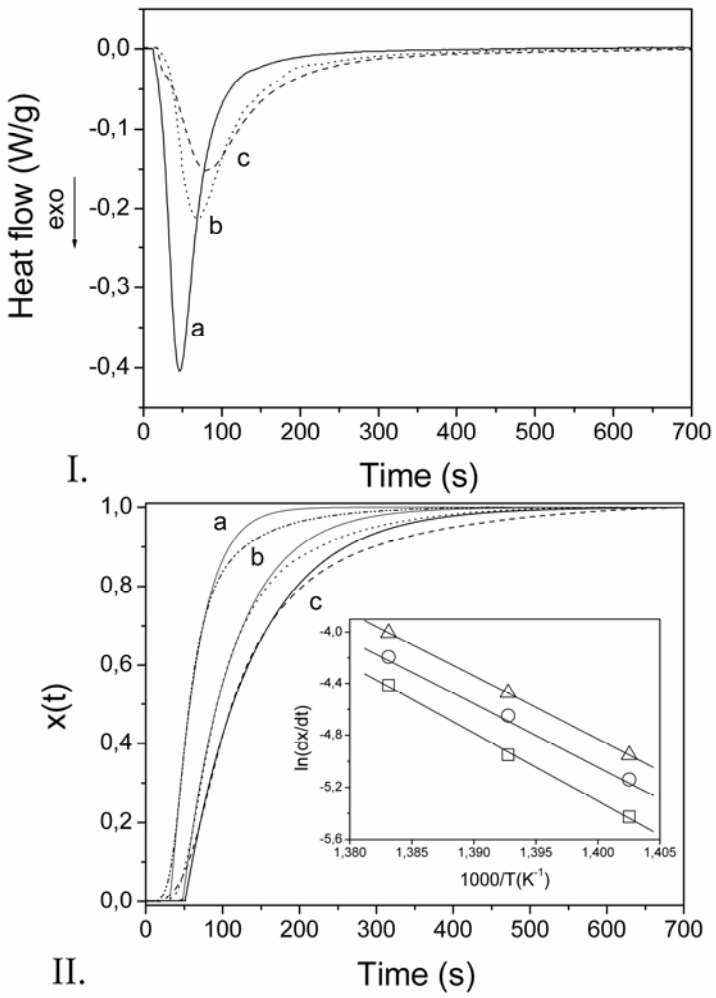

Figure 3.18. I. Isothermal annealing DSC curves of the $Cu_{60}Zr_{20}Ti_{20}$ obtained at a) 733 K, b) 728 K, c) 723 K. II. Fraction transformed x(t) (dashed lines) and JMAK approximation (solid lines) of isothermal anneals at a) 733 K, b) 728 K, c) 723 K. The inset shows ln(dx/dt) vs 1000/T for the determination of activation energy from eq. 3.6 (x = 0.4, Δ; x = 0.5, ○; and x = 0.6, □).

3.2.3.2. Microstructural development of the $Cu_{60}Zr_{20}Ti_{20}$ amorphous alloy

X-ray diffraction – Figure 3.19 shows the XRD patterns of the as-quenched ribbon and after linear heating up to 763 K and 833 K, curve a, b and c respectively. The as-quenched state exhibits a broad and symmetric halo around 2θ=41°, which is typical for a fully amorphous phase. After the first crystallization stage (continuous heating at 0.33 Ks^{-1} up to 763 K or isothermally annealed at 698 K for 7200s), the XRD pattern still indicates a strong amorphous

halo with a maximum at 2θ=40.5°. Similar results were also found by Aronin et al. [49] in $Cu_{50}Zr_{40}Ti_{10}$ alloy. As already shown in section 3.2.2, after completion of the crystallization process, curve c), the microstructure reveals the presence of hexagonal $Cu_{51}Zr_{14}$ (P6/m a= 1.130 nm, c=0.824nm, similar to the found by Liu et al. [50]) and hexagonal Cu_2TiZr-like ($MgZn_2$-type structure a= 0.514 nm, c=0.823nm) [57] crystalline phases, in agreement with the equilibrium phase diagram [58].

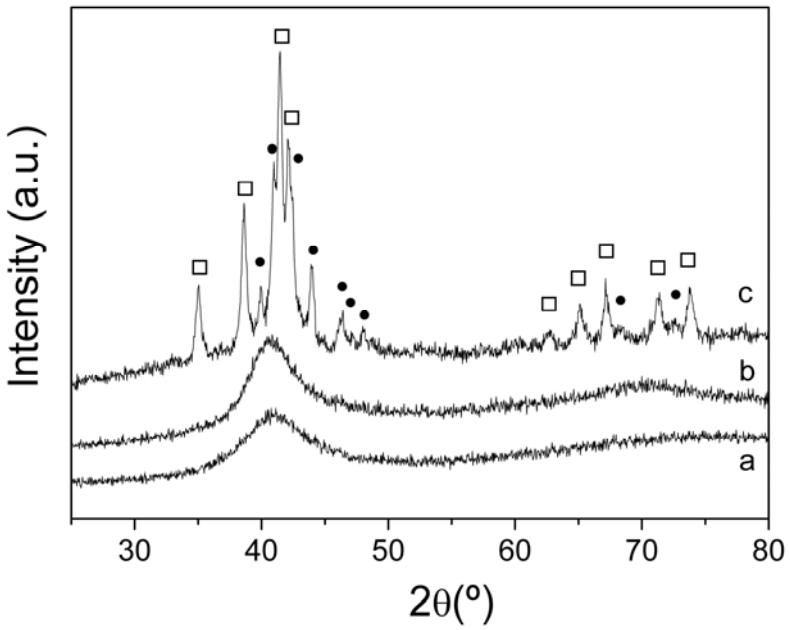

Figure 3.19. X-ray patterns corresponding to the $Cu_{60}Zr_{20}Ti_{20}$ ribbon for a) the as-quenched state, b) partially crystallized (after the first crystallization stage when continuous heating at 0.34 Ks^{-1} up to 763 K) states, and c) fully crystalline (after the second crystallization stage when continuous heating at 0.34 Ks^{-1} up to 833 K). ● and □ correspond to the Bragg peaks of hexagonal $Cu_{51}Zr_{14}$ and hexagonal Cu_2TiZr-like, respectively.

Synchrotron experiments – Real time X-ray diffraction patterns taken in transmission mode during continuous heating are shown in Fig. 3.20. The microstructural changes start with a shift of the position of the amorphous halo (T = 698 K), indicating a possible atomic rearrangement in the initial amorphous matrix. This might be due either to a decomposition process or to the initial precipitation of some crystals of hexagonal $Cu_{51}Zr_{14}$. The first crystalline peaks appear at T = 723 K indicating the formation of hexagonal $Cu_{51}Zr_{14}$ crystalline phase. At T = 763 K, some faint crystalline peaks appear corresponding to hexagonal Cu_2TiZr-like. Finally, at T = 783 K the microstructure clearly reveals the coexistence of hexagonal $Cu_{51}Zr_{14}$ and Cu_2TiZr-like. It is worth mentioning that slight changes in the characteristic temperatures may appear due to the different heating mechanism in the DSC and in the synchrotron beam.

So, concerning the data presented in Fig. 3.20, two different crystallization stages were found by the synchrotron experiment, which agrees with the DSC data. The first crystallization stage consists of nucleation and growth of hexagonal $Cu_{51}Zr_{14}$, while during the second

crystallization stage hexagonal $Cu_{51}Zr_{14}$ continues to grow and hexagonal Cu_2TiZr-like nucleates and grows. Similar results were found by Jiang et al [42].

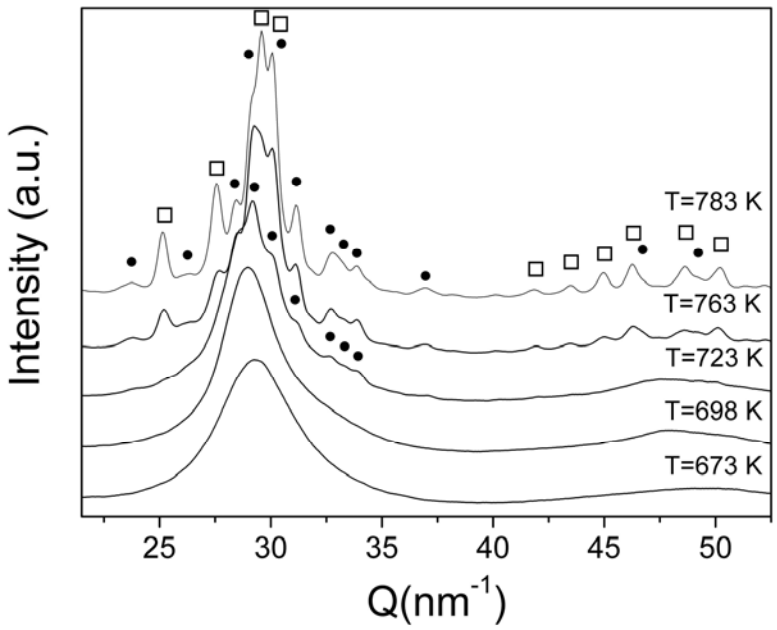

Figure 3.20. In situ XRD patterns during continuous heating of the $Cu_{60}Zr_{20}Ti_{20}$ alloy. ● and □ correspond to the Bragg peaks of hexagonal $Cu_{51}Zr_{14}$ and hexagonal Cu_2TiZr-like, respectively.

Transmission electron microscopy – The evolution of the microstructure during non-isothermal and isothermal conditions was also studied by TEM. Figure 3.21 summarizes the TEM micrographs and the corresponding selected area electron diffraction (SAED) patterns of the as-quenched sample and the sample continuously heated to 763 K (after the first crystallization stage).

For the as-quenched state the micrograph (Fig. 3.21 a) does not show any crystalline contrast, in addition, the corresponding SAED pattern is a diffuse halo, indicating a fully amorphous state (inset Fig. 3.21 a). After the first crystallization stage (continuous heating up to 763 K), the bright-field TEM image shows areas of different contrast homogeneously dispersed, with an average characteristic size of 10 to 20 nm (Fig. 3.21 b). The difference in contrast of these areas suggests different compositions. The corresponding SAED pattern still shows an amorphous halo (inset of Fig. 3.21 b), however, the diffraction rings become narrower and the position of the bright ring inside the amorphous halo indicates the initial precipitation of a crystalline phase [59]. The energy filtered transmission electron microscopy (EFTEM) image (Fig. 3.21 c) of the same crystalline state reveals the formation of homogeneously dispersed nuclei in the residual matrix. The corresponding histogram can be fitted by a log-normal distribution function with a mean particle sizes of about 4-5 nm (Fig. 3.21 d). The overall distribution seems to be compatible with a process of nucleation.

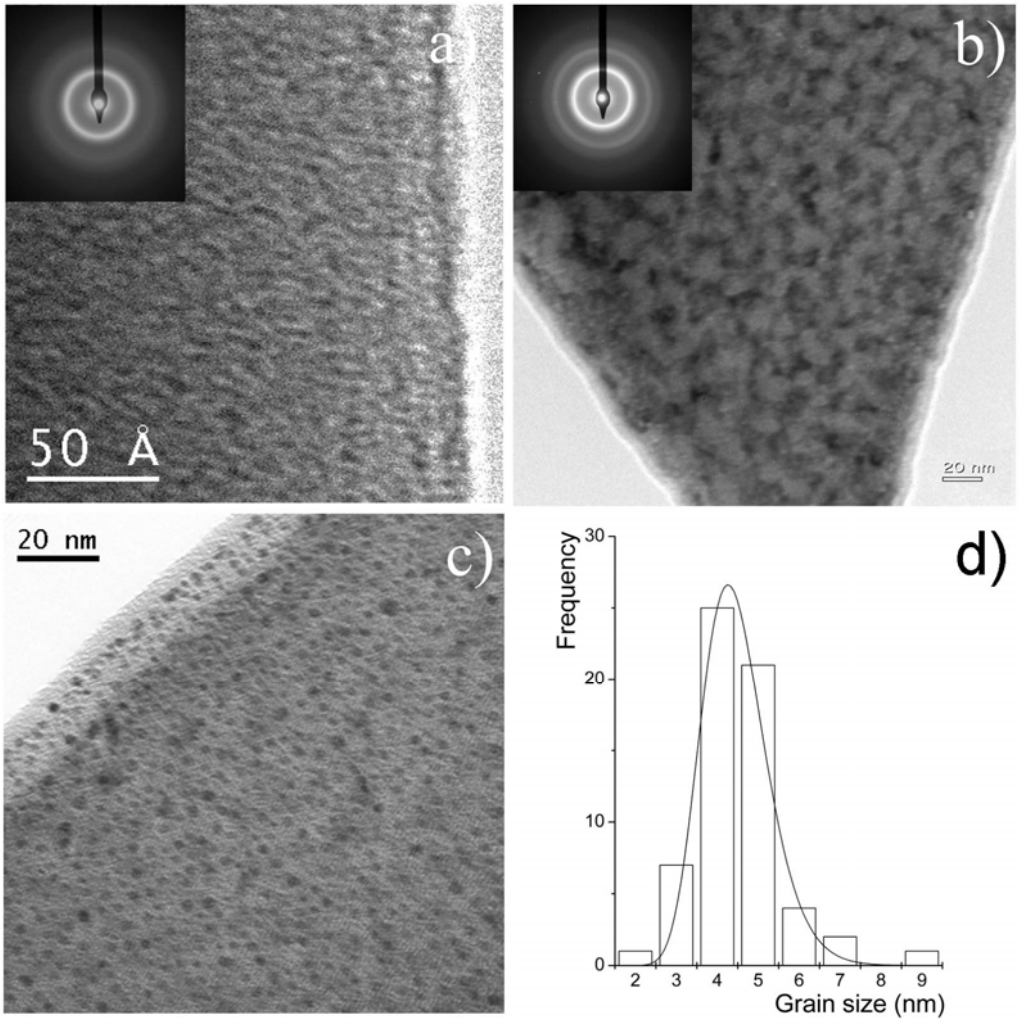

Figure 3.21. TEM micrographs and SAED patterns corresponding to the $Cu_{60}Zr_{20}Ti_{20}$ as-quenched ribbon (a) and to the sample heated up to 763 K (b). EFTEM micrograph (c) and grain size histogram corresponding to the sample heated up to 763 K (d).

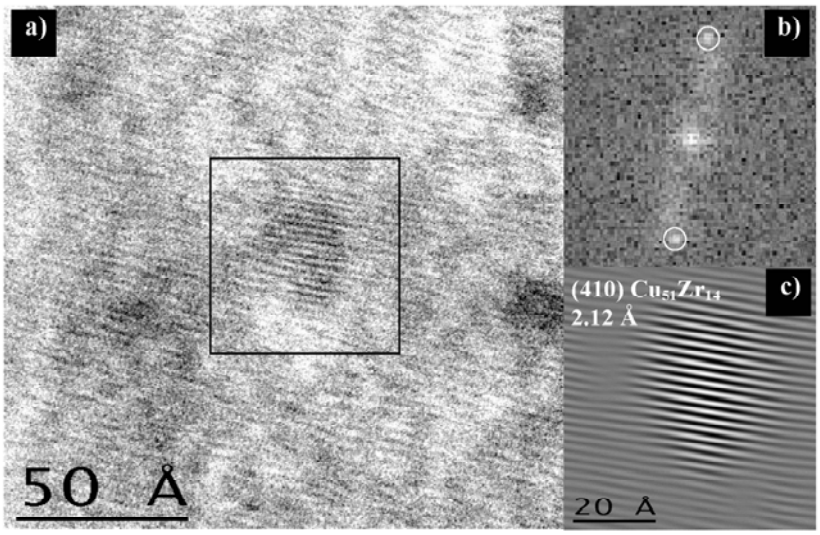

Figure 3.22. (a) HRTEM micrograph of the $Cu_{60}Zr_{20}Ti_{20}$ sample heated up to 763 K. (b) FFT of the selected nanocrystal (c) Fourier filtered reconstruction of the selected area.

A HRTEM micrograph of the same sample is presented in Fig. 3.22 a). The crystallite at the center of the image, with visible atomic planes is about 3 nm in size. Note that the surrounding material exhibits a speckle contrast characteristic of an amorphous phase. The square selection has been digitally analyzed by obtaining a fast Fourier transform (FFT), as shown in Fig. 3.22 b). The intensity peaks in the Q-space (marked by white circles) are consistent with the hexagonal $Cu_{51}Zr_{14}$ (410)-plane (2.12 Å). The corresponding filtered image (Fig. 3.22 c) shows that the grain interior exhibits periodic atomic planes.

Isothermal annealings were carried out at T = 698 K for 2700 and 7200 seconds in order to determine the evolution of the microstructure. At this temperature the isothermal DSC signal was smaller than the sensitivity of the equipment and difficult to evaluate. However, subsequent continuous heating experiments showed that the area of the first peak diminished by about 60% and almost 100%, respectively. In contrast, the area of the second peak remains practically unchanged, indicating that the contribution of the second crystallization stage is negligible.

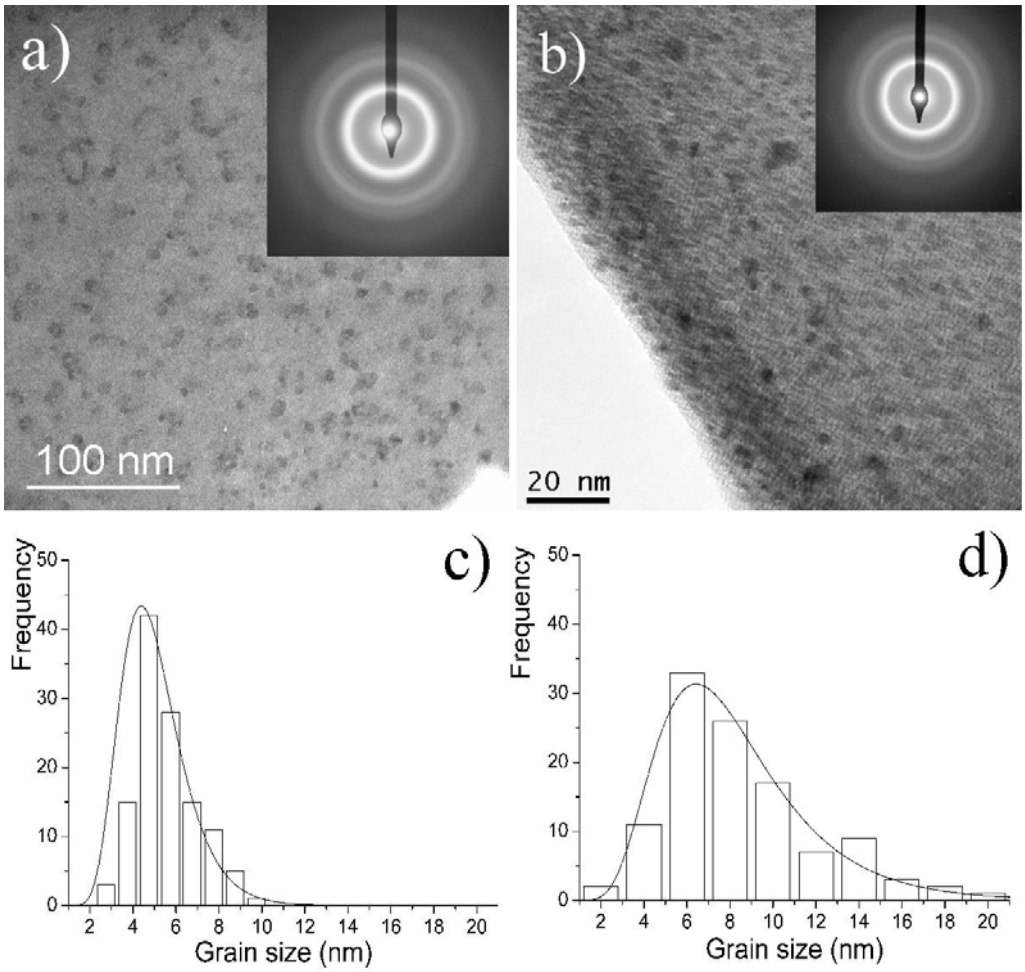

Figure 3.23. TEM micrographs and SAED patterns corresponding to the $Cu_{60}Zr_{20}Ti_{20}$ isothermally annealed samples at T_{ann}=698 K for (a) 2700 s, (b) 7200 s and grain size histograms corresponding to the isothermally annealed samples at T_{ann}=698K for (c) 2700 s, (d) 7200 s.

Figures 3.23 a) and b) illustrate the evolution of the microstructure when the as–quenched alloy was isothermally annealed at 698 K for 2700 and 7200 seconds showing the formation of small nanoscale crystallites, homogeneously dispersed in the amorphous matrix. The SAED patterns (insets in Fig. 3.23 a) and b) exhibits less diffuse rings, indicating the formation of crystalline phases. After the longer annealing time, slightly narrower SAED rings are visible; this indicates a slight grain growth. Figure 3.23 c) and d) present histograms of grain size distribution of the samples annealed at 698 K for 2700 and 7200 seconds, respectively. Particle distributions were adjusted in both cases to a log-normal distribution, and for both heat-treatments the mean grain sizes are very small, about 5nm and 7nm, respectively. These results are in agreement with usual findings in other bulk metallic glasses and rapidly quenched amorphous alloys [60-63].

A HRTEM image of the isothermally annealed state at 698 K for 2700 seconds shown in Fig. 3.24 a), reveals nanocrystals embedded in the amorphous matrix. The crystallite in the selected area is about 7 nm. The FFT image-analysis confirmed the precipitation of hexagonal $Cu_{51}Zr_{14}$ during isothermal annealing; the circles in Fig. 3.24 b) correspond to the $Cu_{51}Zr_{14}$ (411) plane (2.06 Å). The filtered image can be seen in Fig. 3.24 c).

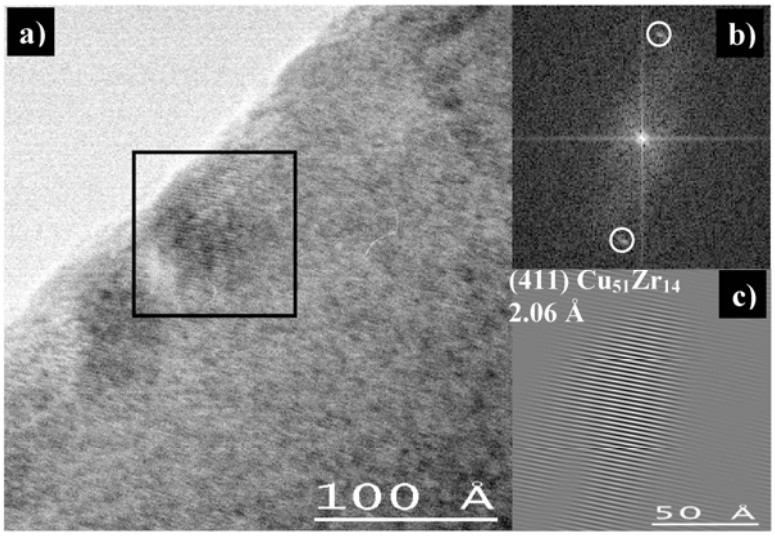

Figure 3.24. (a) HRTEM micrograph of the $Cu_{60}Zr_{20}Ti_{20}$ isothermally annealed sample at T_{ann}=698K for 2700 s. (b) FFT of the selected nanocrystal. (c) Fourier filtered reconstruction of the selected area.

3.2.4. Microstructural evolution during decomposition and crystallization of the $Cu_{60}Zr_xTi_{40-x}$ metallic glasses

Glade et al. pointed out that $Cu_{47}Ti_{34}Zr_{11}Ni_8$ metallic glass decomposes by the diffusion of Ti atoms with activation energy of 4.28±0.11eV, [59], in Cu and Ti rich zones. These values, close to those obtained for isothermal and non-isothermal anneals, suggest that decomposition of the $Cu_{60}Zr_{20}Ti_{20}$ may also occur by Ti diffusion, forming Ti-rich zones in the amorphous matrix. Furthermore, the bright-field TEM image shown in Fig. 3.21 b) presenting regions of

different contrast and with bigger crystals size than those shown in Fig. 3.21 c), also agrees with the idea of decomposition of the amorphous phase in two different composed amorphous regions [44]. It is noteworthy that Louzguine and Inoue [44] have shown that in the case of $Cu_{60}Zr_{30}Ti_{10}$ decomposition in two different amorphous regions plus precipitation of nanocrystals occurs during the first crystallization peak, although no Bragg peaks of the crystallized phase were observed in the conventional XRD pattern.

Jiang et al. [42] and also in this work, it has been established, by *in situ* synchrotron experiments, that the first crystalline phase to nucleate in $Cu_{60}Zr_{20}Ti_{20}$ is hexagonal $Cu_{51}Zr_{14}$ and coincides with the first crystallization stage. Based on these data and on the experimental results presented, the nucleation of hexagonal $Cu_{51}Zr_{14}$ may take place during first crystallization stage. According to the viscosity measurements presented in Fig. 3.12, the precipitation and growth of nanocrystals have to be slow during the first crystallization stage, since the supercooled liquid matrix dominates the viscosity changes.

The heat release for partial crystallization of the hexagonal $Cu_{51}Zr_{14}$ phase from the amorphous matrix is remarkably high. This means that there is a considerable enthalpy difference between the purely amorphous state and the partially crystallized nanocrystalline state, suggesting that the driving force for nanoscale precipitation of $Cu_{51}Zr_{14}$ is large. In contrast, the XRD patterns in Fig. 3.19 do not show any significant difference between the as-quenched and the continuously heated state. The explanation for such an observation is the high Gibbs free energy of formation for $Cu_{51}Zr_{14}$, [58], and the contribution from the decomposition of the amorphous matrix. The decomposition of the amorphous phase in Cu- and Ti-rich zones may force the formation of this phase in the Cu-rich ones. One should mention that phase separation on heating was also previously observed in the binary Cu-Zr metallic glasses [64,65]. Similarly in Zr-Be based bulk metallic glasses, phase separation was observed by several teams using different investigation techniques [66-68].

From the Avrami exponent found in the kinetics of crystallization and assuming interface-controlled growth due to the decomposition, the nucleation occurs through a one dimensional nucleation and is followed by subsequent grain growth processes. However, from the TEM image in Fig. 3.19, it seems a three dimensional process. This divergence in the results of the different experimental techniques can be explained by the decomposition of the amorphous phase. In this case, the coexistence of different amorphous regions with different composition may decrease the free Gibbs energy of the initial amorphous state. Consequently, when the decomposition takes place, the material releases some heat which contributes to the enthalpy of the first crystallization event. Furthermore, in the JMAK model it is assumed that the nucleation rate and growth rate of the nuclei does not depend on the local microstructure, whereas in the case of decomposition it does. So, the transformed volume fraction could be explained as a combination of two processes, decomposition of the amorphous matrix plus nanocrystallization of a crystalline phase.

For all the studied compositions the apparent activation energy for the first crystallization process is similar, see Table 3.III. Furthermore, the microstructure shown in X-ray after first crystallization stage is also comparable for all the compositions, see Fig. 3.14.

Both experimental data indicate analogous processes for each composition during the first crystallization peak and therefore, for all compositions Ti diffusion occurs, leading to a decomposition of the amorphous phase in two different amorphous regions.

For the alloys x=20 up to x=30, during the second crystallization stage hexagonal Cu_2TiZr nucleates and grows, while hexagonal $Cu_{51}Zr_{14}$ continues to grow. Moreover, cell parameters of hexagonal $Cu_{51}Zr_{14}$ remains more or less constant, while for hexagonal Cu_2TiZr increase with Zr composition, probably due to the substitution of Zr for Ti in the cell. No information on its solubility limits is available in the literature. However, in the case of x = 15, only hexagonal $Cu_{51}Zr_{14}$ grows during second crystallization stage, while tetragonal $CuTi_2$ nucleates and grows during third crystallization stage.

The final microstructure obtained in all the alloys agrees with the equilibrium phase diagram of Cu-Ti-Zr [58]. The formation of only two phases was also found by Woychik and Massalski [69], without a satisfactory explanation. The reason could be again the decomposition of the liquid in Cu and Ti rich zones. While Cu rich zones undergo a crystallization of hexagonal $Cu_{51}Zr_{14}$, in Ti rich zones hexagonal Cu_2TiZr-like is the crystallized phase.

3.2.5. Mechanical properties of $Cu_{60}Zr_xTi_{40-x}$ metallic glasses

The mechanical properties of $Cu_{60}Zr_xTi_{40-x}$ amorphous alloys (x = 20, 22, 25, 30) prepared by Cu-mould casting have been studied by means of compression tests. All the compositions exhibit high and similar yield and ultimate compression stress. However, all of them show poor plastic deformation although some differences have been found depending on the composition. These differences are discussed as a function of the ratio between the shear (μ) and bulk (B) modulus, since a recent compilation of data showed a universal and sharp correlation between μ/B and fracture toughness (G) for metallic glasses [70]. In this approach, the competition between flow and fracture relates the resistance to plastic deformation, proportional to μ, to the resistance to dilatation that occurs in the region of a crack tip, which is proportional to B.

3.2.5.1. Compression tests of $Cu_{60}Zr_xTi_{40-x}$ metallic glasses

Figure 3.25 shows the dependence of stress on strain during compression tests for the different studied compositions. To facilitate comparison the starting points of the curves are displaced. Furthermore, the strain at yield (ε_e), yield stress (σ_Y), maximum strain (ε_{US}), ultimate stress (σ_{US}), elastic modulus (E) and fracture plane inclination angles (θ) for the different studied glassy alloys are shown in Table 3.VI. All the compositions show a high ultimate stress around 2000 MPa, and a similar Young modulus around 110 GPa. Nevertheless, for x = 20-25 few per cent of the total strain corresponds to plastic strain, while for x = 30, the plastic strain is considerably larger (i.e. 1.3%). Similar results were obtained by Inoue et al. [40].

composition	ε_e (%)	σ_Y (MPa)	ε_{US} (%)	σ_{US} (MPa)	E (GPa)	θ (°)
$Cu_{60}Zr_{20}Ti_{20}$	1.5 ± 0.1	1600 ± 100	1.95 ± 0.1	2000 ± 50	118 ± 1	43 ± 1
$Cu_{60}Zr_{22}Ti_{18}$	1.5 ± 0.1	1600 ± 100	1.88 ± 0.1	1925 ± 50	112 ± 1	41 ± 1
$Cu_{60}Zr_{25}Ti_{15}$	1.6 ± 0.1	1600 ± 100	1.97 ± 0.1	1920 ± 50	104 ± 1	42 ± 1
$Cu_{60}Zr_{30}Ti_{10}$	1.5 ± 0.1	1600 ± 100	2.80 ± 0.1	2020 ± 50	115 ± 1	40 ± 1

Table 3.VI. Strain at yield stress (ε_e), yield stress (σ_Y), maximum strain (ε_{US}), ultimate stress (σ_{US}), elastic modulus(E) and fracture plane inclination angles (θ) for the different investigated glassy alloys.

Plastic flow in metallic glasses is thought to be a diffusion-like process involving the stress-induced cooperative rearrangement of small groups of atoms referred to as shear transformation zones [17,32]. These flow defects are associated to free volume sites, which are distributed throughout the structure. Thus, it is usually assumed that the amount and distribution of the free volume controls plastic flow. Furthermore, extensive plastic deformation is possible when multiple shear bands are generated [17,32].

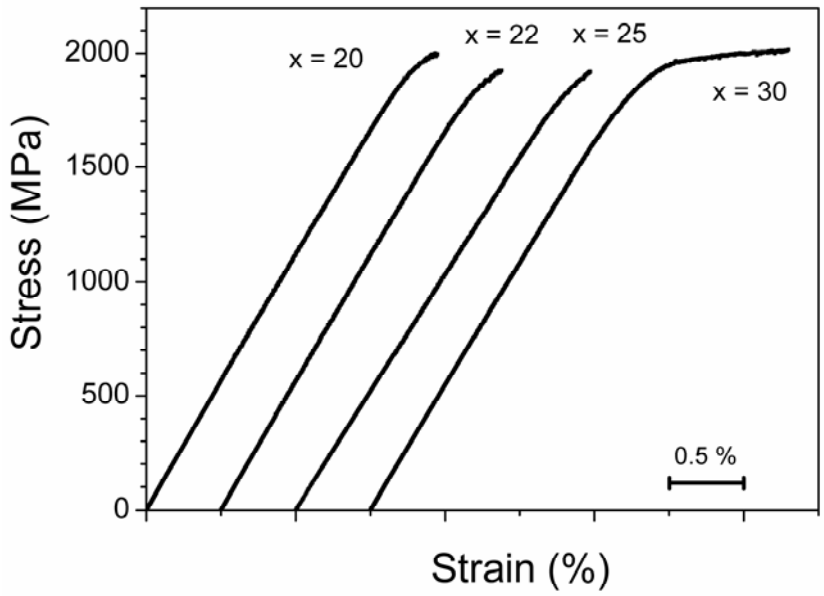

Figure 3.25. Uniaxial compressive stress-strain curve measured for $Cu_{60}Zr_xTi_{40-x}$ amorphous alloys. Starting points of the curves are displaced.

During uniaxial compression test, metallic glasses load elastically to the yield stress, at which point serrated plastic flow begins. Serrated flow is characterized by repeating cycles of a sudden stress drop followed by elastic reloading [71]. Since the plastic deformation achieved by bulk amorphous alloys is confined almost entirely in narrow regions near the shear bands, the extent of plastic deformation in the bulk amorphous alloy is largely dependent on the density of the shear bands. Therefore, it was expected that the different alloys would differ in their number density and the shape of their shear bands. In fact, detailed observation of the plastic strain in the stress-strain curve of each alloy show serrated flow during deformation, each burst is related

to the formation and propagation of shear bands, Fig. 3.26. The alloy with x = 30 shows more bursts than the other alloys.

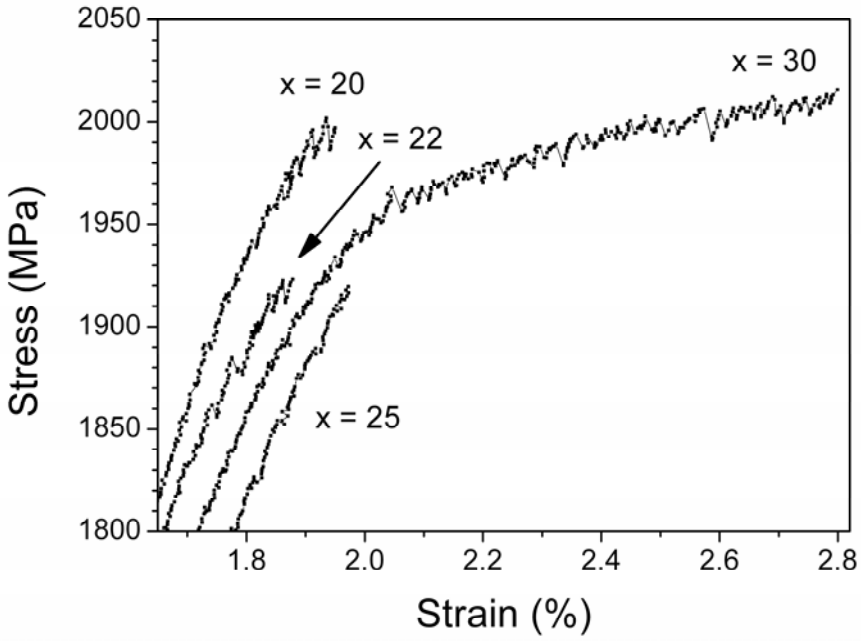

Figure 3.26. Stress as a function of strain in serrated flow region in the $Cu_{60}Zr_xTi_{40-x}$ tested in uniaxial compression.

According to Lewandowski et al. [70], metallic glasses show a brittle behaviour for certain ratios of shear modulus, μ, to bulk modulus, B, precisely for $(\mu/B) > 0.41\text{-}0.43$ or equivalently for a Poisson ratio, $\upsilon < 0.31\text{-}0.32$. The υ is related to μ/B by:

$$\upsilon = \frac{1 - 2\mu/3B}{2 + 2\mu/3B} \qquad \text{eq. 3.7}$$

In basis of this correlation, Yang and Greer have presented a formula to predict plasticity or brittleness of metallic glasses [72]. Their calculations are based on the property of a glass being an average of the constituent elements. Therefore, they used an average of the previous moduli weighted by volume fraction and, applying a uniform-strain model it is possible to calculate the shear modulus and bulk modulus of a metallic glass alloy according to

$$\overline{X}_c = \sum_{i=1}^{n} \frac{X_i c_i V_i}{\overline{V}_m} \qquad \text{eq. 3.8}$$

where: X_i, c_i and V_i are the modulus (μ or B), atomic fraction and volume per atom for the i-th constituent element, respectively; $\overline{V}_m$ and $\overline{X}_c$ are the measured average atomic volume and the calculated modulus of the metallic glass. But an assumption of uniform stress rather than strain, gives a lower bound for the calculated modulus

$$\overline{X}_c = \left(\sum_{i=1}^{n} \frac{c_i V_i}{X_i \overline{V}_m} \right)^{-1} \qquad \text{eq. 3.9}$$

From the mean of eqs. 3.8 and 3.9, a ratio between shear modulus and bulk modulus may be obtained. However, Zhang and Greer realized that it was necessary to scale it in order to predict the intrinsic plasticity or brittleness of the alloy. They obtained a scaled value to be

$$\left(\frac{\mu}{B}\right)_{sc} = \frac{0.78\mu_c}{B_c} \qquad \text{eq. 3.10}$$

In basis of the calculation of Zhang and Greer, the $(\mu/B)_{sc}$ of the studied compositions have been evaluated in order to predict their plasticity, obtaining the values quoted in Table 3.VII.

The lower ratio of shear modulus to bulk modulus of Zr than Ti makes the alloy with x = 30 to become the alloy with lower $(\mu/B)_{sc}$. In agreement with this result, the plasticity of the alloy x = 30 is higher than the rest, see Fig. 3.26. Furthermore, Egami has recently shed light in the brittle-plastic behaviour of metallic glasses and its relation with the ratio of shear to bulk modulus or Poisson's ratio [73]. The relation is in fact easy to understand if we assume that the local heating within the shear band is enough to make the temperature in the band exceeding the glass transition temperature [74]. In the system with a high Poisson's ratio or low ratio of shear to bulk modulus, the viscosity of liquid will quickly decrease, showing a fragile behaviour of the liquid [73]. This will allow stress concentration in the shear band to dissipate quickly, slowing down the propagation of the shear band, resulting in a ductile behaviour. On the other hand if the Poisson's ratio is low, the liquid will be strong and the viscosity will remain high, not allowing the stress concentration to dissipate, resulting in a brittle fracture. According to this reasoning, it has been observed that the alloy with x = 30 the viscosity decreases at higher rate and to a lower value at the glass transition temperature than the alloy with x = 20, see Fig. 3.12. However, the alloys with x = 22 and 25 behave as a more brittle materials than the alloy with x = 20 in spite of the higher amount of Zr. The possible explanation might be the difference in the atomic volume of the constituents, leading to a higher (μ/B) than the calculated $(\mu/B)_{sc}$.

Composition	$(\mu/B)_{sc}$
$Cu_{60}Zr_{20}Ti_{20}$	0.290
$Cu_{60}Zr_{22}Ti_{18}$	0.289
$Cu_{60}Zr_{25}Ti_{15}$	0.288
$Cu_{60}Zr_{30}Ti_{10}$	0.286

Table 3.VII. Calculated scaled ratio of shear modulus, μ, to bulk modulus, B, according to eqs. 3.8 to 3.10.

3.2.5.2. Fracture surfaces of $Cu_{60}Zr_xTi_{40-x}$ metallic glasses

So far several studies on uniaxial tension [7,75-78], compression [75,76,78-82], three point bending [83-85], fracture toughness [86,87] and fatigue [88,89] were reported in order to

reveal the mechanisms of strain localization, plastic deformation, crack initiation and propagation in metallic glasses. In these previous works, different features on the fracture surfaces were observed depending on the fracture mode. Mainly, three different distinct patterns were described: vein-like, smooth featureless and river-like features. The first one has been reported several times in compression tests, while the smooth featureless has been attributed to fast crack propagation and the last one corresponds to the morphology known from tensile tests of BMGs.

In the present section, we report on the different fracture features developed during compression of Cu-based BMG. The quasi-static compression fracture surface displays a mixture of the three mentioned patterns and randomly distributed transversal steps on the fracture plane. The presence of these different fracture features indicates that the development of the fracture plane occurs in a stepwise mode.

The as-cast samples studied fractured along a single plane, indicating that one major shear-band dominates the final fracture. The inclination fracture angle in compression for each studied alloy are quoted in Table 3.VI, and are lower than 45º, indicating that plasticity in the present BMG deviates from the classical von Mises yield criterion, as usual in metallic glasses, see section 1.1.7.2.

The SEM image of the $Cu_{60}Zr_{30}Ti_{10}$ presented in Fig. 3.27 shows the fracture surface covered mostly with a vein-like pattern. Similar fracture morphology was observed for other metallic glasses with different chemical compositions [7,75,76,78-82]. This type of pattern is generally considered to be typical for the compression fracture of BMGs. The uniform arrangement of the veins agrees with the flow direction in the shear plane, as already pointed out by Zhang et al. [75].

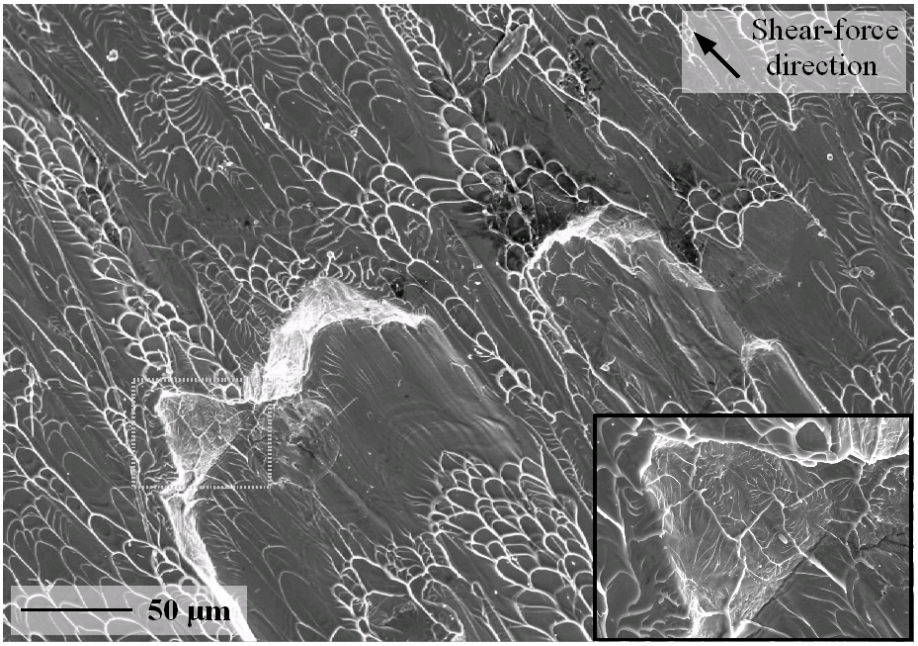

Figure 3.27. Transversal step and fracture morphology of neighboring regions formed on fracture surface of $Cu_{60}Zr_{30}Ti_{10}$ upon compression. Inset shows enlargement of the transversal step with the river-like morphology.

However, other distinct fracture patterns have been observed at higher magnification. A river-like morphology is found on the fracture plane of all studied alloys, as exemplified in the inset of Fig. 3.27. This morphology appears in the form of islands surrounded by vein-like patterns and intermittent smooth regions that sometimes contain fine striations (Fig. 3.27). Similar fracture surface features were found for the $Cu_{60}Zr_{20}Ti_{20}$ (see Fig. 3.28). Both figures reveal areas where transversal steps are emerging from the main fracture plane, presenting the localized formation of a river-like pattern (see inset of Fig. 3.27). An analogous morphology has been recently found by Xi et al. [90] on the fracture surface of a brittle Mg-based BMG.

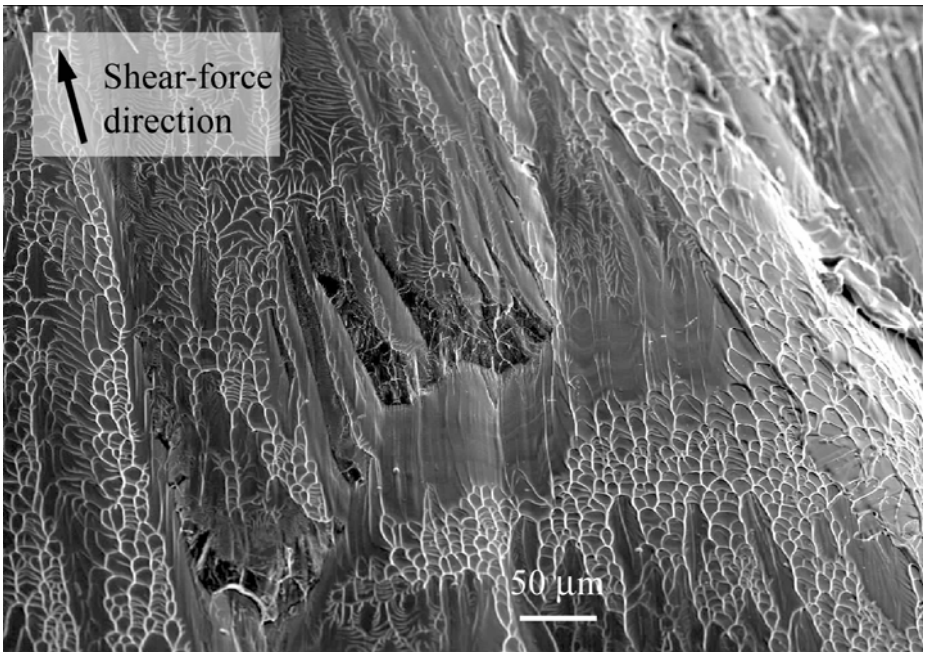

Figure 3.28. Fractography of $Cu_{60}Zr_{20}Ti_{20}$. Overview of the fracture surface with regions of different morphology; with transversal step and mixed fracture morphology – vein-like pattern, river-like pattern and intermittent smooth regions.

Note that, when following the direction opposite to the direction of the shear force, there is no visible distinct boundary for the transition from the river-like pattern to the intermittent smooth regions and to the vein-like pattern. However, there is a sharp discontinuity between the vein-like and the river-like patterns in form of a transversal step on the fracture surface, as exemplified in Fig. 3.27 for $Cu_{60}Zr_{30}Ti_{10}$ and in Fig. 3.28 for $Cu_{60}Zr_{20}Ti_{20}$. Transversal steps of different sizes ranging from a few micrometers up to hundreds of micrometers were found. It is noteworthy that the river-like fracture pattern formed on the transversal steps resembles the pattern observed on the fracture surface after tensile testing [75,76,78]. Furthermore, it is well-known that when two parallel flat glass surfaces with a thin layer of silicone in between are separated (like in a tensile test experiment), a river-like pattern is formed on the two surfaces.

The presence of different morphologies on the fracture surface may help to interpret the conditions as well as the time sequence of their formation during compression.

As it is mentioned above, the fracture surface analysis of the Cu-based BMGs reveals three distinct morphologies: (a) vein-like pattern, (b) intermittent smooth regions and (c) river-like pattern. According to the literature, a high temperature is achieved in the shear bands, [74], due to local heating (well above the glass transition temperatures), and when the fracture occurs the vein-like pattern is formed on the fracture surface. This morphology covers most of the fracture surface area of the studied alloys.

Besides the dominant vein-like morphology, some intermittent smooth regions are also observed on the examined fracture surfaces. According to Conner et al., these smooth regions were formed during fast crack propagation when the crack tip recovered from a trap of a crystalline particle in a $Zr_{57}Nb_5Al_{10}Cu_{15.4}Ni_{12.6}$ metallic glass reinforced with W particles [91]. After the particle was sheared due to the high energy accumulated in the elastic-plastic zone of the crack tip, the crack propagates through the glassy matrix forming a smooth region. Subhash et al. [92] used the proposed model of the intermittent smooth region formation to explain a similar feature observed on the fracture plane of a BMG deformed at high strain rate. Both studies confirmed the essential role of fast crack propagation. Therefore, local conditions similar to high rate crack propagation might be established in the regions where intermittent smooth regions are observed, generally near the transversal steps.

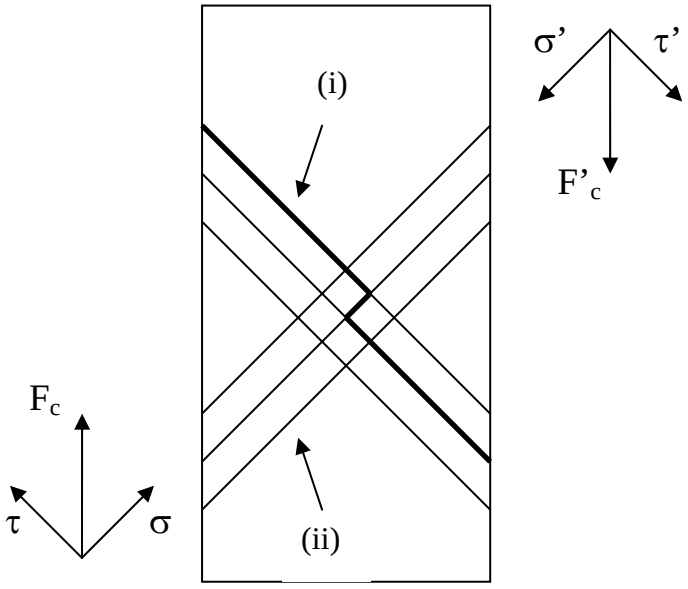

Figure 3.29. Schematic representation of a compression test on a BMG. (i) and (ii) represent the primary and secondary shear bands, respectively, formed during compression test. σ and τ are the resolved normal and shear stress components of the compression force F_C, respectively.

The river-like pattern is the third distinct morphology found randomly scattered over the fracture surface, frequently covering areas near the edge of the fracture plane. This morphology

is a region where fine tributaries merging into coarser rivers are present on the fracture surface. The orientation of the tributaries reflects the imposed local stress and their onset points correspond to the nucleation site of a crack [93]. Merging sets of rivers originating from neighboring flaws are observed to form loops, as it has already been reported [75,76] (see the inset in Fig. 3.27). The nucleation centers of the river-like morphology are located either randomly on a transversal plane or near the intersection of the shear plane with transversal steps.

The morphology of the river-like pattern formed on the transversal steps is very similar to that observed for BMGs fractured in tension [75,76]. However, the presence of local tensile stresses acting on the main fracture plane is not obvious during compression. In order to understand the role of the shear-bands in the formation of transversal steps, the resolved components of the superimposed compression force are overlapped with an array of shear bands or a transversal step penetrating onto the surface of the compression test specimen, as shown in Fig. 3.29. According to Kusy et al. [93], the shear bands can be divided into two distinct groups; (i) shear-bands aligned parallel with the fracture plane (plane i) – primary shear bands, (ii) shear bands approximately perpendicular to the fracture plane (plane ii) – secondary shear-bands, see Fig. 3.29.

It should be considered that the crack nucleation and subsequent crack growth at the shear bands of group ii (secondary shear bands) and group i (primary shear bands) leading to failure are competing, since they have exactly the same stress magnitude. Basically, the secondary shear bands (ii) act as bridging ligaments between a set of parallel primary shear bands. Such physical separation is very similar to the failure under pure normal stress. This, in turn, helps to develop a core structure and a river-like pattern close to the plane ii and forms transversal steps on the fracture plane, as it is clearly evidenced in Figs. 3.27 and 3.28. In contrast, final failure along a shear plane causes the formation of melting features on the fracture surface leading to a vein-like pattern.

In summary, the obtained results show that the fracture surfaces of the studied alloys present the same motives of fracture morphology: a vein-like pattern, intermittent smooth regions and a river-like pattern. The river-like patterns as well as the intermittent smooth regions cover isolated regions of the fracture surface surrounded by a dominating vein-like pattern. The river-like pattern formed on transversal steps resembles morphology similar to the one observed on the fracture planes of samples loaded in tension. Easy separation along the secondary shear bands takes place at the instability prior to failure due to the significant strain accommodated along perpendicular and parallel direction with respect to the shear band planes during the compression test.

Possibly sub-critical crack nucleation starts from sites covered with the river-like pattern. The crack propagation further continues forming the intermittent smooth regions. The vein-like pattern develops during the ultimate failure of the compression specimens in the regions of the softened shear bands.

3.3. Effect of relaxation and primary nanocrystallization on the mechanical properties of $Cu_{60}Zr_{22}Ti_{18}$ bulk metallic glass

As it has been shown in the previous section, Cu-base BMGs display little plastic deformation at room temperature because the plastic flow is governed by the formation of localized shear-bands. The precipitation of ductile or nanoscale crystalline phases may be used to improve the mechanical behaviour of BMGs, [94-96], since nanocrystals may disrupt shear-band propagation, as shown in section 1.2. The precipitation of nanocrystals in the amorphous matrix may be induced by the addition of elements which cause partial crystallization during casting, [95], or by primary crystallization during heat treatment of the BMG. However, the formation of brittle intermetallic compounds may strongly degrade the toughness and the plasticity of the material. The grain size and volume fraction of the precipitated intermetallic phases are important parameters to control, since when certain critical values are exceeded the material may become brittle.

Despite the high compressive strength, Young's Modulus around 100-115 GPa, and an elastic elongation of about 2.0% in the as-cast state for the Cu-Zr-Ti presented alloys, few efforts have been made to investigate the effect of the addition of nanocrystalline precipitates in the amorphous matrix, either by element addition, [45], or by primary crystallization. As it has been stated in section 3.2.1, the $Cu_{60}Zr_xTi_{40-x}$ amorphous system showed for x = 22 the widest supercooled liquid region and the highest glass forming ability. Therefore, the dependence of the microscopic and macroscopic mechanical response of a $Cu_{60}Zr_{22}Ti_{18}$ BMG on the degree of thermal relaxation and different crystalline volume fractions are presented. As it is shown, macroscopic compression tests reveal that the fracture strength and Young's modulus increase with increasing annealing time and hence, with increasing crystalline volume fraction. However, embrittlement of the material is also found for longer annealing treatments. In the forthcoming section we will show that a perfect solute mixture model of defect-free nanoparticles embedded in an amorphous matrix can be used to account for the strengthening effect. Nanomechanical tests will also contribute to the understanding of the mechanical behaviour of the heat treated BMG states under investigation.

3.3.1. Thermal treatments in the $Cu_{60}Zr_{22}Ti_{18}$ BMG

The amorphous nature of the alloys was confirmed by X-ray diffraction (XRD) and differential scanning calorimetry (DSC) as described above, in section 3.2.1. Relaxed state was produced by heating the sample up to 698 K ($T_{ann} \sim T_g$) at a heating rate of 0.33 K s^{-1} and subsequent cooling. Isothermal heat treatments were carried out for different times in a Linn oven by heating the sample up to 698 K ($T_{ann} \sim T_g$).

The typical DSC curve of the as-cast specimen shows two exothermic peaks corresponding to the crystallization of the amorphous material. It has been shown that in the case of $Cu_{60}Zr_xTi_{40-x}$ (x = 15, 20, 22, 25, 30) alloys, decomposition in two different amorphous regions plus precipitation of nanocrystals of $Cu_{51}Zr_{14}$ occurs during the first crystallization peak, although no Bragg peaks of the crystallized phase were observed in the conventional XRD pattern, as shown in section 3.2.1. Furthermore, after the completion of the first crystallization peak nanocrystals of 4-5 nm embedded in an amorphous matrix were observed in x = 20 and x = 30, shown in section 3.2.3 and [44,97].

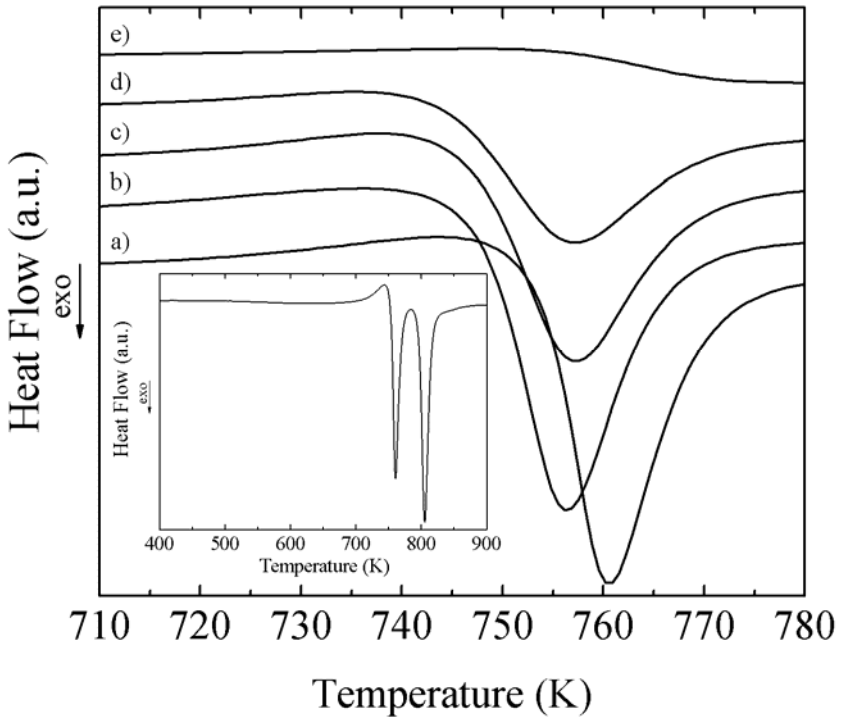

Figure 3.30. First DSC peak (heating rate of 0.667 K s^{-1}) of the $Cu_{60}Zr_{22}Ti_{18}$ specimens a) as-cast, b) relaxed, and after isothermal annealing at 698 K holding the temperature for c) 15 min, d) 30 min and e) 120 min, of a continuous heating at 0.667 K s^{-1}. The inset shows the complete DSC-curves of the as-cast $Cu_{60}Zr_{22}Ti_{18}$ specimens recorded at the same heating rate.

	As-cast	Thermally relaxed	T_{ann} hold 5 min	T_{ann} hold 10 min	T_{ann} hold 30 min	T_{ann} hold 120 min
V_{crys}	0	0	0.058	0.075	0.181	0.403
E (GPa)	106 ± 7	115 ± 8	130 ± 9	137 ± 10	139 ± 10	142 ± 10
σ_{US} (MPa)	1925 ± 193	2045 ± 205	2050 ± 205	2075 ± 208	2100 ± 210	2200 ± 220
ε_{US} (%)	1.9 ± 0.2	2.0 ± 0.2	1.7 ± 0.2	1.7 ± 0.2	1.6 ± 0.2	1.5 ± 0.2

Table 3.VIII. Crystallized volume fraction, V_{crys}, Young modulus, E, ultimate fracture stress, σ_{US}, and ultimate fracture strain, ε_{US}, for the as-cast and thermally treated samples, where T_{ann} = 698 K.

Figure 3.30 shows the first DSC peak obtained at 0.667 Ks^{-1} for the as-cast and the heat-treated samples. Curve a) corresponds to the fully amorphous state. After thermal relaxation the first peak shifts to lower temperature without variation in the peak enthalpy (curve b) Fig. 3.30). Furthermore, we were unable to detect incipient crystallization using experimental means available. The displacement of the first crystallization peak after relaxation may be due to a rearrangement in the atomic short range order, such as initial decomposition of the amorphous phase [97]. A subsequent increase of the duration of the annealing at 698 K leads to a reduction of the enthalpy of the first DSC peak, as shown in Fig. 3.30, indicating a primary crystallization of $Cu_{51}Zr_{14}$ from the amorphous matrix [97]. However, the enthalpy measured in the second crystallization peak remains unaltered. This indicates that no formation of the second crystalline phase, Cu_2TiZr, has taken place during the thermal treatments. From the enthalpies released during the first crystallization peak, the total crystallized volume fraction, V_{crys}, for each specimen was calculated by methods previously outlined [41], and presented in Table 3.VIII.

3.3.2. Fracture behaviour of relaxed and nanocomposite $Cu_{60}Zr_{22}Ti_{18}$

The results obtained from the compression tests are shown in Table 3.VIII. Both structural relaxation and $Cu_{51}Zr_{14}$ precipitation produce an increase in Young's modulus and fracture strength, while the ultimate strain slightly increases once the sample relaxation takes place and decreases with the increasing volume fraction of $Cu_{51}Zr_{14}$ formed. As noticeable in Fig. 3.31, the structural relaxation produces an increase in the maximum strength before failure reached during the elastic deformation, linear part of curve b), maintaining the plastic flow in a similar range. Subsequent formation of $Cu_{51}Zr_{14}$ nanocrystals leads to a reduction in plastic deformation and a tendency for catastrophic failure as a consequence of the increasing crystalline volume fraction. The combination of these two behaviours explains the increase in ultimate strain for the relaxed specimen and its decrease with increasing amount of nanocrystals.

The fracture surfaces of the compression test specimens were examined in order to understand the fracture behaviour dependence on the crystallized volume fraction (Fig. 3.32). The as-cast sample fractured along a single plane, indicating that one major shear-band dominates the final fracture. The inclination angle in compression is around 40.8°, which indicates that plasticity in the present BMG deviates from the classical von Mises yield criterion, as usual in metallic glasses [76]. The fracture surface of the as-cast sample shows the typical vein-like structure already found in different metallic glasses (Fig. 3.32 a). This vein-like structure is attributed to local softening by melting of some regions of the alloy within the shear-band, induced by the high elastic energy release upon instantaneous fracture [74,79].

The relaxed sample did not fracture along a single plane since the fracture surface was relatively rough. This result may be due to simultaneous operation of multiple shear bands. Despite the different fracture surface of the relaxed and the as-cast specimens, and the different fracture mode, a similar vein-like structure was observed in both specimens. While as-cast samples fractured in two pieces, relaxed and partially crystallized samples fractured to several

pieces, showing a reduction in size and an increase in the number of the pieces with increasing crystallized volume fraction, hence, the material becomes brittle for longer annealing times.

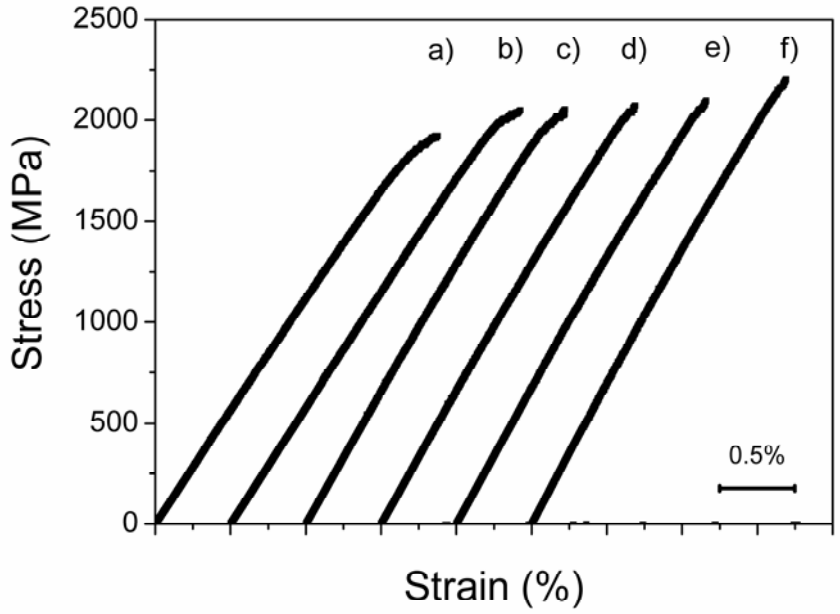

Figure 3.31. Compression test curves of the $Cu_{60}Zr_{22}Ti_{18}$ specimens a) as-cast, b) relaxed, and after isothermal annealing at T_{ann} = 698 K for c) 5 min, d) 10 min, e) 30 min and f) 120 min. The curves have been displaced by 0.5% in strain.

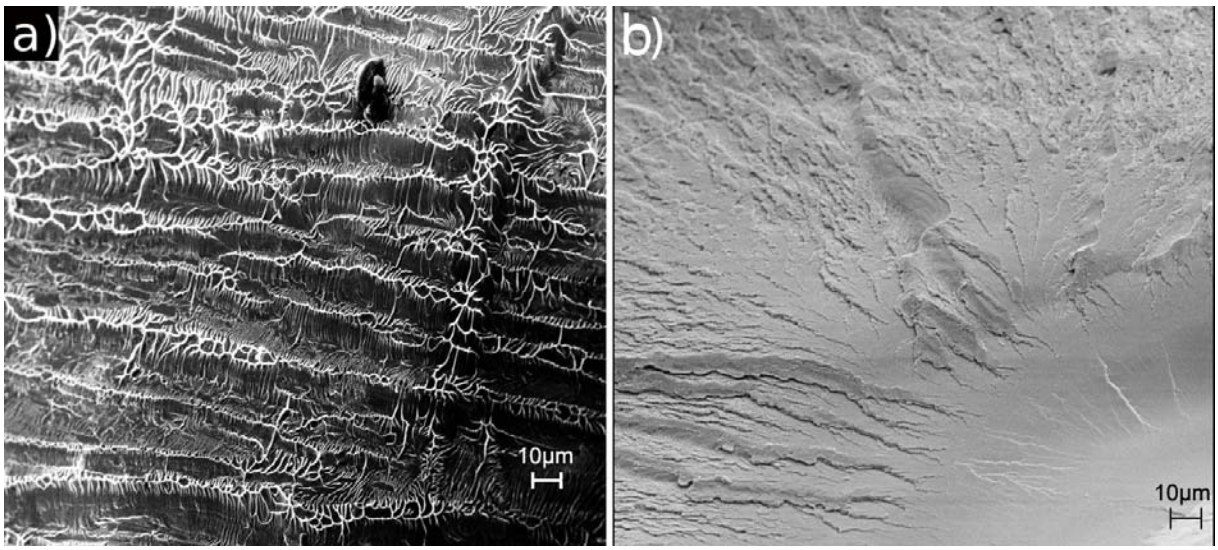

Figure 3.32. Fracture surfaces of the $Cu_{60}Zr_{22}Ti_{18}$ specimens for the a) as-cast state, and b) after isothermal annealing at T_{ann} = 698 K for 10min.

Figure 3.32 b) shows the fracture surface of a sample heat treated for 10 min. The propagation of the fracture starts with a few vein patterns, (right-hand bottom corner of Fig. 3.32 b), and continues to a zone in which cracks and microvoids have formed. The observed

fracture surface reveals that during compressive loading micro-cracks join together to form continuous cracks, leading finally to brittle fracture. This response together with the compression test result implies that the ability of the amorphous matrix to deform plastically decreases with increasing volume fraction of crystalline precipitates. Longer annealing result in similar features on the fracture surface, and the material fractures into multiple pieces, larger in number for longer annealing times.

3.3.3. Nanoindentation results on relaxed and nanocomposite $Cu_{60}Zr_{22}Ti_{18}$

The deformation behaviour of the alloy under investigation was also analysed by nanoindentation. Figure 3.33 shows load-displacement curves for each of three different thermally treated specimens. The curves have been displaced 20 nm from each other to facilitate comparison. During the loading segment, all the curves exhibit a very similar displacement at 5 mN load (inset of Fig. 3.33). Increasing the load to 8 mN produces a different displacement in each of the three materials, showing a clear trend in final indentation depth as a function of the volume fraction of crystalline $Cu_{51}Zr_{14}$, although this variation is small. Additionally, the slope of the unloading part of the curves, which is related to elastic recovery of the materials, is clearly higher for the relaxed specimen and lower for the other two (the values for the two partially crystallised samples are comparable). It is also worth mentioning that some small pop-in events, attributed to shear-band formation, are distributed randomly along the loading segment of the curves in all the samples [28]. Furthermore, these pop-in events become more visible with the relaxation degree of the amorphous matrix.

3.3.4. Correlation between compression and nanoindentation results

The features on the fracture surface of as-cast alloy, such as viscous flow traces, vein pattern morphology, and localized melting, reveals typical deformation behaviour of amorphous alloys and corresponds to a slightly ductile fracture mode [7,92].

Structural relaxation of the amorphous alloy produces a small increase in the Young's modulus and fracture strength of the material with respect to the as-cast sample, similar results were also found by Mulder et al. in a $Fe_{32}Ni_{36}Cr_{14}P_{12}B_6$ metallic glass [98]. During structural relaxation, a more dense randomly packed structure is obtained due to the annihilation of free-volume, and hence, the elastic atomic rearrangements which takes place during the compression test are more difficult [98,99], leading to the increase in Young’s modulus. Embrittlement (i.e. reduction in the plastic fracture strain) is generally observed in BMGs after relaxation [98-101]. This is indeed the case here, but the reduction in plastic strain failure is very small for the relaxed sample and can only be observed for the samples annealed for longer times (Fig. 3.31). According to the Wu and Spaepen phenomenological free-volume flow model, a critical minimum amount of free-volume is required for significant plastic deformation [102]. In the

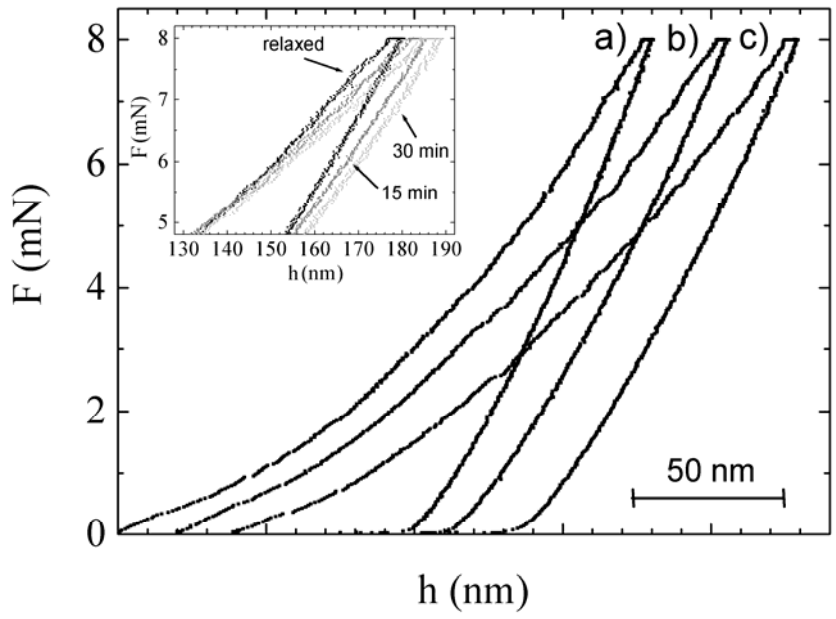

Figure 3.33. Load-displacement curves of the $Cu_{60}Zr_{22}Ti_{18}$ specimens a) relaxed, and after isothermal annealing at T_{ann} = 698 K for b) 15 min and c) 30 min, measured during nanoindentation tests at 1.6 mN/s. The inset shows a zoom of two load displacement curves (not displaced) between about 5 and 8 mN, for a relaxed, a 15 min and a 30 min annealed sample at T_{ann}= 698 K.

present case, the reduction of free-volume during relaxation treatment clearly has not caused a catastrophic embrittlement of the material, and shear-band formation may be still possible in the relaxed specimen. In fact, shear band formation and propagation is observed in the relaxed specimen by nanoindentation, see Fig. 3.33.

The fracture stress and Young's modulus of the material increase with increasing volume fraction of $Cu_{51}Zr_{14}$ although the plastic deformation decreases, as shown in Fig. 3.31 and described above. The increasing relaxation of the amorphous matrix and the precipitation of nanocrystals during annealing may therefore appreciably influence the deformation and fracture behaviour. The relaxation of the amorphous matrix dominates the deformation behaviour because crystallization kinetics of the alloy is known to be rather slow [97]. For this reason and because the small grain size of any precipitate is not conducive to the formation of dislocations, the main deformation mechanism of these materials should be shear-banding across the amorphous matrix. So, the embrittlement of the crystallized samples, since plastic deformation dramatically disappears with increasing annealing time, is attributed to the reduction of the free-volume in the amorphous matrix, and the formation of shear bands result in fracture without plastic deformation. This may be observed from the nanoindentation tests, which show steps in the loading curve corresponding to the shear-band propagation (Fig. 3.33), and these steps are more marked for longer annealing times. Furthermore, the nanocrystals formed during the annealing are not able to inhibit significantly shear-band propagation maybe due to their small size. Thus, catastrophic failure is still observed.

A phase mixture model [103,104] can be invoked to explain the increase of the fracture strength with the increasing volume fraction of precipitates. In this simple model the partially

crystallized alloy is considered as a nanocomposite consisting of defect-free nanoparticles embedded in the amorphous matrix. The rule of mixtures for the compressive strength, σ, of the different heat treated samples is represented by eq. 3.11,

$$\sigma = V_{relax}\sigma_{relax} + V_{Cu_{51}Zr_{14}}\sigma_{Cu_{51}Zr_{14}} \qquad \text{eq. 3.11}$$

where V_{relax} and σ_{relax} and $V_{Cu_{51}Zr_{14}}$ and $\sigma_{Cu_{51}Zr_{14}}$ are the volume fraction and the compressive strength of amorphous phase in the relaxed state and of the nanocrystalline particles, respectively. In order to calculate the fracture strength for the annealed states with the phase mixture model, fracture strength of the relaxed state is used, because the amorphous matrix undergoes a relaxation during heating to the isothermal annealing temperature and the main deformation mechanism is shear banding, as described above. The yield strength of $Cu_{51}Zr_{14}$ is used since no plastic deformation of the nanocrystals is expected, due to their small grain size. Taking into account that Vickers microhardness of $Cu_{51}Zr_{14}$ is around 6.7 GPa, and using the well-known relationship $H_V = 3\sigma_y$, [105], to approximate the yield strength of $Cu_{51}Zr_{14}$, the results for the fracture strength of the different treated samples using the phase mixture model are shown in Fig. 3.34. There is a rather satisfactory agreement between the experimental values and the modelled function.

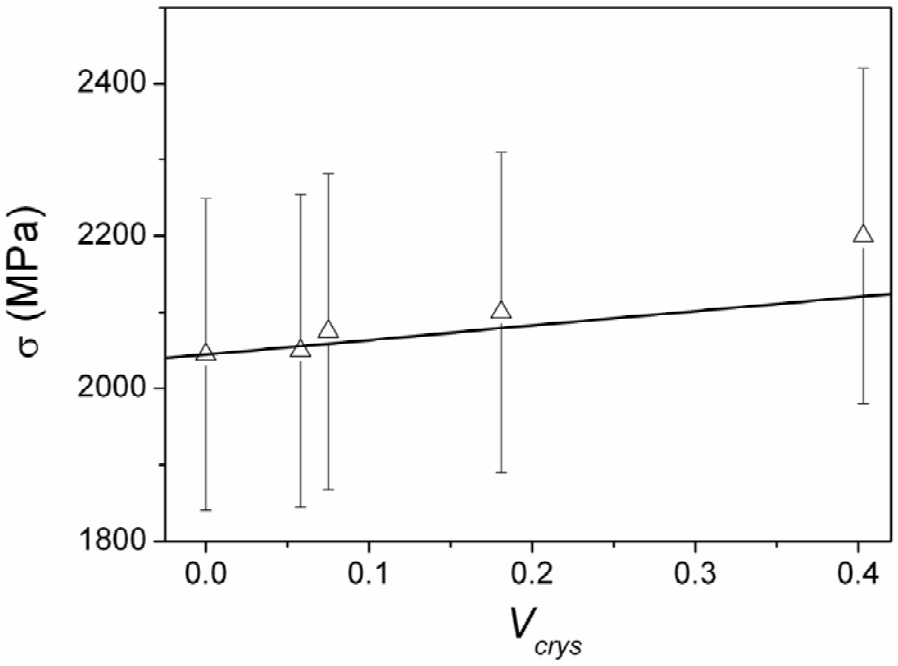

Figure 3.34. The fracture strength values, σ, versus the crystallized volume fraction, V_{crys}. △ corresponds to the experimental points. The straight line represents the theoretical fracture strength calculated by the phase mixture model.

Therefore, macroscopic compression tests revealed embrittlement of the material with increasing annealing time. The embrittlement of the annealed samples may be attributed to the reduction of the free-volume in the amorphous matrix during the annealing treatment, since a critical minimum amount of free-volume is necessary for sufficient plastic deformation

according to the model of Wu and Spaepen [102]. According to nanoindentation and macroscopic compression tests, the main deformation mechanism of these materials is shear-banding across the amorphous matrix. The nanocrystals formed during the annealing may not disrupt shear-band propagation due to their small size and this leads to catastrophic failure without plastic deformation in the nanocomposite. Fracture strength and Young's modulus increase with increasing crystalline volume fraction. A perfect solute mixture model of defect free nanoparticles embedded in an amorphous matrix has been applied satisfactorily to describe the strengthening mechanism.

3.4 Mechanical properties of a two-phase amorphous Ni-Nb-Y alloy studied by nanoindentation

Different mechanisms have been proposed to overcome the low ductility of metallic glasses such as precipitation of a second phase or fine dispersion of porosity [106-108]. Namely, the precipitation of a second phase in the amorphous matrix may disrupt shear-band propagation and hence improve the ductility of these materials at low temperature. Usually, ductile or nanoscale crystalline phase(s) are used for this purpose [106,108]. However, recent studies have succeeded in obtaining metallic glasses with heterogeneous two-phase amorphous structures [109-114]. A particular case is the Ni-Nb-Y alloy, which is composed of two binary amorphous phases due to the immiscibility gap of the Y-Nb system in the liquid as well as in the solid states due to the strong positive enthalpy of mixing. It is noteworthy that the studies on the mechanical behaviour of two-phase metallic glasses are very scarce and the few existing works only deal with systems in which one of the two phases composing the metallic glass is nanometric in size [113,114].

The purpose of the current section is to investigate the mechanical properties, by means of nanoindentation, of a two-phase amorphous Ni-Nb-Y alloy. A comparison with nanoindentation results on the corresponding single-phase amorphous alloys is made to provide valuable information for better understanding of the deformation mechanisms in the two-phase amorphous composite metallic glass.

Three master alloys with nominal compositions $Ni_{59.5}Nb_{40.5}$, $Ni_{57.5}Y_{42.5}$ and $Ni_{58.5}Nb_{20.25}Y_{21.25}$ (at%) were prepared by arc melting a mixture of the pure elements in an Ar atmosphere. Ribbons of each composition were obtained from the melt by means of rapid quenching. Nanoindentation were run in load-control mode at a constant loading rate of 0.25 mN s^{-1}, to a maximum force of 10 mN held during 30 s followed by unloading at a constant rate of 1.00 mN s^{-1}. The thermal drift was kept below ± 0.05 nm s^{-1} for all the indentations considered here. The hardness and the reduced elastic modulus (E_r) were derived from these load-displacement curves using the method of Oliver and Pharr [9].

3.4.1 Microstructure of the two-phase amorphous Ni-Nb-Y alloy

The XRD patterns of the two single-phase studied alloys (not shown) exhibit broad and symmetric halos, typical of fully amorphous phases. In the case of the two-phase alloy, the spectrum is a superposition of the patterns of the different individual phases [111]. The microstructure of the ternary alloy shows decomposition into two phases (see Fig. 3.35). Energy dispersive X-ray analysis (EDX) reveals that the bright amorphous matrix is enriched in Y, while the globular darker regions are rich in Nb [111]. From the HRTEM images, it is interesting to note that the inter-phase boundary is rather sharp due to the large immiscibility

gap of the Nb-Y system, similar results were found in other systems [109-114]. Furthermore, from an ensemble of different SEM images corresponding to the ternary alloy, the phase percentages of Y-rich matrix and Nb-rich globules have been determined to be 60 vol.% and 40 vol.%, respectively. Further details on the phases and microstructure of the alloy can be found in Ref. [111].

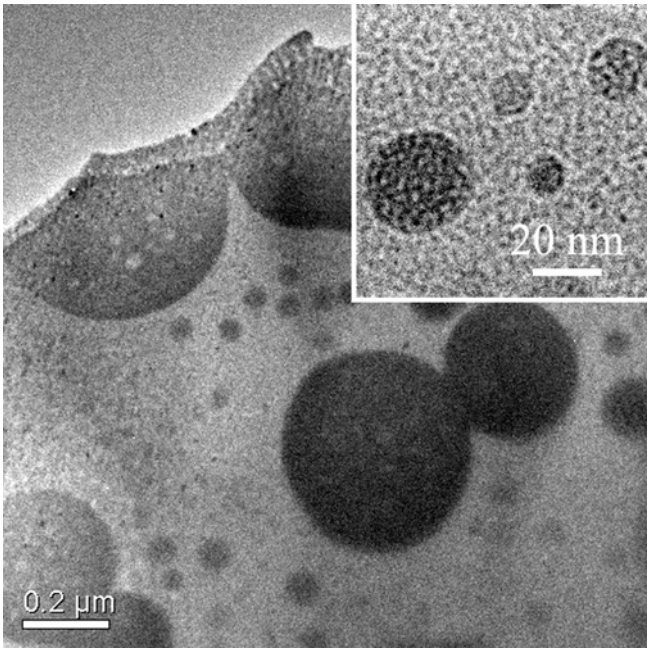

Figure 3.35. Transmission electron microscopy micrographs (cross section) of the rapidly-quenched $Ni_{58.5}Nb_{20.25}Y_{21.25}$ alloy. The inset shows a HRTEM image of the same alloy.

3.4.2 Mechanical properties of the two-phase amorphous Ni-Nb-Y alloy

The mechanical properties of composite materials are usually understood as being the result of a combination of the individual mechanical properties of each of the constituent phases [115]. The so-called rule of mixtures in isostrain conditions can be expressed as

$$P_c = \sum X_i P_i \qquad \text{eq. 3.12}$$

where P_c is the mechanical property of the composite, and P_i and X_i are the property and the volume fraction of the i^{th} composing phase, respectively.

Figure 3.36 shows load-displacement (*F*-*h*) nanoindentation curves for the studied metallic glasses. The hardness (*H*) and the reduced elastic modulus (E_r) values obtained for each composition are quoted in Table 3.IX. Also indicated in Table 3.IX are the *H* and E_r values for the $Ni_{58.5}Nb_{20.25}Y_{21.25}$ alloy calculated using eq. 3.12. Although the calculated E_r for the ternary alloy is similar to the measured value, the calculated hardness is larger than the measured one. Clear pop-in events or steps appear in the loading curve corresponding to the $Ni_{59.5}Nb_{40.5}$ alloy. Such discontinuities in the loading curve are related to shear bands, the characteristic feature of inhomogeneous plastic deformation in metallic glasses [16,116,117]. However, in the other two

loading curves, pop-in events are almost imperceptible. The apparent absence of serrations may be due to either lack of resolution of the system or a poor rate of data acquisition [118], since shear bands are indeed formed, in all the alloys, in the vicinity of each indentation, as it can be observed in the HRSEM images shown in Fig. 3.37.

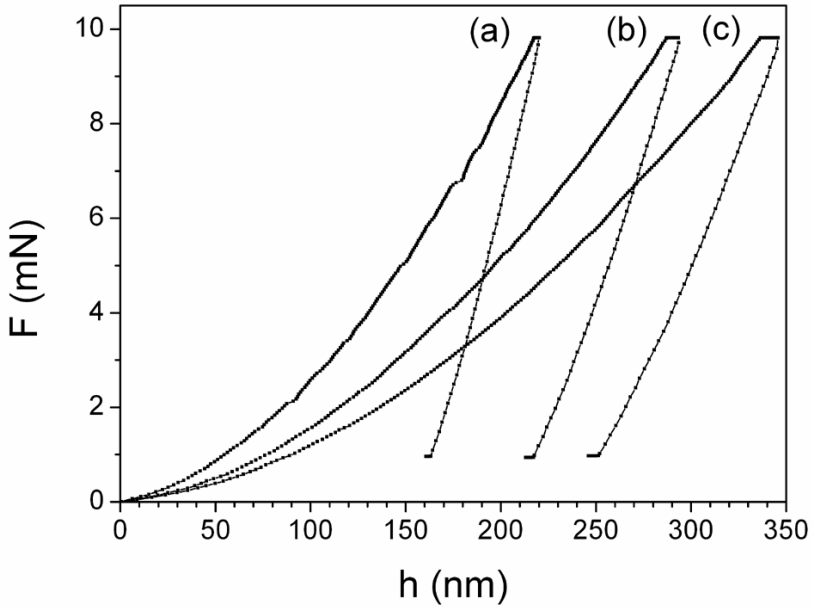

Figure 3.36. Load-displacement (F-h) curves measured during nanoindentation tests in load control mode for: (a) $Ni_{59.5}Nb_{40.5}$, (b) $Ni_{58.5}Nb_{20.25}Y_{21.25}$ and (c) $Ni_{57.5}Y_{42.5}$ amorphous alloys.

The apparent lack of serrated flow in the ternary alloy, similar to what is observed in $Ni_{57.5}Y_{42.5}$, may suggest that the plasticity of this alloy is dominated by the soft Y-rich matrix. Nevertheless, the reduced elastic modulus of the ternary alloy is equal to the calculated one using the rule of mixtures under isostrain conditions, indicating that the elastic properties of the $Ni_{58.5}Nb_{20.25}Y_{21.25}$ composite glass can be well described by this rule. This result implies that the two amorphous phases deform concomitantly under an elastic deformation, and therefore the boundary between the two compositionally different regions has almost no effect on the overall elastic behaviour. Actually, according to Hufnagel et al. [119], the elastic deformation in amorphous metals is confined to the nearest-neighbour atomic shell, although due to the amorphous structure of a metallic glass, not all atoms, even if they are of the same species, experience the same displacement in elastic deformation. In the two-phase alloy, the atomic

	$Ni_{59.5}Nb_{40.5}$	$Ni_{57.5}Y_{42.5}$	$Ni_{58.5}Nb_{20.25}Y_{21.25}$ Measured	$Ni_{58.5}Nb_{20.25}Y_{21.25}$ Calculated (40 % NiNb)
H (GPa)	11.5 ± 0.3	4.6 ± 0.2	6.5 ± 0.4	7.4 ± 0.3
E_r (GPa)	190 ± 8	58 ± 5	107 ± 3	111 ± 8

Table 3.IX. Hardness, H, and reduced elastic modulus, Er, for the different studied compositions. The last column corresponds to the calculation of the H and E_r for the $Ni_{58.5}Nb_{20.25}Y_{21.25}$ alloy using eq. 3.12.

distribution in the boundaries differs from the one in the Y-rich matrix and the Nb-rich globular phase. However, since the interfaces are very sharp (see Fig. 3.35) the percentage of atoms forming the boundaries is low. Hence, their contribution to the elastic modulus is very small. On the other hand, eq. 3.12 overestimates the hardness value of the composite (see Table 3.IX). This is not so surprising taking into account that this rule is not fully applicable for the morphology of the composite material investigated in this work. Namely, in our case, the system consists of a discontinuous composite in which the reinforcement is hard and more rigid than the matrix while the morphology for which it might be more reasonable to use eq. 3.12 is one with a percolating hard and rigid phase (for example in lamellae loaded in parallel or a discontinuous composite with a reinforcement softer than the matrix). Nevertheless, the indentation strain field once the load is released might almost lead to isostrain conditions in the material and this may account for the relatively good agreement between the calculated and measured reduced elastic modulus.

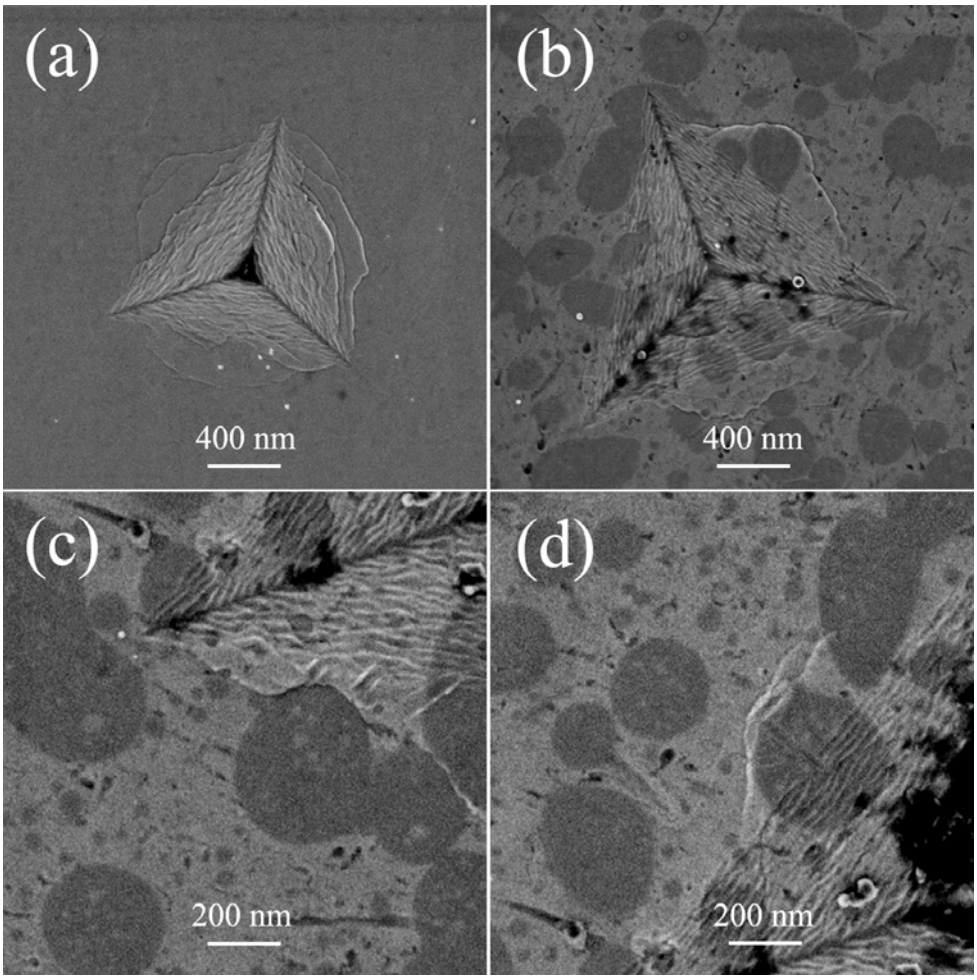

Figure 3.37. Scanning electron micrographs of: (a) an indentation performed in the single-phase amorphous $Ni_{59.5}Nb_{40.5}$ alloy, (b-d) indentations performed in the Ni-Nb-Y alloy.

Detailed morphological features inside and around the nanoindentations were observed by HRSEM. Figure 3.37 a) shows the typical morphology of an indentation and its vicinity for the $Ni_{59.5}Nb_{40.5}$ single-phase alloy, revealing similar features as those observed by Jiang and

Atzmon in an Al-based metallic glass [118]. The same morphology in the surroundings of an indentation is found for the $Ni_{57.5}Y_{42.5}$ alloy, but with larger indentation size due to its lower hardness (see Table 3.IX). Both single-phase metallic glasses present few slip-steps on the top of the surface surrounding the indents. This indicates that the shear bands which formed the slip-steps could freely propagate around the indenter following the induced strain field. The plane-strain distribution evolution during an indentation test in a metallic glass has been calculated by finite element analyses [120]. These calculations show that slip-steps are formed due to the propagation of several shear-bands, and are visualized as pop-in events in the load-displacement nanoindentaion curves. On the other hand, the two-phase alloy also presents slip-steps in the vicinity of the indents, but their distribution is different compared to the single-phase amorphous samples [compare Fig. 3.37 a) with Fig. 3.37 b)]. In this case, the shear-bands form and propagate in the matrix, since it is softer than the globular phase. But once a shear band collides with the Nb-rich phase, it is either deflected, as shown in Figs. 3.37 b) and 3.37 c), or stopped, as shown in Fig. 3.37 d). Note that after deflection, the shear bands do not follow arbitrary trajectories, but tend to propagate along the boundaries of the Nb-rich globular phase. Actually, the presence of the Nb-rich phase makes the stress state in the matrix highly inhomogeneous, similarly to what has been reported in a composite materials consisting of crystalline particles dispersed in an amorphous matrix [121] and as shown in section 1.2.1.1. Due to the difference in elastic modulus between the two phases, a misfit strain is induced around the precipitates during deformation which causes a load transfer to the matrix. As a result of this local stress increase in the vicinity of the globular phase the overall stress distribution is modified compared to the single phase alloy. Shear bands initiate in regions where the yield stress is overcome by the indentation-induced stresses and propagate along directions where the local stress is higher than the yield stress, i.e. predominantly along the boundaries of the globular phase. Shear bands eventually stop if they encounter a region where the shear stress is insufficient to sustain shear band propagation. This is for example the case inside the harder globular phase [see Fig. 3.37 d)], where the yield stress is larger than in the matrix and thus the yield criterion is not satisfied. As a result of the stress distribution in the two-phase amorphous alloy, shear band propagation is hindered and restricted in the soft-matrix.

In conclusion, the mechanical behaviour of a two-phase metallic glass, consisting of a Y-rich softer matrix and a globular harder Nb-rich phase, has been investigated by nanoindentation. The reduced elastic modulus of the two-phase ternary alloy can be described by a proportional addition of the reduced elastic modulus of the different constituent phases. The propagation of shear bands during deformation mainly initiates in the softer matrix, but it is interrupted or deflected when they collide with the globular harder phase. Therefore, the plasticity and the hardness of the two-phase alloy are enhanced with respect to the single softer amorphous alloy composing the matrix and their magnitude can not be predicted by the simple rule of mixtures of the composite.

3.5 Severe plastic deformation of a $Ti_{60}Cu_{14}Ni_{12}Sn_4Nb_{10}$ nanocomposite alloy studied by nanoindentation technique

Adding several percent of refractory metals, e.g. Nb or Ta, into a Ti-base BMG forming alloy, He et al. obtained micrometer-scale dendritic crystalline phase in a nano/ultrafine eutectic matrix [122]. The refractory metal in these alloys induces the precipitation of a β-Ti solid solution with dedritic morphology at the early stage of solidification, while the remaining liquid then transforms into a nano/ultrafine-structure at the later stage of solidification [122], leading to a nanocomposite alloy instead of a metallic glass matrix, as it would be expected. Nevertheless, this morphology yields excellent mechanical properties such as high strength, typical of nanostructured materials [123], combined with enhanced plasticity [122].

In this section, the microstructure and mechanical properties of a Ti-based multicomponent alloy composed of micrometer-sized dendrites embedded in a nanostructured eutectic matrix have been studied before and after subjecting it to high pressure torsion (HPT). HPT causes an enhancement of the overall hardness of the alloy due to high microstrains and grain refinement of the different constituent phases. Nanoindentation experiments are used to probe the local hardening during HPT of each individual phase. The indentation size effects and the applicability of the rule of mixtures of the constituent phases to extract the overall hardness of the composite are investigated. In the arc-melt state the dendrites are harder than the nanostructured eutectic matrix. Since HPT forces the material to plastically deform without fracture, the nanostructured eutectic matrix undergoes significant work-hardening during HPT. The contribution of the local hardening of each phase to the overall mechanical response in the HPT alloy is discussed.

An ingot with the composition $Ti_{60}Cu_{14}Ni_{12}Sn_4Nb_{10}$ was prepared by arc-melting a mixture of the pure elements under argon atmosphere. Pieces from the arc-melted alloy (AM) were processed by HPT, subjecting them to 5 whole-turn torsion under an applied pressure of 4 GPa, using a modified Bridgeman anvil type device [124] in the constrained geometry.

3.5.1. Microstructure before and after severe plastic deformation

Figures 3.38 a) and b) show SEM images of the AM alloy. Micrometer-sized dendrites (A), an eutectic matrix (B) and precipitated phases (C and D) compose the microstructure of the AM alloy; the D phase is mainly found surrounding the dendrites. EDX results show that the dendrites are enriched in Nb and Sn, while the matrix is enriched in Cu and Ni (see Table 3.X). Taking into account that Nb and Sn are β-stabilizers [125], the dendrites are assumed to be a β-Ti solid solution; in agreement with the XRD patterns (shown later) and previous results reported in the literature [126-129]. The C and D regions are enriched in Cu and Ni and presumably are intermetallic phases precipitated during cooling of the melt, after the formation

of the dendrites. Furthermore, Figs. 3.38 a) and b) reveal that the eutectic matrix is composed of nanoscale lamellae (their width is around 100 nm), and appear to have varying lamellae spacing, probably because of the different orientation of the eutectic colonies.

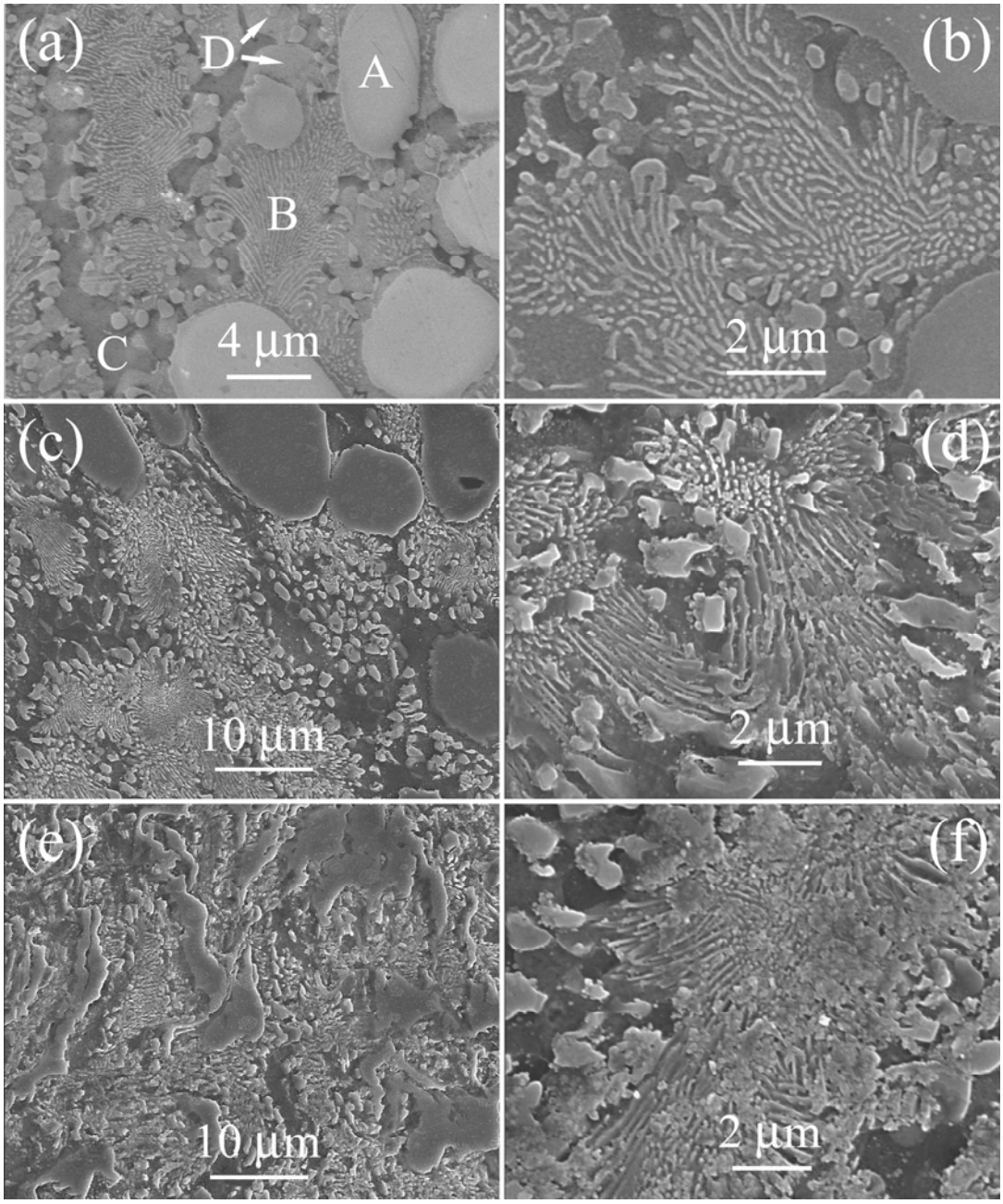

Figure 3.38. Scanning electron microscopy (SEM) images of the $Ti_{60}Cu_{14}Ni_{12}Sn_4Nb_{10}$ alloys corresponding to: a) and b) the AM specimen; c) and d) the center of the disk processed by HPT; e) and f) the edge of the HPT disk.

The consequences of the severe plastic deformation on the microstructure of the alloy are evidenced in Fig. 3.38 c)-f). Near the centre of the disk the dendrites are virtually not deformed and still maintain a rounded shape [see Figs. 3.38 c)]. Furthermore, the precipitated phases appear to be almost unaffected. However, as can be seen in Fig. 3.38 d), the eutectic

lamellae become severely distorted. HPT deforms and bends the lamellae and although they remain parallel, a loss of a preferential directionality is observed. At the disk edges both the dendrites and the eutectic are affected. As shown in Fig. 3.38 e), the dendrites become deformed and elongated, in contrast to what is observed at the centre of the disk, since the strain level during HPT process is higher at the edge [130]. The eutectic matrix is also deformed and the lamellae are even more distorted than in the centre of the disk [see Fig. 3.38 f)].

at%	Ti	Cu	Ni	Sn	Nb
A	59	5	2	8	26
B	54	16	21	3	6
C	62	24	10	0	4
D	50	25	24	0	1

Table 3.X. EDX compositional analyses, corresponding to Figure 2 a), for the different phases present in the AM specimen of the $Ti_{60}Cu_{14}Ni_{12}Sn_4Nb_{10}$ alloy. Note that the compositions for B are averaged values over the different eutectic phases.

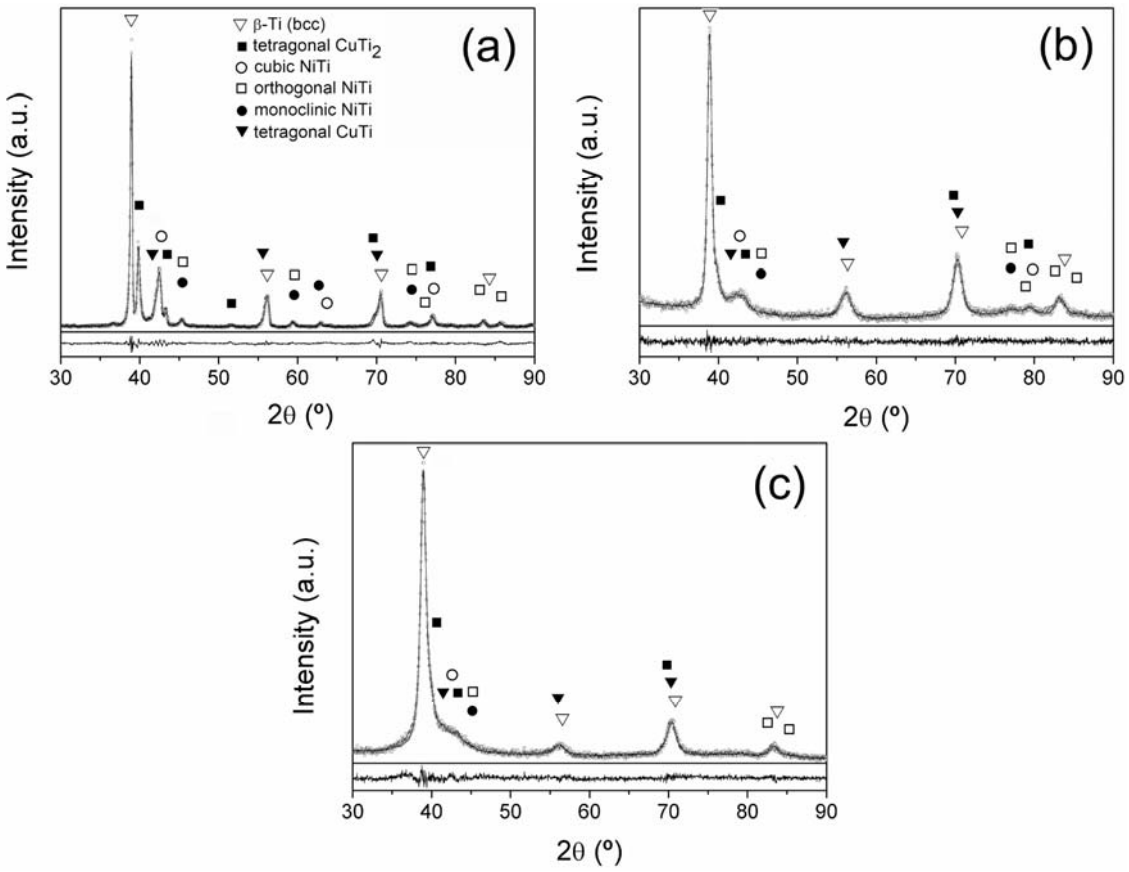

Figure 3.39. X-ray diffraction patterns of $Ti_{60}Cu_{14}Ni_{12}Sn_4Nb_{10}$ alloys corresponding to: a) the AM sample, b) the central part of a disk processed by HPT and c) the edge of a disk processed by HPT. Plotted together with the experimental data are fits obtained using the full-pattern fitting procedure (Rietveld method) and the corresponding difference between the calculated and the experimental profiles. The main peaks of the different phases are also indicated.

Figure 3.39 shows the XRD patterns from a) the AM sample, b) the HPT disk centre and c) the HPT disk edge. Plotted together with the experimental data are fits obtained using the full-pattern fitting procedure (Rietveld method [131,132]) and the corresponding difference between experimental and calculated profiles. Since the β-Ti reflections are asymmetric, two β-Ti phases were considered in order to fit well the XRD spectra. These two β-Ti phases form the dendrites and one of the phases in the eutectic colonies [126,133] and have slightly different lattice parameters, as recently reported by Woodcook et al. through transmission electron microscopy investigations [129]. The higher lattice parameter of the β-Ti forming the dendrites is probably due to the higher amount of solvents, i.e. Sn and Nb (see Table 3.X). The AM and HPT samples also show the presence of tetragonal $CuTi_2$ (I4/mmm), tetragonal CuTi (Pnmm), cubic NiTi (Pm3m), orthogonal NiTi (Pmma) and monoclinic NiTi (P21/m) phases. The crystallite sizes and the microstrains for each phase and sample are summarized in Table 3.XI. The table reveals that HPT causes a significant structural refinement in all the phases and confirms that, indeed, this refinement is more pronounced at the disk edges.

	AM		HPT center		HPT edge	
	D (nm)	$<\varepsilon^2>^{1/2}$ x 10^{-3}	D (nm)	$<\varepsilon^2>^{1/2}$ x 10^{-3}	D (nm)	$<\varepsilon^2>^{1/2}$ x 10^{-3}
β-Ti (dendrites)	100 ± 3	1.8±0.1	42 ± 3	4.3 ± 0.3	21 ± 1	4.5 ± 0.5
β-Ti (eutectic)	36 ± 2	1.0±0.2	13 ± 1	3.5 ± 0.2	10 ± 1	6.0 ± 0.5
tetragonal $CuTi_2$ (I4/mmm)	51 ± 3	0.6±0.1	14 ± 1	2.0 ± 0.1	8 ± 1	4.0 ± 0.2
monoclinic NiTi (P21/m)	37 ± 2	1.8±0.1	25 ± 2	1.8 ± 0.1	7 ± 1	5.0 ± 0.3
orthogonal NiTi (Pmma)	26 ± 2	0.9±0.1	10 ± 2	1.0 ± 0.1	8 ± 1	3.5 ± 0.2
cubic NiTi (Pm3m)	50 ± 3	2.7±0.2	15 ± 2	2.7 ± 0.2	13 ± 1	2.5 ± 0.2
Tetragonal CuTi (P4/nmm)	70 ± 3	3.3±0.2	16 ± 2	0.8 ± 0.1	10 ± 1	3.0 ± 0.2

Table 3.XI. Summary of the crystallite sizes, D, and microstrains, $<\varepsilon^2>^{1/2}$, of the different phases present in the different samples of $Ti_{60}Cu_{14}Ni_{12}Sn_4Nb_{10}$ alloy.

3.5.2. Phase distribution and microstructure of the AM alloy

Previous investigations have described the microstructure of similar compositions cast by rapid quenching techniques, i.e., Cu-mould casting [122,127-129]. Such alloys present a dendrite structure surrounded by a matrix composed of eutectic regions and a third phase,

identified as tetragonal $CuTi_2$ [129]. In the present case, the AM sample also shows a dendrite structure, however the matrix differs in the constituent phases. Namely, apart from the eutectic regions present in the matrix, two precipitated phases are observed instead of one, which correspond to the C and D regions in Fig. 3.38 (a). According to EDX measurements (see Table X) combined with the XRD analyses (see Table 3.XI) the D phase is ascribed to be tetragonal CuTi, with some Ni dissolved in its structure as a substitutional element for Cu, while tetragonal $CuTi_2$ constitutes the second precipitated phase (C), also with some Ni dissolved. Furthermore, the XRD analyses and the SEM images, in agreement with Woodcock et al. [129] and previous work from Concustell et al. [133], indicate that β-Ti, cubic NiTi (Pm3m), orthogonal NiTi (Pmma) and monoclinic NiTi (P21/m) compose the eutectic regions. The high cooling rate and the Cu content in the NiTi eutectic phases favor the formation of the NiTi martensitic product phases (orthogonal and monoclinic) from the austenitic parent phase (cubic) [134,135]. Woodcock et al. suggested that the tetragonal $CuTi_2$ phase is the equilibrium phase in the rapidly quenched $Ti_{60}Cu_{14}Ni_{12}Sn_6Ta_{10}$ alloy, while the formation of the metastable β-Ti – NiTi eutectic is favoured by both the high cooling rate and the addition of Nb and Sn which kinetically exclude the formation of the equilibrium phase [128,129]. Our results indicate that, apart of the formation of the metastable eutectic, the tetragonal CuTi compound, which is also metastable, precipitates at the regions surrounding the dendrites and the eutectic counterparts. This may be assisted by the rejection of Cu and Ni from the β-Ti phases (composing the dendrites and the eutectic) during cooling, creating Cu- and Ni-rich zones in their surroundings and, therefore, allowing the formation of the observed CuTi phase.

3.5.3. Microstructural changes after high pressure torsion

During HPT processing the applied strain increases towards the edge of the disks [130]. Therefore, the samples undergo different levels of deformation along the radius. Near the centre of HPT disks, as it has been previously mentioned, the dendrites seem rather unaffected, although the XRD analyses show that the β-Ti dendritic phase has smaller crystallite size and higher microstrains than in the AM as a result of the severe plastic deformation and the increment of dislocation density accompanying the HPT process. Such effect is more evident at the edge of the disk, where the dendrites become elongated and even smaller crystallite sizes and higher microstrains are obtained (see Table 3.XI). Concerning the eutectic regions, it is noteworthy that the lamellae colonies become bent after HPT, both at the centre and edges of the disk. This morphology might be related to the highly localized deformation processes, which occur in order to accommodate the shear strain under the constrained geometry imposed by HPT and result in a reduction of the crystallite size and an increase of the microstrains of the constituent phases. However, contrary to what has been reported for AlCu eutectic alloys subjected to equal channel angular pressing (ECAP) [136], no periodic shear banding is observed in our case. This is probably due to the fact that HPT is more energetic than ECAP and also because of the lack of ductility of the Ti-based eutectic matrix in the present studied alloy [137].

3.5.4. Nanoindentation results on the $Ti_{60}Cu_{14}Ni_{12}Sn_4Nb_{10}$ composite (AM and HPT alloys)

The nanoindentation tests were run in load control mode at a constant loading time of 15 s, applying maximum forces of 3, 10, 25, 50 and 500 mN held during 30 s followed by unloading at a constant time of 15 s. For each condition, a set of 100 indentations was performed. For low values of maximum loads, each phase composing the alloy could be indented separately. After nanoindentation tests, the specimens were observed by SEM to identify each individual indent site, as shown in Fig. 3.40.

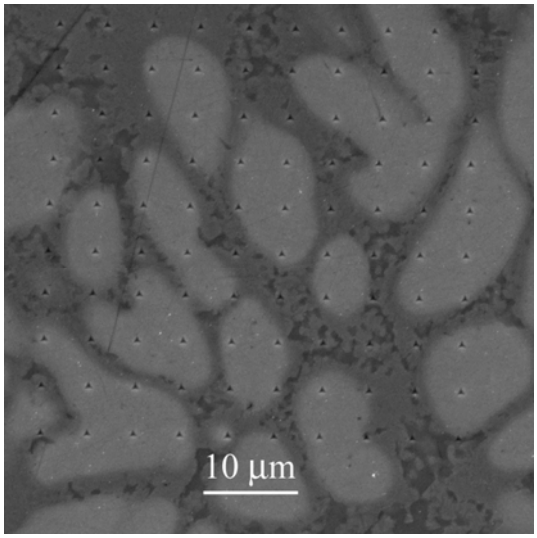

Figure 3.40. Scanning electron microscopy (SEM) image of an array of indentations performed using a maximum indentation load of 3 mN on the $Ti_{60}Cu_{14}Ni_{12}Sn_4Nb_{10}$ alloy processed by HPT (centre of the disk).

Figure 3.41 presents load-displacement (*F-h*) nanoindentation curves for a) AM, b) centre and c) edge of the HPT disk with a maximum applied load of 3 mN. Due to this small load value, it is possible to evaluate the hardness and reduced elastic modulus of each individual phase separately. However, due to their small percentage and the concomitant difficulty of being independently indented, the nanomechanical response of the intermetallic phases is not presented. The hardness, H, and the reduced elastic modulus, E_r, values for the dendrites and the eutectic matrix, deduced from the curves in Fig. 3.41, are given in Table 3.XII.

Nanoindentation curves for the AM alloy reveal a clear difference in the nanomechanical properties of each phase, i.e. the displacement into the sample for the indentations corresponding to the dendrites is much lower than in the ones belonging to the eutectic matrix, as shown in Fig. 3.41 a). Therefore, for the AM alloy, both H and E_r of the dendrites are higher than for the eutectic matrix (see Table 3.XII) in agreement with the results of Alcalá et al. [138]. The table also shows that the H and the E_r values obtained from nanoindentation tests are larger at the edge than in the centre of the HPT

specimen. However, each phase evolves in a different way. Near the disk centre, both the dendrites and the eutectic matrix harden compared to the AM alloy but the dendrites remain still harder than the eutectic matrix, while E_r becomes similar for both. At the edge of the disk, the hardness and the E_r values of both phases are almost equal, as shown in Table 3.XII.

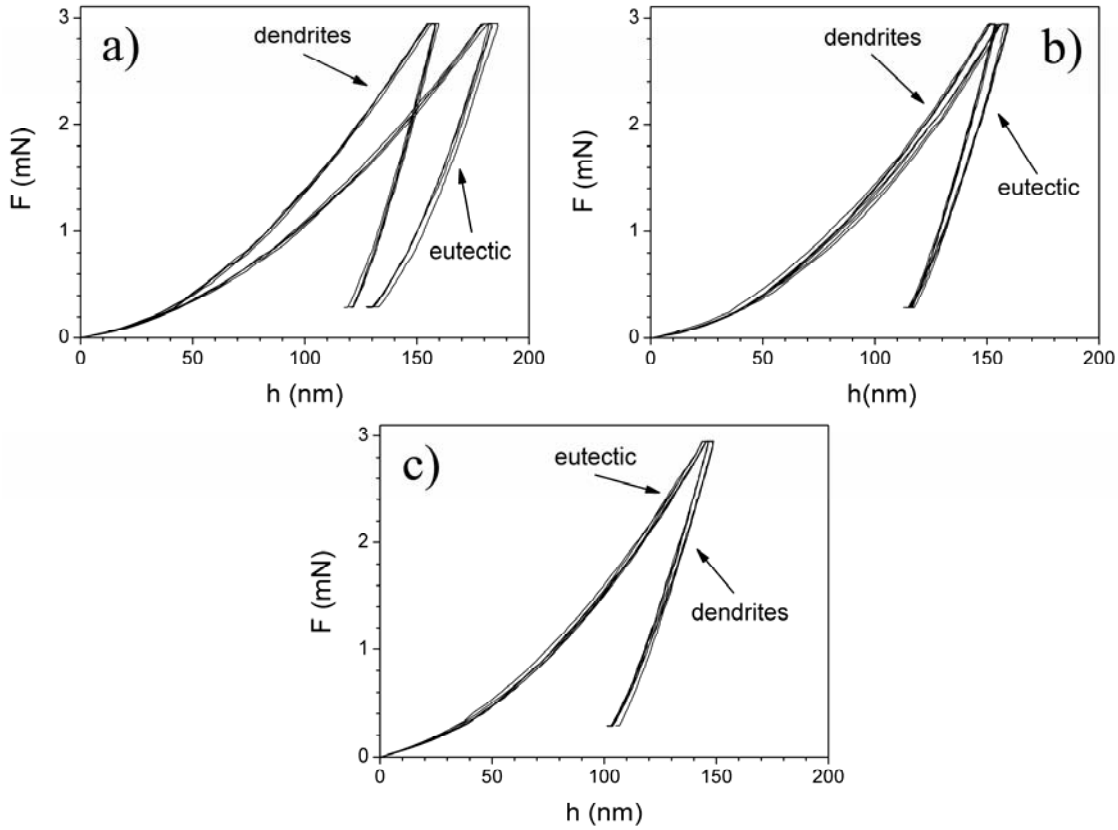

Figure 3.41. Load-displacement (F-h) curves of the $Ti_{60}Cu_{14}Ni_{12}Sn_4Nb_{10}$ alloys corresponding to: (a) the AM specimen, (b) centre and (c) edge of the HPT specimen.

	Dendrite		Eutectic	
	H (GPa)	E_r (GPa)	H (GPa)	E_r (GPa)
AM	6.3 ± 0.3	115 ± 8	5.0 ± 0.3	86 ± 9
HPT center	7.0 ± 0.2	118 ± 5	6.4 ± 0.2	111 ± 6
HPT edge	7.5 ± 0.2	121 ± 4	7.7 ± 0.3	118 ± 6

Table 3.XII. Hardness (H) and reduced elastic modulus (E_r, as defined by Oliver and Pharr [9]) obtained by nanoindentation of the dendrites and eutectic regions in the $Ti_{60}Cu_{14}Ni_{12}Sn_4Nb_{10}$ alloys.

It is well-known that in crystalline materials the hardness of an alloy increases when decreasing the maximum applied load [139,140]. This effect has been reported to be more pronounced for larger grain sizes and has been attributed to the interaction of dislocations loops

with each other and with the crystal surface [140]. Figure 3.42 shows the dependence between hardness and penetration depth corresponding to the AM, for both the dendrites and the eutectic matrix when they are independently indented at different maximum forces. Note that the indentation size effect of the constituent phases could only be studied using forces of up to 50 mN. For larger load values, the indentations always affected both the dendrites and the eutectic matrix simultaneously. Figure 3.42 evidences that indentation size effects are larger for the dendrites, which can be ascribed to their larger crystallite size, as shown in Table 3.XI. Interestingly and in spite of the indentation-size effect, the hardness of the dendrites in the AM remains always higher than in the eutectic matrix.

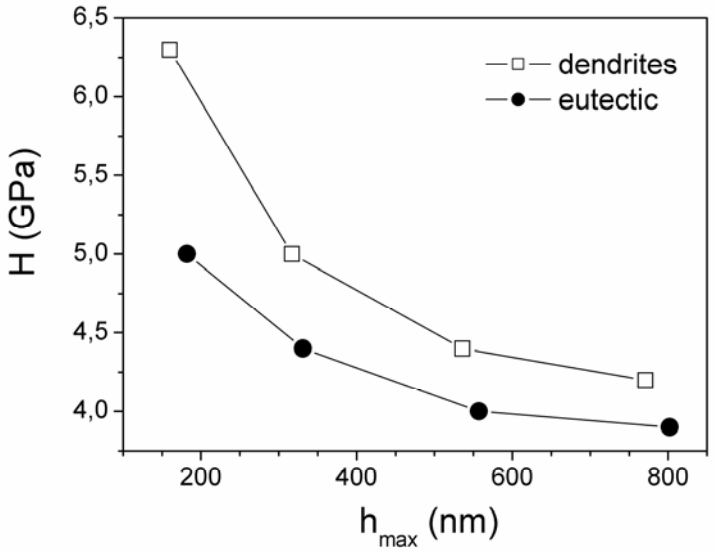

Figure 3.42. Dependence of the hardness on the penetration depth for the dendrites (□) and the eutectic matrix (●) in the AM specimen of the $Ti_{60}Cu_{14}Ni_{12}Sn_4Nb_{10}$ alloy.

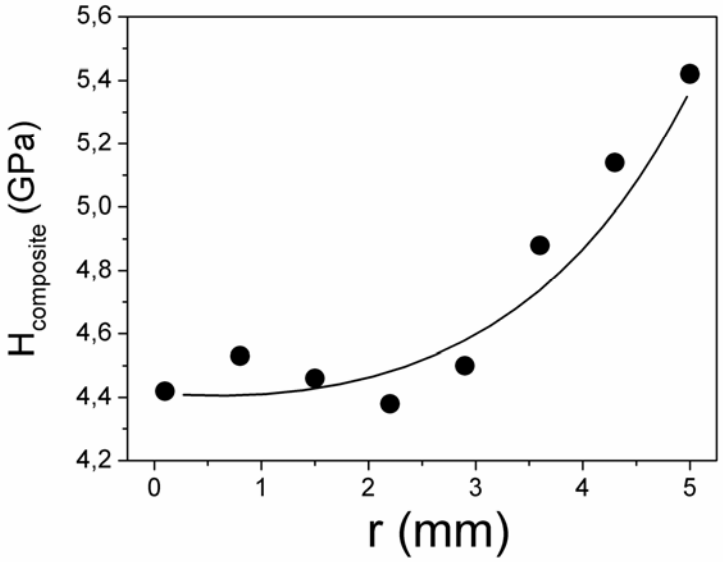

Figure 3.43. Dependence of the composite hardness on the radius of the HPT disk of the $Ti_{60}Cu_{14}Ni_{12}Sn_4Nb_{10}$ alloy, evaluated from indentations using a maximum load of 500mN.

Finally, the dependence of the overall hardness, evaluated from nanoindentations using a maximum load of 500 mN, on the distance from the disk centre for the alloy processed by HPT is shown in Fig. 3.43. The hardness of the composite is found to progressively increase towards the edge of the HPT disk.

3.5.5. Nanomechanical characterization and overall mechanical hardening

The nanoindentation experiments probe the local mechanical behaviour of the individual phases present in the different specimens. The results of hardness and reduced elastic modulus of the individual phases in the AM alloy presented in this work (Table 3.XII) are in agreement with the compression test results of He et al. [137], who have shown that the elastic modulus of a monolithic nanostructured eutectic sample is lower than that of a dendrite – nanostructured eutectic alloy. Therefore, the precipitation of dendrites, with higher elastic modulus, produces an increase of the overall elastic modulus in the rapidly quenched alloy. Furthermore, He et al. also pointed out that the high macroscopic fracture strain of the rapidly quenched specimens is caused by the obstruction of the shear band propagation by the mechanically harder dendrites, which would be also in agreement with the present results.

Different strengthening mechanisms are responsible for the large hardness values observed in the AM alloy. The dissolution of Nb and Sn in the β-Ti dendrites and the dislocation density due to the rapid cooling, observed as microstrain in the XRD analysis, are the principal hardening mechanisms in the dendrites. Note that the solution hardening in the β-Ti phase of the dendrites is more pronounced than in the β-Ti of the eutectic matrix, due to the higher solute concentration (see Table 3.X). This can explain the higher values of hardness obtained in the dendrites (as shown in Table 3.XII). The nanometer-scale eutectic matrix strengthens the alloy by the presence of a large number of grain boundaries, which have an effect on the deformation behaviour by serving as an effective barrier to the movement of dislocations [115]. Actually, this structural refinement leads to a large mechanical hardness in agreement with the Hall-Petch relationship, as has been reported for some eutectic alloys [141].

In addition to the local mechanical properties, nanoindentation tests also allow probing the overall mechanical behaviour of the composite, when the indentations are large enough (i.e, for sufficiently large maximum loads) to affect both the dendrites and the eutectic matrix at the same time. Figure 3.44 shows the overall hardness values evaluated at different forces, i.e. 10, 25, 50, 500 mN, in the AM alloy. These values have been obtained averaging from different indentations, which have indented dendrites and eutectic matrix simultaneously. It is noteworthy that an indentation size effect is also observed for the overall hardness values of the composite.

On the other hand, in composite materials, it is common to assume that the overall hardness of the composite is directly proportional to the hardness of the different constituent phases [127]. Hence, if we neglect the contribution from the tetragonal CuTi and the tetragonal $CuTi_2$ secondary precipitated phases (whose volume percentage is around 10 %), the hardness of the composite can be written as: $H_{composite} = A\,H_E + B\,H_D$, equivalent to eq. 3.12, where H_E

and H_D are the hardness values of the eutectic and dendrites while *A* and *B* are the eutectic and dendrites volume phase percentages. From an ensemble of twenty SEM images corresponding to the AM sample, the phase percentages *A* and *B* have been determined to be 55% and 45%, respectively. From these phase percentages and the local hardness values in the dendrites and eutectic regions (evaluated only for loads up to 50 mN), one obtains the hardness values which are plotted as open symbols in Fig. 3.44. Interestingly, the hardness values of the composite calculated from the rule of mixtures of the constituent phases agree reasonably well with the measured ones. The small discrepancies may be due to the contribution of the precipitated phases whose hardness is even higher than that in the dendrites. Note also that for the smallest penetration depth (i.e., when the maximum load is only 3 mN) the dendrites and the eutectic are always separately indented. Hence, the hardness of the composite can only be estimated using the rule of mixtures. However, as evidenced in Fig. 3.44, the overall hardness of the AM alloy can only be determined from the rule of mixtures of a composite if the local hardness values are also evaluated at the same indentation depths.

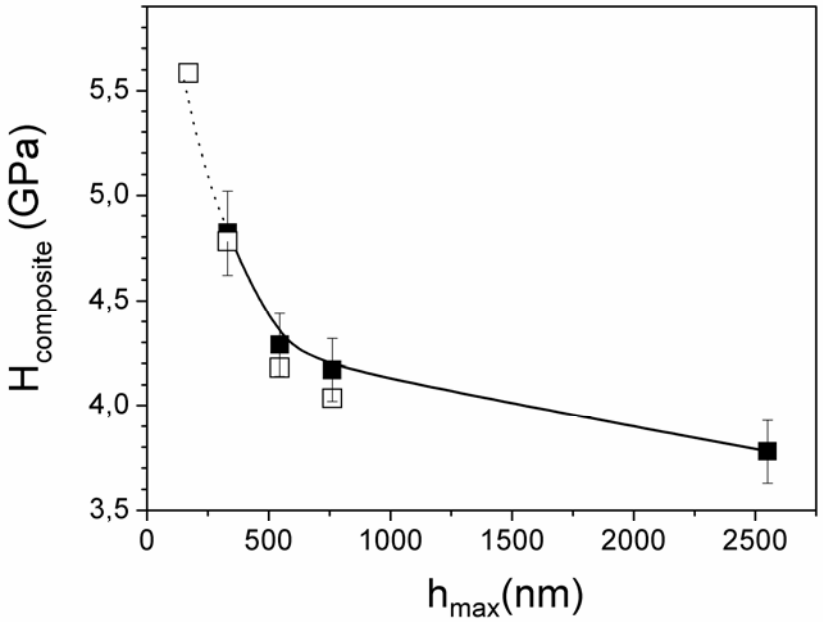

Figure 3.44. Dependence of the measured overall hardness of the composite on the indentation depth for the AM specimen of the $Ti_{60}Cu_{14}Ni_{12}Sn_4Nb_{10}$ alloy (■). Calculated composite hardness using the rule of mixtures (□).

The HPT processing brings about a further increase of the hardness of the individual constituent phases (see Fig. 3.44 and Table 3.XII). However, comparing the mechanical properties of the AM with those at the centre of the HPT specimens it can be seen that the hardness increase of each phase is different: the dendrites have an increment of 9% while the hardness in the eutectic regions increases by 28%. A similar difference is observed when comparing the local hardness increases between the centre and the edge of the HPT specimen. Overall, the eutectic regions harden three times more than the dendrites when severe plastic deformation is applied on the alloy. This indicates that during HPT the eutectic matrix undergoes high plastic deformation. It should be noted that under the constrained conditions of

the HPT process, the eutectic colonies have to deform through the creation of dislocations and grain refinement, as evidenced by the broadening of the XRD peaks, in order to accommodate the shear strain. This brings about a loss of preferential directionality of the eutectic lamellae [see Figs. 3.38 d) and f)]. Moreover, the heat generated during deformation may help the dislocations to rearrange into low-angle grain boundaries [115]. These deformation mechanisms also contribute to the hardening of the eutectic matrix measured by nanoindentation. Furthermore, the structural refinement restricts further deformation not only by hindering the dislocation movement but also by limiting the eutectic interlamellar glide. This latter mechanism has been reported to control the mechanical properties of several eutectic systems, particularly when the phases composing the lamellae are not structurally coherent [142]. It should be noted that as the lamellae progressively bend, the eutectic colonies tend to overlap [see Fig. 3.38 f)] and, as a result, interlamellae glide along preferential orientations becomes restricted. On the other hand, the harder dendrites can only accommodate the shear strain by the creation of dislocations and grain refinement, thus leading to a lower total hardening than in the eutectic regions. It is worth mentioning that the dendrites only become deformed, i.e., elongated, at the edge of the HPT disk [see Fig. 3.38 e)] where the eutectic matrix becomes hard enough to force this deformation, as shown in Table 3.XII.

Using a large applied load (500 mN), the overall hardness of the composite after HPT has also been evaluated. As expected, the overall hardness also increases as the distance from the disk centre is increased (see Fig. 3.43). When the rule of mixtures is applied to the AM and HPT sample using the local hardness values obtained at 3 mN, overall composite hardness values of 5.6, 6.7 GPa and 7.6 GPa are obtained for the AM, at the centre of the HPT disk and at the edge of the HPT disk, respectively. However, the measured hardness values applying 500 mN are much lower. This difference can be again ascribed to the indentation-size effect. Actually, the overall hardness in the AM, the centre and the edge of the HPT disk evaluated using 500 mN are 32 %, 34 % and 29 % lower than when the applied maximum load is 3 mN. These values are very similar and denote that, once indentation size effects are taken into account, the hardening in the HPT disk, as it has been shown for the AM alloy, can be correlated with the local hardening of the constituent phases.

In summary, our results demonstrate that HPT is a very effective technique to mechanically harden bulk nanocomposite materials. The nanoindentation experiments shed light to the mechanical behaviour of these alloys, illustrating that the overall mechanical hardening of these materials is due to the hardening of each individual phase composing them. The microstructure evolution and the mechanisms of mechanical hardening during high pressure torsion in a Ti-based dendrite/eutectic nanostructured alloy have been investigated. In the initial arc-melt sample the dendrites are found to be harder than the eutectic matrix. During HPT both the dendrites and the eutectic strengthen. This is due to the structural refinement that occurs in all phases during the severe plastic deformation imposed by HPT. Interestingly, this hardening is more pronounced for the eutectic regions, probably due to the bending effect observed in the lamellae which causes a concomitant loss in their directionality, thus hindering the interlamellar glide. Furthermore, we have demonstrated that the well-known indentation size effect also occurs in composite materials. The estimation of the overall hardness from the hardness of the

constituent phases is only possible when using local hardness values evaluated at similar indentation depths.

References

[1] Inoue A, Zhang T, Masumoto T: Mater Trans JIM 1990; 31:177.

[2] Inoue A, Nishiyama N, Matsuda T: Mater Trans JIM 1996; 37:181.

[3] Nishyama N, Inoue A: Mater. Trans JIM 1999; 40:64.

[4] Löffler JF, Schroers J, Johnson WL: Appl Phys Lett 2000; 77:681.

[5] Kempen ATW, Sommer F, Mittemeijer EJ: Acta Mater 2002; 50:1319-1329.

[6] Mattern N, Hermann H, Roth S, Sakowski J, Macht MP, Jovari P, Jiang J: Appl Phys Let 2003; 82:2589.

[7] Mukai T, Nieh TG, Kawamura Y, Inoue A, Higashi K: Intermetallics 2002; 10:1071.

[8] Mukai T, Nieh TG, Kawamura Y, Inoue A, Higashi K: Scripta Mater 2002; 46:43.

[9] Oliver WC, Pharr GM: J Mater Res 1992; 7:1564.

[10] Cheng YT, Cheng CM: Int J Solids and Struct 1999; 36:1231.

[11] Zeng K, Chiu CH: Acta Mater 2001; 49:3539.

[12] Ocelík V, Csach K, Kasardová A, Bengus VZ: Mater Sci Eng A 1997; 226-228:851.

[13] Kursumovic A, Cantor V: Scripta Mater 1996; 34:1655.

[14] Concustell A, Sort J, Greer AL, Baró MD: Appl Phys Lett 2006; 88:171911.

[15] Berry BS: Metallic Glass (American Society for Metals, Metals Park, OH, 1976).

[16] Concustell A, Sort J, Alcalá G, Mato S, Gebert A, Eckert J, Baró MD: J Mater Res 2005; 20:2719.

[17] Spaepen F: Acta Metall 1977; 25:407.

[18] Li J, Spaepen F, Hufnagel TC: Phil Mag 2002; 82:2623.

[19] Li J, Wang L, Hufnagel TC: Phys Rev B 2002; 65:144201.

[20] Wright WJ, Hufnagel TC, Nix WD: J Appl Phys 2003; 93:1432.

[21] Kimura H, Masumoto T: Acta Metall 1983; 31:231.

[22] Turnbull D, Cohen M: J Chem Phys 1958; 29:1049.

[23] Duine PA, Sietsma J, van den Beukel A: Acta Metall Mater 1992; 40:743.

[24] Van Aken B, de Hey P, Sietsma J: Mater Sci Eng A 2000; 278:247.

[25] Schuh CA, Argon AS, Nieh TG, Wadsworth J: Phil Mag A 2003; 83:2585.

[26] Schuh CA, Nieh TG, Kawamura Y: J Mater Res 2002; 17:1651.

[27] Schuh CA, Nieh TG: Acta Mater. 2003; 51:87.

[28] Greer AL, Castellero A, Madge SV, Walker IT, Wilde JR: Mater Sci Eng A 2004; 375-377:1182.

[29] Fischer-Cripps AC: Vacuum 2000; 58:569.

[30] Larsson PL, Giannakopoulos AE, Soderlund E, Rowcliffe J, Vestergaard R: Int J Sol Struct 1996; 33:221.

[31] Argon AS: Acta Metall 1979; 27:47.

[32] Steif PS, Spaepen F, Hutchinson JW: Acta Metall 1982; 30:447.

[33] Li J, Spaepen F, Hufnagel TC: Phil Mag 2002; 82:2623.

[34] Li J, Wang L, Hufnagel TC: Phys Rev B 2002; 65:144201.

[35] Schuh CA, Lund AC, Nieh TG: Acta Mater 2004; 52:5879.

[36] Inoue A, Kato A, Zhang T, Kim SG, Masumoto T: Mater Trans JIM 1991; 32:609.

[37] Peker A, Johnson WL: Appl Phys Lett 1993; 63:2342.
[38] Inoue A: Mater Trans JIM 1996; 37:181.
[39] Inoue A, Zhang T, Nishiyama N, Ohba K, Masumoto T: Mater Lett 1994; 19:131.
[40] Inoue A, Zhang W, Zhang T, Kurosaka K: Acta Mater 2001; 49:2645.
[41] Révész Á, Concustell A, Varga LK, Suriñach S, Baró MD: Mater Sci Eng A 2004; 375–377:776.
[42] Jiang JZ, Yang B, Saksl K, Franz H, Przds N: J Mater Res 2003; 14:895.
[43] Révész Á, Varga LK, Suriñach S, Baró MD: J Mater Res 2002; 17:2140.
[44] Louzguine DV, Inoue A: J Mater Res 2002; 17:2112.
[45] Lee JC, Kim YC, Ahn JP, Kim HS, Lee SH, Lee BJ: Acta Mater 2004; 52:1525.
[46] Inoue A, Zhang W, Zhang T, Kurosaka K: J Non-Crys Sol 2002; 304:200.
[47] Busch R, Bakke E, Johnson WL. Acta Mater 1998; 46:4725.
[48] Einstein A: Ann Phys 1911; 34:592.
[49] Aronin AS, Abrosimova GE, Gurov AF, Kir´yanov Yu V, Molokanov VV: Mater Sci Eng A 2001; 304-306:375.
[50] Liu XD, Nagumo M, Umemoto M: Mater Sci Eng A 1998; 252:179.
[51] Johnson MWA, Mehl KF: Trans Am Inst Min Metall Pet Eng 1939; 135:416.
[52] Avrami M: J Chem Phys 1939; 7:1103.
[53] Avrami M: J Chem Phys 1940; 8:212.
[54] Avrami M: J Chem Phys 1941; 9:177.
[55] Kolmogorov AN: Izv Akad Nauk USSR Ser Matem 1937; 3:355.
[56] Christian JW: The Theory of Transformations in Metals and Alloys, 2nd ed., (Pergamon, Oxford, 1975).
[57] Botstein O, Rabinkin A: Mater Sci Eng A 1994; 188:305.
[58] Arroyave R, Eagar TW, Kaufman L: J Alloys Comp 2003; 351:158.
[59] Glade SC, Löffler JF, Bossuyt S, Johnson WL: J Appl Phys 2001; 89:1573.
[60] Foley JC, Allen DR, Perpezko JH: Scri Mater 1996; 35:655.
[61] Calin M, Köster U: Mater Sci Forum 1998; 269-272:749.
[62] Révész Á, Donnadieu P, Simon JP, Guyot P, Ochin P: Phil Mag Lett 2001; 81:767.
[63] Xing LQ, Bertrand C, Dallas JP, Cornet M: Mater Sci Eng A 1998; 241:216.
[64] Barbee TW, Walmsley Jr RG, Marshall AF, Keith DL, Stevenson DA: Appl Phys Lett 1981; 38:132.
[65] Schultz R, Samwer D, Johnson WL: J Non-Cryst Solids 1984; 62:997.
[66] Inoue A, Chen S, Masumoto T: Mater Sci Eng A 1994; 346-350:346.
[67] Busch R, Schneider S, Peker A, Johnson WL: Appl Phys Lett 1995; 67:1544.
[68] Antonione C, Spriano S, Rizzi P, Baricco M, Battezzati L: J Non-Cryst Solids 1998; 232-234:127.
[69] Woychik CG, Massalski TB: Bd 1988; 79:149.
[70] Lewandowski JJ, Whang WH, Greer AL: Phil Mag Lett 2005; 85:77.
[71] Wright WJ, Schwarz RB, Nix WD: Mater Sci Eng A 2001; 319-321:229.
[72] Zhang Y, Greer AL: J Non-Cryst Solids in press.
[73] Egami T: Intermetallics 2006; 14:882.

[74] Lewandowski JJ, Greer AL: Nature Mater 2006; 5:15.
[75] Zhang ZF, Eckert J, Schultz L: Acta Mater 2003; 51:1167.
[76] Zhang ZF, He G, Eckert J, Schultz L: Phys Rev Lett 2003; 91:045505.
[77] Liu CT, Heatherly L, Easton DS, Carmichael CA, Schneibel JH, Chen CH, Wright JL, Yoo MH, Horton JA, Inoue A: Metall Mater Trans A 1998; 29A:1811.
[78] Pampillo CA: J Mater Sci 1975; 10:1194.
[79] Wright WJ, Saha R, Nix WD: Mater Trans JIM 2001; 42:642.
[80] Inoue A, Zhang T, Masumoto T: Mater Trans JIM 1995; 36:391.
[81] Lowhaphandu P, Ludrosky LA, Mongomery SL, Lewandowski JJ: Intermetallics 2000; 8:487.
[82] He G, Lu J, Bian Z, Chen D, Chen G, Tu G, Chen G: Mater Trans 2001; 42:356.
[83] Conner RD, Johnson WL, Paton NE, Nix WD: J Appl Phys 2003; 94:904.
[84] Hufnagel TC, El-Deiry P, Vinci RP: Scripta Mater 2000; 43:1071.
[85] Yokoyama Y, Yamano K, Fukaura K, Sunada H, Inoue A: Mater Trans 2001; 42:623.
[86] Gilbert CJ, Ritchie R, Johnson WL: Appl Phys Lett 1997; 71:476.
[87] Gilbert CJ, Schroeder V, Ritchie RO: Metall Mater Trans A 1999; 30A:1739.
[88] Zhang ZF, Eckert J, Schultz L: J Mater Res 2003; 18:456.
[89] Zhang ZF, Eckert J, Schultz L: Metall Mater Trans A 2004; 35A:3489.
[90] Xi XK, Zhao DQ, Pan MX, Wang WH, Wu Y, Lewandowski JJ: Phys Rev Lett 2005; 94:125510.
[91] Conner RD, Choi-Yim H, Johnson WL. J Mater Res. 1999; 14:3292.
[92] Subhash G, Dowding JR, Keczkes LJ: Mater Sci Eng 2002; A334:33.
[93] M. Kusy, U. Kühn, A. Concustell, A. Gebert, J. Das, J. Eckert, L. Schultz, and M.D. Baró: Intermetallics 2006; 14:982.
[94] Kanungo BP, Glade SC, Asoka-Kumar P, Flores KM: Intermetallics 2004; 12:1073.
[95] Fan C, Inoue A: Appl Phys Let 2000; 77:46.
[96] Flores KM, Dausdardt RH: Intermetallics 2004; 12:1025.
[97] Concustell A, Révész Á, Suriñach S, Varga LK, Heunen G, Baró MD: J Mater Res 2004; 19:505.
[98] Mulder AL, van der Zwaag S, van den Beukel A: Scripta Metal 1983; 17:1399.
[99] Allemand JP, Fouquet F, Perez J, de Guillebon B: Phys Stat Sol A 1988; 105:427.
[100] Ramamurty U, Lee M L, Basu J, Li Y: Scripta Mater 2002; 47:107.
[101] Bian Z, Chen GL, He G, Hui XD: Mater Sci Eng A 2001; 316:135.
[102] Wu TW, Spaepen F in: Mechanical Behavior of Rapidly Solidified Materials, (Warrendale, PA: The Metallurgical Society, Inc. 1986, Edited by Sastry SML and MacDonald BA).
[103] Kim HS, Hong SI: Acta Mater 1999; 47:2059.
[104] Kim HS: Mater Sci Eng A 2001; 304-306:327.
[105] Davis LA in: Mechanical Behavior of Rapidly Solidified Materials, (Warrendale, PA: The Metallurgical Society, Inc. 1986, Edited by Sastry SML and MacDonald BA).
[106] Kühn U, Eckert J, Mattern N, Schultz L: Appl Phys Lett 2002; 80:2478.
[107] Wada T, Inoue A, Greer AL: Appl Phys Lett 2005; 86:25197.

[108] Greer AL: Mater Sci Eng 2001; 304-306:68.
[109] Li F, Zhang T, Guan S, Shen N: Mater Lett 2005; 59:1453.
[110] Kündig AA, Ohnuma M, Ping DH, Ohkubo T, Hono K: Acta Mater 2004; 52:2441.
[111] Mattern N, Kühn U, Gebert A, Gemming T, Zinkevich M, Wendrock H, Schultz L: Scripta Mater 2005; 53:271.
[112] Park BJ, Chang HJ, Kim DH, Kim WT, Chattopadhyay K, Abinandanan TA, Bhattacharyya S: Phys Rev Lett 2006; 96:245503.
[113] Eckert J, Das J, Kim KB, Baier F, Tang MB, Wang WH, Zhang ZF: Intermetallics 2006; 14:876.
[114] Park ES, Kim DH: Acta Mater 2006; 54:597.
[115] Hertzberg RW: Deformation and Fracture Mechanics of Engineering Materials, fourth ed. (John Wiley & Sons, New York, 1996).
[116] Golovin YI, Ivolgin VI, Khonik VA, Kitagawa K, Tyurin AI: Scripta Mater 2001; 45:947.
[117] Schuh CA, Nieh TG: Acta Mater 2004; 52:5879.
[118] Jiang WH, Atzmon M: J Mater Res 2003; 18:755.
[119] Hufnagel TC, Ott RT, Almer J: Phys Rev B 2006; 73:064204.
[120] Anand L, Su C: J Mech Phys Sol 2005; 53:1362.
[121] Ott RT, Sansoz F, Molinari JF, Almer J, Ramesh KT, Hufnagel TC : Acta Mater 2005; 53:1883.
[122] He G, Eckert J, Löser W, Schultz L: Nat Mater 2003; 2:3.
[123] Koch CC, Morris DG, Lu K, Inoue A: MRS Bull 1999; 24:54.
[124] Bridgeman J: Processing of Metals under High Pressure Conditions, (Moscow, Tehizdat, 1936).
[125] Polmear IJ: Light Alloys. Metallurgy of Light Metals, third ed. (Arnold, London, 1995).
[126] Dai QL, Sun BB, Sui ML, He G, Li Y, Eckert J, Luo WK, Ma E: J Mater Res 2004; 19:2557.
[127] Sun BB, Sui ML, Wang YM, He G, Eckert J, Ma E: Acta Mater 2006; 54:1349.
[128] Woodcock TG, Xie FY, Alcalá G, Mato S, Gebert A, Löser W, Eckert J, Schultz L: J Metastable & Nano Mater 2005; 24-25:57.
[129] Woodcock TG, Kusy M, Mato S, Alcala G, Thomas J, Löser W, Gebert A, Eckert J, Schultz L: Acta Mater 2005; 53:5141.
[130] Zhilyaev AP, Nurislamova GV, Kim BK, Baró MD, Szpunar JA, Langdon TG: Acta Mater 2003; 51:753.
[131] Lutterotti L, Scardi P: J Appl Cryst 1990; 23:246.
[132] Young RA in: The Rietveld Method, (International Union of Crystallography, Oxford University Press, Oxford, 1995).
[133] Concustell A, Sort J, Woodcock TG, Gimazov A, Suriñach S, Gebert A, Eckert J, Zhilyaev AP, Baró MD: Intermetallics 2006;14:871.
[134] Tang WJ, Sandstrom R, Miyazaki S: J Phase Equil 2000; 21:227.
[135] Santamarta R, Schryvers D: Intermetallics 2004; 12:341.
[136] Wang J, Kang SB, Kim HW: Mater Sci Eng A 2004; 383:356.

[137] He G, Hagiwara M, Eckert J, Löser W: Phil Mag Lett 2004; 84:365.
[138] Alcalá G, Mato S, Woodcock TG, Hangen U, Eckert J, Gebert A, Schultz L: Z Metallkd 2004; 95:317.
[139] Durst K, Backes B, Göken M: Scripta Mater 2005; 52:1093.
[140] Manika I, Maniks J: Acta Mater 2006; 54:2049.
[141] Kaya M, Gündüz M, Çadirli O, Uzun O: J Mater Sci 2004; 39:6571.
[142] Das J, Kim KB, Baier F, Löser W, Eckert J: Appl Phys Lett 2005; 87:161907.

4. Conclusions

The fundamentals of deformation behaviour of several families of metallic glasses and composite materials have been investigated by means of compression tests and nanoindentation experiments. The main conclusions on the results presented in this work are the following:

1. The mechanisms of elastic, anelastic and plastic deformation of metallic glasses influence the response of the material during a nanoindentation test. The observed and discussed results on the deformation behaviour of a Pd-base BMG lead to the following conclusions:

- The deformation of a Pd-base BMG under an indenter during constant-load segments shows classic relaxation kinetics with relaxation times which are temperature-dependent but independent of the constant-load segment and the loading rate. The observations have been correlated to anelastic deformation of metallic glasses. Hence, an activation energy of 0.26 eV has been quantified for the deformation process during constant-load segments. The low activation energy together with the short relaxation time found indicates that the observed anelastic processes are due to local atomic shear motions which change only the local shear stress but break no atomic bonds.
- Pop-in events have been observed during loading segments of the nanoindentation tests. The intensity and appearance of the serrated flow depends on the loading rate. These observations have been related to the nature of plastic deformation in metallic glasses. Plastic flow of a metallic glass under an indenter at low loading rate is accommodated by shear localization of the free volume into shear bands, leading to a serrated loading curve. High loading rates limit the localization and coalescence of free volume into shear bands.
- A strain softening has been observed as a consequence of shear band formation. In displacement control mode tests, shear localization of the free volume is inhibited since the nanoindenter releases some force from the tip, leading to a stress drop in the material and, consequently, the shear localization stops. Shear band formation provokes a drop in the necessary mean pressure to start the shear localization for the subsequent bands.

2. The crystallization behaviour, thermal stability and mechanical properties of the $Cu_{60}Zr_xTi_{40-x}$ (x = 15, 20, 22, 25, 30) metallic glasses have been extensively studied. The main conclusions are listed below:

- All the compositions studied show high thermal stability due to the combination of high crystallization temperature and high apparent activation energy. Some of the experimental results suggest the decomposition of the amorphous matrix in Ti and Cu rich

zones. The first exothermic transformation for all the compositions corresponds to the formation of a nanocomposite structure with hexagonal $Cu_{51}Zr_{14}$ particles embedded in the amorphous matrix. However, the final microstructure depends on the composition of the alloy.

- Similar elastic modulus and yield strength has been observed for the different studied amorphous alloys of the $Cu_{60}Zr_xTi_{40-x}$ system. The difference in plastic deformation between the alloys has been related to the μ/B ratio.

- The fracture surfaces of compression tested $Cu_{60}Zr_{30}Ti_{10}$ and $Cu_{60}Zr_{20}Ti_{20}$ present the same motives of fracture morphology: a vein-like pattern, intermittent smooth regions and a river-like pattern. The distribution of these features has led to the analysis of the failure of a BMG. Therefore, sub-critical crack nucleation starts from sites covered with the river-like pattern. The crack propagation further continues forming the intermittent smooth regions. The vein-like pattern develops during the ultimate failure of the compression specimens in the regions of the softened shear bands.

3. The influence of relaxation and the precipitation of secondary phases on the mechanical response of a BMG have been analysed, and the main conclusions are summarized as follows:

- Macroscopic compression tests have revealed embrittlement of the material with increasing annealing time of a $Cu_{60}Zr_{22}Ti_{18}$ BMG. The reduction of the free-volume in the amorphous matrix during the annealing treatment causes the embrittlement of the annealed samples, since plastic flow in metallic glasses needs a critical minimum amount of free-volume.

- The precipitation of nanocrystals does not change the main deformation mechanism of these materials and therefore, shear bands form and propagate across the amorphous matrix. The nanocrystals formed during the annealing may not disrupt shear band propagation due to their small size and this leads to catastrophic failure without plastic deformation in the nanocomposite. Fracture strength and Young's modulus increase with increasing crystalline volume fraction. A perfect solute mixture model of defect free nanoparticles embedded in an amorphous matrix has been applied satisfactorily to describe the strengthening mechanism.

- The mechanical behaviour of a two-phase metallic glass, consisting of a Y-rich softer matrix and a globular harder Nb-rich phase, has been investigated by nanoindentation. The elastic behaviour has been described by a proportional addition of the elastic behaviour of the different constituent phases. The plasticity and the hardness of the two-phase alloy are enhanced with respect to the single softer amorphous alloy composing the matrix, due to deflection of the shear bands in the vicinity of the hard globular phase.

4. The microstructure evolution and the mechanisms of mechanical hardening after high pressure torsion in a Ti-based dendrite/eutectic nanostructured alloy have been investigated. The main results can be summarized as follows:

- The dendrites are formed of a β-Ti solid solution, while the matrix is composed by a nanostructured eutectic of β-Ti and NiTi phases and an intermetallic phase (i.e. $CuTi_2$). After HPT, no phase transformations take place, but grain size of all phases is reduced while microstrains are increased.
- The dendrites are found to be harder than the eutectic matrix. The structural refinement that occurs in all phases during the severe plastic deformation imposed by HPT strengthens the material. Interestingly, this hardening is more pronounced for the eutectic regions, probably due to the bending effect observed in the lamellae which causes a concomitant loss in their directionality, thus hindering the interlamellar glide.
- The estimation of the overall hardness from the hardness of the constituent phases is only possible when using local hardness values evaluated at similar indentation depths, due to the indentation size-effect.

The deformation mechanisms and the applications of metallic glasses and composite materials are still under investigation. The use of complementary techniques, such as SEM or TEM, has shown to provide valuable information for the in-depth investigation of the microscopic mechanisms governing plastic flow in metallic glasses and their composites. The work presented in this thesis is likely to motivate new studies on the subject, from both fundamental and technological points of view. Nanoindentation can still be vastly used to study the deformation behaviour of metallic glasses. The obtained results can help in the interpretation of phenomena, like the indentation size-effect, relaxation processes, cyclic deformation and deformation during indentation in metallic glasses. The work has shed some light into the recently proposed routes to increase mechanical toughness of metallic glasses, such as the development of nanocomposites or phase separation into two amorphous counterparts. Although studies using nanoindentation in composite materials are still not widely carried out, the power of this technique is clearly shown in this work enabling a distinction to be made between the hardening of the constituent phases. Hence, the underlying mechanisms governing the property changes in a composite material during plastic deformation (i.e. compression tests or severe plastic deformation) can now be better understood. Finally, more work has to be done in the optimization of ductilization procedures of metallic glasses and nanocrystalline alloys which may enhance their performance and widen their applicability as structural materials.

It is also worth noting that several papers directly or indirectly related to the presented work have been published in international journals. These papers are listed below:

- Révész Á, Concustell A, Varga LK, Suriñach S, Baró MD. Mater Sci Eng A 2004; 375:776.
- Concustell A, Révész Á, Suriñach S, Varga LK, Heunen G, Baró MD. J Mater Res 2004; 19:505.
- Concustell A, Zielinska M, Révész Á, Suriñach S, Varga LK, Baró MD. Intermetallics 2004; 12:1063.
- Sort J, Ile DC, Zhilyaev AP, Concustell A, Czeppe T, Stoica M, Suriñach S, Eckert J, Baró MD Scripta Mater 2004; 50:1221.
- Concustell A, Sort J, Alcalá G, Mato S, Gebert A, Eckert J, Baró MD. J Mater Res 2005; 20:2719.
- Concustell A, Alcalá G, Mato S, Woodcock TG, Gebert A, Eckert J, Baró MD. Intermetallics 2005; 13:1214.
- Concustell A, Sort J, Woodcock TG, Gimazov A, Suriñach S, Gebert A, Eckert J, Zhilyaev AP, Baró MD. Intermetallics 2006; 14:871.
- Kusy M, Kühn U, Concustell A, Gebert A, Eckert J, Schultz L, Baró MD. Intermetallics 2006; 14:982.
- Concustell A, Sort J, Greer AL, Baró MD. Appl Phys Lett 2006; 88:171911.
- Sort J, Concustell A, Menéndez E, Suriñach S, Rao KV, Deevi SC, Baró MD, Nogués J. Adv Mater 2006; 18:1717.
- Sort J, Concustell A, Menéndez E, Suriñach S, Baró MD, Farran J, Nogués J. Appl Phys Lett 2006; 89:032509.
- Van Steenberge N, Das J, Concustell A, Sort J, Suriñach S, Eckert J, Baró MD. Scripta Mater 2006; 55:1087.
- Concustell, N. Mattern, H. Wendrock, U. Kuehn, A. Gebert, J. Eckert, A.L. Greer, J. Sort, M.D. Baró. Scripta Mater 2007; 56:85.
- Concustell A, Sort J, Suriñach S, Gebert A, Eckert J, Zhilyaev AP, Baró MD. Intermetallics (accepted).
- Van Steenberge N, Sort J, Concustell A, Das J, Scudino S, Suriñach S, Eckert J, Baró MD. Scripta Mater 2007, doi:10.1016/j.scriptamat.2006.12.014

APPENDIX -I-

Microstructural analysis by means of x-ray diffraction

I.I.- Bragg's law of x-ray diffraction

To describe the way x-rays diffract in a perfect crystal (without distortions and with atoms located in fixed positions) we will consider that x-rays are perfectly parallel and monochromatic (with a wavelength λ) and make an incident angle θ with respect to the reticular planes of the crystal [1].

As a result of interactions with atoms, x-rays are dispersed in all directions, but the diffraction beam is formed from those x-rays for which the incident angle is equal to the reflected angle. For example, as can be seen in Fig. A1.1, the rays *1* and *1a* strike atoms *K* and *P* and are scattered in all directions, but only in the directions *1'* and *1a'* these scattered beams are completely in phase and therefore capable to reinforce one another. Therefore, the difference in their path length will fulfil the following relationship:

$$QK - PR = PK\cos\theta - PK\cos\theta = 0 \qquad \text{eq. a1.1}$$

Similarly, the rays scattered by all the atoms in the first plane in a direction parallel to *1'* are in phase and add they contribute to the diffracted beam. This will actually occur for all planes separately.

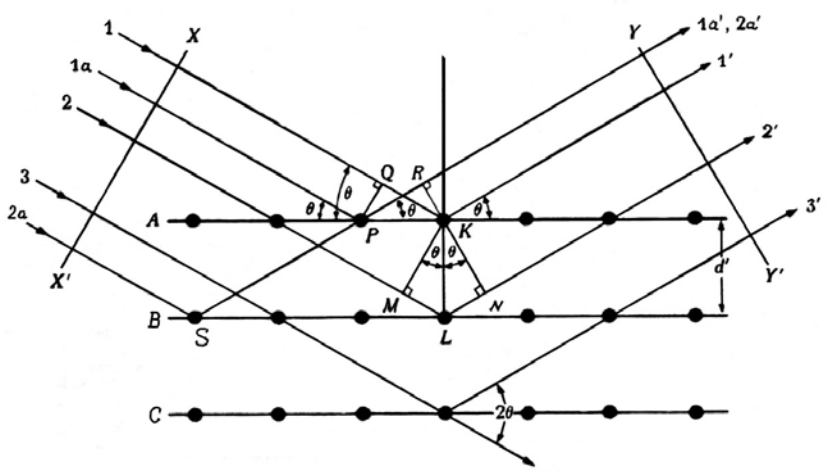

Figure A1.1. X-ray diffraction in a crystal [1].

However, rays *1* and *2* will be scattered by atoms *K* and *L*, respectively, and their path difference will be:

$$ML + LN = d \ \ sin\theta + d \ \ sin\theta \qquad \text{eq. a1.2}$$

Similar relationships can be derived from other rays striking atoms in different planes. Therefore, rays *1'* and *2'* will be completely in phase if the following relationship is fulfilled (difference of path length equal to a whole number of wavelengths, *n*):

$$n\lambda = 2d \ sin\theta \qquad \text{eq. a1.3}$$

where *n* is the reflection order, *d* is the interplanar difference and θ is the incidence angle. This relationship is known as Bragg Law, since it was elaborated in 1912 by W.L. Bragg [2].

I.II.- The effect of crystallite size and microstrains on the XRD patterns: Scherrer's formula deduction

Bragg's law of XRD assumes the crystal to be ideal, without defects. This is usually not fulfilled in reality. Moreover, x-rays are never perfectly collimated, i.e. some divergence is always inevitably present. This is of big importance, since it allows determination of the *crystallite size*, which is the minimum part of material that diffracts coherently [1].

Let us consider a crystal of finite thickness *t*, composed of a set of *m* + 1 diffraction planes (see figure A1.2). In the figure, θ is the incident variable angle, θ_B is the incident angle that fulfills exactly Bragg's law and λ and *d* are the wavelength of the incident beam and the interplanar distance, respectively.

The rays *A*, *D*, ..., *M* make an incident angle with the crystallographic planes exactly equal to θ_B. The ray *D'* is out of phase with respect to *A'* by exactly an amount equal to one wavelength. And *M'* is *m* wavelengths out of phase with respect to *A'*. Therefore, the rays *A'*, *D'*, ..., *M'* interfere constructively and form a diffracted beam of maximum intensity. Let us now suppose that two different rays, *B* and *C*, that make incident angles θ_1 and θ_2, slightly different from θ_B, so that:

$$\begin{aligned} \theta_1 &= \theta_B + \Delta\theta \\ \theta_2 &= \theta_B - \Delta\theta \end{aligned} \qquad \text{eq. a1.4}$$

and fulfil the condition:

$$\begin{aligned} 2t \ sin\theta_1 &= (m+1)\lambda \\ 2t \ sin\theta_2 &= (m-1)\lambda \end{aligned} \qquad \text{eq. a1.5}$$

Thus, for θ_1, the planes *i* and *i + 1* are slightly out of phase and between the planes 0 and *m* it is possible to find midway in the crystal a plane for which the difference of phase with respect to *B'* will be exactly $\lambda / 2$, thus interfering destructively with it. These rays cancel one another and so do the other rays from similar pairs of planes throughout the crystal, the net effect being that rays scattered by the top half of the crystal annul those scattered by the bottom half. The

intensity of the beam diffracted at an angle θ_1 is therefore zero. Similarly, the intensity of the beam diffracted at an angle θ_2 is also zero. For rays making an incident angle between θ_1 and θ_B the intensity will have an intermediate value between $I_{Màx}$ and I = 0. Thus, a distribution of intensities is obtained.

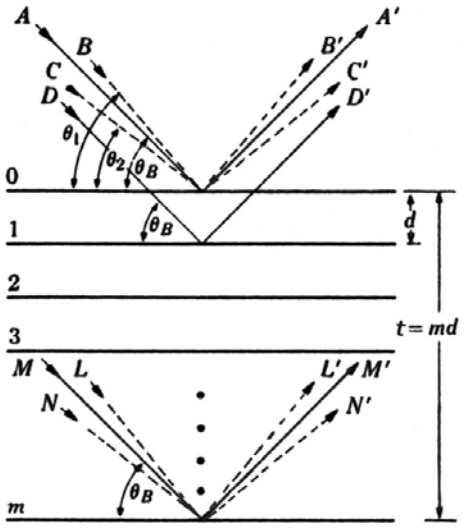

Figure A1.2. Finite crystallite size effect on diffraction [1].

Subtracting equations eq. a1.5 one obtains:

$$2\lambda = 2t\ (sin\theta_1 - sin\theta_2) = 4t\ \cos\left(\frac{\theta_1+\theta_2}{2}\right)\ sin\left(\frac{\theta_1-\theta_2}{2}\right) \approx 4t\left(\frac{\theta_1-\theta_2}{2}\right)\cos\theta_B \qquad \text{eq. a1.6}$$

where the approximation $sin(x) \approx x$ has been used, together with:

$$\frac{\theta_1+\theta_2}{2} = \theta_B \qquad \text{eq. a1.7}$$

If we define: $(\theta_1 - \theta_2) = \beta$, where β is the half-height width, from equation a.6 one can deduce:

$$\beta = \frac{\lambda}{t\ \cos\theta_B} \qquad \text{eq. a1.8}$$

which is the well-known *Scherrer formula* for crystallite size [1,3]. A more precise treatment gives that:

$$\beta = \frac{0.9\lambda}{t\ \cos\theta_B} \qquad \text{eq. a1.9}$$

This equation is valid only for crystallite sizes smaller than 100 nm. Moreover, t is not exactly the crystallite size but the *coherent diffraction domain* (portion of crystal that gives a beam of diffracted rays with well-defined phase relation). This means that dislocations or stacking faults

inside the crystallites can also limit the *coherent diffraction domain*. Moreover, for an infinite crystal:

$$\lim_{m\to\infty}\left(\sin\theta_1\right)=\lim_{m\to\infty}\left(\frac{m-1}{m}\frac{\lambda}{2d}\right)=\frac{\lambda}{2d}=\sin\theta_B \qquad \text{eq. a1.10}$$

This means that for an infinite crystal $\theta_1 = \theta_B = \theta_2$, and the intensity will be a δ-Dirac.

Furthermore, during ball milling and heat treatments not only crystallite size is found to vary but also some strains may appear in the material which, to some extent, can deform the grains or particles. In general, it is important to distinguish between macrostrains, which affect the overall crystal, and microstrains, which are created by the influence of neighbouring grains in the form of dislocations, stacking faults, etc. Both the crystallite size and microstrains can be evaluated from the width of the diffraction peaks. However, in the peak width there is also an experimental contribution. Therefore, in order to obtain reliable values of the crystallite size, all effects have to be somehow isolated and evaluated separately.

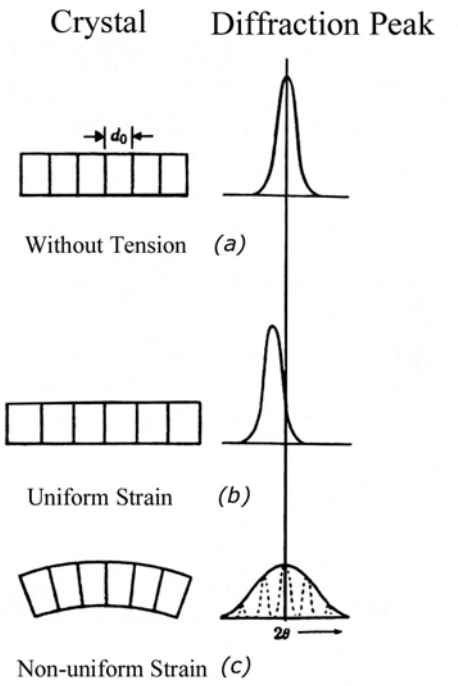

Figure A1.3. Effect of strains on the width and position of the diffraction peaks [1].

It is qualitatively easy to understand that microstrains contribute to the broadening of the diffraction peaks, while macrostrains induce a shift in their positions. Figure A1.3 shows schematic diagrams of *(a)* unstrained crystal, *(b)* uniformly strained crystal and *(c)* non-uniformly strained crystal. In *(b)* a macrostrain is shown to bring about an increase of the cell parameter, thus shifting the diffraction peak to a lower angle. In *(c)* the non-uniform strain makes different portions of the crystallites to deform differently. Thus, the cell parameter varies inside the crystallite from one region to another. As a result, we would obtain several sharp

peaks (one from every sub-crystallite), mutually overlapped which, as a result, would give a wide diffraction peak, as observed experimentally.

I.III.- Evaluation of structural parameters by single-peak fit method (*Marquardt Model)*

The analysis of XRD data can be performed by fitting peak by peak or fitting the whole spectra (Fourier analysis). The analysis peak by peak was carried out using the *MARQFITO* program, which was obtained from the Materials Engineering Department of Trento University. This program fits the peaks using a *pseudo-Voigt* function, by means of mathematic algorithms, based on the *Marquardt model* [4], using a minimum square method.

The diffraction profile obtained experimentally, *h(x)*, is the convolution product of a "pure" diffraction profile, *f(x)*, and the experimental contribution, *g(x)*:

$$h(x) = \int_{-\infty}^{\infty} g(\varepsilon) f(x-\varepsilon) d\varepsilon \qquad \text{eq. a1.11}$$

Crystallite sizes and microstrains are determined from the pure diffraction profile, *f(x)*. A good approximation of *f(x)* is obtained using a pseudo-Voigt function [5], which can be written as a lineal combination of a Cauchy (related to crystallite size) and Gaussian (related to microstrains) functions. The width of the experimental contribution to the diffraction peak, *g(x)*, also has these two components.

It has been demonstrated that the Voigt function is a good mathematical approach to describe the behaviour of the diffraction peaks [6]. In particular, it can be written as the convolution product of a Gaussian, *G(x)*, and a Lorentzian (or Cauchy), *C(x)*, functions, which when normalized to the peak integrated intensities, are given by:

$$G(x) = \frac{2}{W_{1/2}} \sqrt{\frac{\ln 2}{\pi}} \cdot \exp\left[-\frac{4 \ln 2}{W_{1/2}^2} x^2 \right] \qquad \text{eq. a1.12}$$

$$C(x) = \frac{2}{\pi} \cdot \frac{1}{W_{1/2}} \cdot \left[\frac{1}{1 + \frac{4x^2}{W_{1/2}^2}} \right] \qquad \text{eq. a1.13}$$

where *x* represents the distance with respect to the maximum of the diffraction peak (it takes the value 0 at the peak center) and $W_{1/2}$ is the full-width at half height, once the background is eliminated. Sometimes it is also designated as *HWHM (half width at half maximum)*. It is necessary to distinguish $W_{1/2}$ from the integral width, β, which is defined as the integrated intensity of the peak divided by its height:

$$\beta = \frac{1}{I_p}\int I(2\theta)d(2\theta) \qquad \text{eq. a1.14}$$

where I_p is the maximum intensity of the peak and $I(2\theta)$ is the intensity corresponding to the angle 2θ.

Therefore, the instrumental function, $g(x)$, has two contributions: gaussian ($g_G(x)$), which is mainly due to the x-rays source and geometry and is especially important for low angles ($2\theta < 90^o$), and the lorentzian ($g_C(x)$), which is mainly due to the wavelength dispersion and is especially important for high angles. Therefore, $g(x)$ can be written as the convolution product of $g_G(x)$ and $g_C(x)$, which we can indicate in a simple way as follows:

$$g(x) = g_G(x) * g_C(x) \qquad \text{eq. a1.15}$$

Similarly, the pure diffraction profile, $f(x)$, can be expressed as a convolution product of a gaussian contribution, due to microstrains, and a lorentzian contribution, due to crystallite size distribution. We can express, therefore, $f(x)$ as follows:

$$f(x) = f_G(x) * f_C(x) \qquad \text{eq. a1.16}$$

In summary, the experimental profile can be written in this way:

$$h(x) = \left[f_G(x) * g_G(x)\right] * \left[f_C(x) * g_C(x)\right] \qquad \text{eq. a1.17}$$

To avoid having to calculate lengthily the integrals of the convolution product, a good approximation is to use the pseudo-Voigt function, instead of the Voigt function. The pseudo-Voigt function can be written as a linear combination of Cauchy and Gauss functions:

$$pV(x) = \eta C(x) + (1-\eta)G(x) \qquad \text{eq. a1.18}$$

where η is the Gaussian parameter, which can take values from 0 to 1. If η is close to unity this indicates that the curve lorentzian-like. Conversely if η is close to 0, the gaussian contribution predominates. For $x = 0$, i.e. at the maximum intensity, the pseudo-Voigt function can be written in the following way:

$$pV(0) = \eta\left(\frac{2}{\pi}\right)\left(\frac{1}{W_{1/2}}\right) + (1-\eta)\left(2\sqrt{\frac{\ln 2}{\pi}}\right)\left(\frac{1}{W_{1/2}}\right) \qquad \text{eq. a1.19}$$

Moreover, both the integral width and the full width at half height are taken into account in the factor form parameter:

$$\Phi = \frac{2W_{1/2}}{\beta} \qquad \text{eq. a1.20}$$

Hence, it is possible to express the integral width as follows:

$$\beta = \frac{2W_{1/2}}{\Phi} = \frac{area_{peak}}{I_p} = \frac{1}{pV(0)} \qquad \text{eq. a1.21}$$

where the last equality is valid when the overall area of the peak is normalized to unity.

Therefore, the form factor gives an idea of the gaussian and lorentzian profile contributions, since it can be expressed in the following way:

$$\Phi = \left[\left(\frac{\sqrt{\pi}}{2\sqrt{\frac{\ln 2}{\pi}}} \right) + \left(\frac{\pi}{2} - \frac{\sqrt{\pi}}{2\sqrt{\frac{\ln 2}{\pi}}} \right) \eta \right]^{-1} \qquad \text{eq. a1.22}$$

This relationship holds both for the instrumental or the observed (experimental) profiles and, thus, it avoids having to work with the convolution products.

Experimentally, it has been demonstrated that the observed and experimental profiles fulfil the following relationships [5]:

$$\frac{\beta_C}{\beta} = a_0 + a_1\Phi + a_2\Phi^2 \qquad \text{eq. a1.23}$$

$$\frac{\beta_G}{\beta} = b_0 + b_{1/2}\left(\Phi - \frac{2}{\pi}\right)^{1/2} + b_1\Phi + b_2\Phi^2 \qquad \text{eq. a1.24}$$

where the *a* and *b* parameters take the following values:

a_0 = 2.0207	b_0 = 0.6420
a_1 = -0.4803	$b_{1/2}$ = 1.4187
a_2 = -1.7756	b_1 = -2.2043
	b_2 = 1.8706

The error in this approach is estimated to be less than 1 %. Moreover, the following relationships are also valid:

$$\beta_{hG}^2 = \beta_{fG}^2 + \beta_{gG}^2 \qquad \text{eq. a1.25}$$

$$\beta_{hC} = \beta_{fC} + \beta_{gC} \qquad \text{eq. a1.26}$$

The values θ, $W_{1/2}$ and η for the experimental spectra are determined using the fitting program. From equation eq. a1.22 it is possible to determine the form factor of the observed spectra and from equation eq. a1.21 the integral width, β_h, can also be evaluated. Then, using equations eq. a1.23 and eq. a1.24 it is possible to calculate β_{hC} and β_{hG}. The instrumental values of $W_{1/2}$ and η were determined using a Si single-crystal standard and they were found to fulfil the following expressions:

$$1-\eta = 0.84220 - 6.6440\cdot10^{-3}\,(2\theta)$$

$$W_{1/2}^2 = 1.8064\cdot10^{-4} + 1.3797\cdot10^{-3}\cdot tg(\theta) + 7.6180\cdot10^{-4}\cdot(tg(\theta))^2 \qquad \text{eq. a1.27}$$

Finally, expressions eq. a1.25 and eq. a1.26 can be used to determine the Cauchy, β_{fC}, and Gaussian, β_{fG}, contributions of the "pure" diffraction profile.

The Cauchy part of the integral width, β_{fC}, is related to the microstrains, while the gaussian contribution, β_{fG}, to the width is related crystallite size. Hence, for a specific peak, crystallite size is determined from β_{fC} using the following expression:

$$d_{hkl} = \frac{\lambda}{\beta_{fC} \cos\theta_B} \qquad \text{eq. a1.28}$$

where θ_B is the angular position of the peak (measured in radians) and λ is the wavelength (measured in Å). The value of d_{hkl} represents the diffraction coherent domain and is measured also in Å. This formula is able to estimate crystallites sizes up to 1500 Å. For larger d_{hkl}, β_{fC} tends to 0 and d_{hkl} to ∞. Equation 1.28 is called the *Scherrer formula*.

The following expression can be used to determine microstrains:

$$microstrain = \langle e \rangle = \frac{\beta_{fG}}{4tg\theta_B} \qquad \text{eq. a1.29}$$

where $\langle e \rangle$ represents the upper limit of microstrains. However, it is more frequent to use the mean square root of microstrains, $\langle \varepsilon^2 \rangle^{1/2}$ (*rms strain*), which is related to $\langle e \rangle$ in the following way: $\langle e \rangle = 1.25 \langle \varepsilon^2 \rangle^{1/2}$.

I.IV.- The full pattern fit procedure: Rietveld Method

The Rietveld method is used to obtain structural information of the sample by fitting the entire XRD pattern, thereby overcoming the problem of peak overlap and allowing the maximum amount of information to be extracted. In the Rietveld method, during the refinement process, structural parameters, background coefficients and profile parameters are varied in a least-squares procedure until the calculated powder profile, based on the structural model, best matches the observed pattern [7].

This method was first applied to powder neutron diffraction data but later it was adapted for use with x-ray data. A limitation of the Rietveld method is that one must start with a model that is a reasonable approximation of the actual structure and it is, therefore, primarily a structure refinement, as opposed to structure solution techniques. Rietveld refinements can yield very precise structural parameters, as well as quantitative analyses of phase mixtures.

The basic requirements for any Rietveld refinement are: accurate powder diffraction intensity data measured in intervals of 2θ (i.e. step-scan), a starting model that is reasonably close to the actual crystal structure of the material of interest and a model that accurately describes shapes, widths and any systematic errors in the positions of the Bragg peaks in the powder pattern.

The calculation of all structural parameters, by means of the Rietveld method, has been carried out using the *MAUD* program, created by L. Lutterotti in Trento University [8,9]. Although it is out of the scope of this thesis to give a detailed description of all the equations

used by the program, in the following paragraphs some of the more relevant aspects of the way the program fits the data will be summarized.

During a Rietveld refinement, the quantity that is minimized by the least-squares procedure is the *weighted R-pattern*, R_{wp}, which is given by [7]:

$$R_{wp} = \left[\frac{\sum_i w_i (Y_{io} - Y_{ic})^2}{\sum_i w_i Y_{io}^2} \right]^{1/2} \qquad \text{eq. a1.30}$$

where Y_{io} is the observed intensity and Y_{ic} is the calculated intensity at step i, and w_i is the statistical weight assigned to each step intensity:

$$w_i = \sigma_i^2 = \sigma_{ig}^2 + \sigma_{ib}^2 \qquad \text{eq. a1.31}$$

Here σ_{ib} is the background standard deviation and σ_{ig} is the standard deviation at each step i of the rest of the spectrum. The goodness of fit can be estimated from comparison of R_{wp} with the following parameter:

$$R_{\exp} = \left[\frac{N - P}{\sum_i w_i Y_{io}^2} \right]^{1/2} \qquad \text{eq. a1.32}$$

where N is the number of points in the spectrum and P the number of parameters to be fitted. Usually the results are normalized and expressed in terms of $GoF = R_{wp}/R_{exp}$. If GoF would take a value equal to 1 it would indicate that the fit is perfect.

The calculated XRD profile, Y_c, can be expressed in the following way:

$$Y_c(2\theta) = [B * I](2\theta) + bkg \qquad \text{eq. a1.33}$$

where $B(2\theta)$ is the function that describes the sample profile, $I(2\theta)$ is the instrumental profile and *bkg* is the background, which is fitted using a 4th degree polynomial. As in the *Marquardt model* B and I are fitted using a pseudo-Voigt function.

Actually, complicated algorithms are used to express $B(2\theta)$. For crystallite size and microstrains determination MAUD used the *Delft model* [7,10], which is based on the fact that broadening due to crystallite size refinement does not change with 2θ, while the microstrains contribution depends on 2θ.

References

[1] Cullity BD: Elemnts of X-Ray Diffraction, (Addison-Wesley Publishing Company Inc., Boston, 1978).

[2] Bragg WL: Proc Camb Phil Soc 1912; 17:43.

[3] Scherrer: Gött Nachr 1918; 2:98.

[4] Marquardt DW: J Soc Indust Appl Math 1963; 11:431.

[5] Keijser TH, Landfor JI, Mittemeijer J, Vogels ABP: J Appl Cryst 1982; 15:308.

[6] Galí S, Boletín de la Sociedad Castellonense de Cultura 1989; LXV:627.

[7] Young RA: The Rietveld Method, (Internacional Union of Crystallography, Oxford Universtiy Press, 1995).

[8] Lutterotti L, Scardi P: J Appl Cryst 1990; 23:246.

[9] Lutterotti L, Gialanella S: Acta Mater 1997; 46:101.

[10] Van Berkum JGM, Deles R, de Keijser HTh, Mittemeijer EJ: Acta Cryst 1996; A52:730.